Development of a Standardized Methodology for Identifying the Printability Zone of Cementitious 3D Printer and Object Design

by

Kamesh Solaiappan

Under the supervision of

Dr. Reza Foruzanmehr

Thesis submitted to the University of Ottawa in Partial Fulfillment of the requirements for the degree of

Master of Applied Science in Civil Engineering

uOttawa

Department of Civil Engineering
Faculty of Engineering
University of Ottawa

Abstract

The construction industry faces significant challenges in achieving sustainability and embracing digitalization. A key development area involves the integration of 3D printing into the construction process. The success of printing a well-designed 3D model critically depends on the rheological characteristics and density of the material used. However, a major limitation in current 3D printing is the absence of standardized methods for defining the printability zone of 3D printers. This master's study establishes a standard methodology to determine the printability zone of a manually fed extruder using a Delta WASP 3D printer, targeting design heights of 40 mm and 120 mm. A Controlled Shear Stress method was applied to characterize the rheological properties, such as static yield stress and viscosity at a critical shear rate of 0.02 s^{-1}. In the first phase of the study, the extrudability, shape retention, and buildability of a single layer were evaluated. It was observed that reducing the nozzle diameter from 8 mm to 6 mm increased the tip velocity, resulting in wider extrusions of approximately 25 percent. Additionally, the layer printed at an 8 mm layer height experienced excessive plastic deformation compared to those printed with a 4 mm layer height. The printability zone was determined based on printability limits, and a plot correlating yield stresses and viscosities with printability factors was created to determine the printability zone of the 8 mm nozzle with 4 mm and 8 mm layer height for the manual feeding extruder. The second phase focused on assessing the effect of different printing materials (Portland Cement and Alkali-Activated Material) on buildability at the target design heights and their corresponding impact on the printability zone. The concept of minimum specific yield strength was introduced in this study. Among the materials tested, Alkali-Activated Material (AAM) demonstrated superior buildability, successfully printing up to 35 layers – significantly higher than the 11 layers achieved with Portland Cement under comparable rheological properties. This enhanced performance is attributed to its lower density and higher specific yield strength. Finally, buildability plots for 40 mm and 120 mm were developed by correlating specific yield strength and viscosity, in accordance with the established buildability factor criteria.

Acknowledgements

The dream of pursuing a master's thesis began in 2016 during my undergraduate studies, inspired by my then-supervisor, Prof. Dharanidharan Arumugam. Determined to follow this path, I applied to several universities in Canada. Unfortunately, my first attempt resulted in rejections from seven institutions. Undeterred, I reapplied and was accepted into the course-based master's program at Carleton University. However, the goal of completing a thesis remains unfulfilled.

During my first semester, I enrolled in the Materials Characterization class and had the privilege of meeting Professor Reza Foruzanmehr. I approached him for an opportunity to pursue a thesis, and he generously agreed to supervise me. I am deeply grateful to Prof. Foruzanmehr for his invaluable support, guidance and encouragement throughout my master's journey. This work would not have been possible without his mentorship.

I also extend my sincere thanks to Professor Marc A. Dubé and Technical Officer Dr. Leo Denner at the University of Ottawa for allowing me to conduct a critical portion of my research in their laboratory. I am especially thankful to Dr. Denner for his technical expertise and assistance in resolving numerous printer-related challenges during my research. My heartfelt gratitude goes to Dr. Muslim Majeed and Dr. Gamal Elnabesly for their consistent support and technical guidance in the lab. I am grateful to my friends for their friendship, encouragement, and unwavering support throughout this journey.

Finally, I owe immense gratitude to my parents, Solaiappan and Rukmani and my sister Anita, for their unconditional love, faith and sacrifices from thousands of kilometres away, and their support has been a cornerstone of my success. This thesis is dedicated to myself and my supervisor, Prof. Reza Foruzanmehr, for believing in me and for your continuous support.

Table of Contents

List of Figures

List of Tables

List of Abbreviations

3D	-	Three Dimension
WASP	-	World's Advanced Saving Project
GHG	-	Greenhouse Gas
BIM	-	Building Information Modelling
CAD	-	Computer-Aided Design
AI	-	Artificial Intelligence
AM	-	Additive Manufacturing
ISO	-	International Organization for Standardization
ASTM	-	American Society for Testing and Materials
PC	-	Portland Cement
AAM	-	Alkali-Activated Material
RP	-	Rapid Prototyping
CAM	-	Computer-Aided Manufacturing
CNC	-	Computer Numerical Control
CC	-	Contour Crafting
STL	-	Stereolithography
G-Code	-	Geometric Code
COBOD	-	Construction of Buildings On Demand
CSR	-	Controlled Shear Rate
CSS	-	Controlled Shear Stress
OPC	-	Ordinary Portland Cement
SCM	-	Supplementary Cementitious Material
VMA	-	Viscosity Modifying Agents
LF	-	Limestone Filler
HPMC	-	Hydroxy Propyl Methyl Cellulose
GDP	-	Gross Domestic Product
SP	-	Superplasticizer

LOI	-	Loss On Ignition
MCR	-	Modular Compact Rheometer
NFRF	-	New Frontier Research Fund
VWR	-	George Van Waters

List of Symbols

S_f	-	Shape retention factor
S_{f6}	-	Shape retention factor for 6 mm nozzle
S_{f8}	-	Shape retention factor for 8 mm nozzle
M_w	-	Measured width of the printed layer
S_{lf}	-	Single-layer buildability factor
S_{lf4}	-	Single-layer buildability factor for 4 mm layer height
S_{lf8}	-	Single-layer buildability factor for 8 mm layer height
M_h	-	Measured height of the printed layer
L_w/D_w	-	Layer width/Design width
D_{w6}	-	Design width of 6 mm nozzle
D_{w8}	-	Design width of 8 mm nozzle
W/C	-	Water to Cement Ratio
l/s	-	Liquids to Solids Ratio
B_f	-	Buildability Factor
C_{lw}	-	Change in the lowermost layer
M_{ah}	-	Maximum Achievable Height
M_{ph}	-	Maximum Printable Height
D_h	-	Design Height
W_{ll}	-	Lowermost Layer Width
E_l	-	Lowermost Layer
E_u	-	Upper Layer

Chapter 1

1.0 Introduction

1.1 Background

The construction industry plays a pivotal role in shaping a more sustainable future and is essential to achieving net-zero goals by 2050 (Barbosa et al., 2017; James Manyika et al., 2015). However, the sector raise concerns about the industry's ability to meet growing demands while contending with issues like labour shortages, rising construction costs, and a lack of technological advancements and productivity (González et al., 2022; Sanjayan et al., 2019). Consequently, there is an urgent need for civil engineers, architects or developers to explore innovative solutions. One of the promising innovations involves the use of low-carbon construction materials alongside the adoption of digital technology and automation. In response, the Canadian government launched the "Platform to Decarbonize the Construction Sector at Scale" aiming for net-zero emissions by 2050. Under this initiative, two challenge programs were introduced: Low Carbon Built Environment and Construction Sector Digitalization and Productivity (National Research Council Canada, 2023; National Research Council of Canada, 2024).

Additive Manufacturing (AM) is emerging as a transformative advancement in construction. According to ISO/ASTM 52900, AM is the process of joining materials to make parts from 3D model data, usually layer upon layer, using 3D printers (International Standard Organization / American Standards for Testing and Materials, 2021). 3D printing extends this process by integrating digital technologies and advanced material properties, revolutionizing the construction process (Sanjayan et al., 2019). Traditionally, casting concrete involves using formwork to shape structural elements. In the construction industry, 3D printing is predominantly extrusion-based, where materials are deposited layer by layer to form structures. They offer various advantages such as reduction of construction costs and time, minimizing the chance of errors in material wastage and most importantly, innovative designs in the structure (Sanjayan et al., 2019).

A 3D printer extrusion system typically includes an automatic or manual feeding extruder, a hopper, and various nozzle sizes. The extruder dispenses cementitious material either under pressure or through a pressure-free auger system (Buswell et al., 2018). The shape of the nozzle (often circular) and size (ranging from 4 mm to 50 mm in diameter) are crucial to the printing process (He et al., 2021). The successful adoption of 3D printing depends on the extrusion system, the printing technology (i.e., the slicing software), and the rheological properties of the printing materials. While technological advancements have made slicing software and working with 3D printers more accessible, identifying suitable materials with the appropriate rheological properties for extrusion-based printers remains a challenge. This recalls Thomas Edison's 1917 attempt to create a machine capable of constructing residential buildings with a single

concrete pour that failed due to challenges in material properties (Sanjayan et al., 2019). This historical example underscores the critical importance of fresh state properties of cementitious material for 3D printing. The material must exhibit specific rheological properties, remaining within a certain range of yield stress and viscosity to ensure smooth material flow through the nozzle (i.e., extrudability) without compromising the initial shape (i.e., shape retention) or structural stability (i.e., buildability) of the printed object.

Extrudability refers to the ability of material to flow smoothly through the nozzle, which depends on both static yield stress and viscosity. A high solid volume fraction negatively impacts rheological properties and thus extrudability. Studies have shown that materials exceeding a certain yield stress threshold become difficult to extrude (Panda & Tan, 2018; Rehman et al., 2020). Similarly, researchers emphasize the viscosity recovery in shape retention after deposition. While high viscosity resists extrusion, overly fluid pastes may flow beyond the intended dimensions. Buildability refers to the ability of fresh pastes to sustain the designed height without any deformation or collapse in the bottom layer. The material must have sufficient structural integrity to retain its shape and support successive layers. To ensure stability, the lower layers must possess adequate strength in the fresh state to bear the weight of the upper layers. Therefore, to ensure reliable 3D printing performance, the material must possess optimized rheological properties, such that it remains within the defined printability zone.

Kazemian *et al.* explored the printability limits based on printing time, while Tay *et al.* evaluated the printability region using slump and slump flow tests (Kazemian et al., 2017; Tay et al., 2019). Other studies have qualitatively assessed printability factors by measuring the layer width, cross-sectional area, and the number of layers, comparing them to the intended design (Muthukrishnan et al., 2021; Panda & Tan, 2018; Rehman & Kim, 2021; Tay et al., 2019). However, to standardize printability assessment, it is essential to incorporate quantitative rheological parameters in accordance with the printability factors (i.e., extrudability, shape retention, and buildability). The printability zone of a printer is defined as the optimal range of rheological properties within which a printing material can be successfully extruded and deposited as a single layer within acceptable design tolerances. The zone is characterized by the interaction of printability factors such as extrudability, shape retention, and layer deposition, as well as their correlation with rheological properties, including static yield stress and viscosity. The printability zone of a 3D printer is determined solely by the characteristics of the extrusion system. When the rheological properties fall within the defined printability limits, the system is capable of successfully depositing a single layer onto the print bed. However, if the printed material lacks adequate buildability to support successive layers, the intended design height may not be achievable, and multi-layer printing may fail despite the initial layer being printable.

Unlike other printability factors, buildability is influenced not only by static yield stress but also by the density of paste, as the increased material weight can lead to plastic deformation. In simple terms, while adequate static yield stress is essential for printing multiple layers and constructing a stable three-dimensional structure, the weight of the upper layers (i.e., density of paste) also plays a critical role in the stability of the printed structure in the fresh state. Existing literature introduces numerical models that incorporate density as a key factor in determining yield strength (Roussel, 2018). For successful 3D printing of a given design, materials must exhibit both appropriate static yield stress and density. This underscores the importance of defining the printability zone by correlating rheological properties and material density with key printability factors, especially buildability. The printability zone represents the optimal range in which the printing material can be extruded, maintain structural integrity, and achieve the target design height within acceptable tolerances. In other words, the printability zone is influenced by the extrusion system, rheological properties, design height, and material density. Based on the literature review, there is no standard method for determining the printability zone of 3D printers for cementitious materials, nor is there a correlation between rheological properties and printability factors (Zhong & Zhang, 2022).

This study established printability limits for a manually fed extruder by correlating key rheological properties, such as static yield stress and viscosity, with printability factors including extrudability, shape retention and buildability for a single layer. Moreover, successful multi-layer stacking printability zones were identified by establishing a relationship between viscosity and specific yield stress that met the acceptance criteria for printability factors. Portland Cement (PC) served as a reference material to establish the printability zone of a 3D printer, while Alkali-Activated Material (AAM) was used to fine-tune the effects of specific yield strength on the printability zone. A delta WASP printer with a manually fed extruder was used to print small-scale models resembling prefabricated interlocking building blocks.

1.2 Research Objectives

The objectives of this thesis are divided into two phases, as outlined below:

1. The first phase aims to define the printability zone of the manual feeding extruder used in this research. A range of PC pastes with increasing viscosity and yield stress was prepared, and their rheological properties were systematically characterized. Each mix was evaluated for its printability factors against each criterion using the 3D printer. Finally, correlations between rheological properties and printability factors were established to determine the upper and lower thresholds, defining the printability limits.
2. Building on the findings from the first phase, the second phase examines the effect of printing material properties (i.e., Specific yield strength) and design heights (40 mm and 120 mm). This

study aims to establish the concept of minimum specific yield strength for different mix proportions, analyze its relationship with buildability, and develop buildability plots to refine the printability zone for each design height based on buildability factor criteria.

This research study aims to establish a rheology-based methodology for determining the printability limits of a manually feeding extruder and to evaluate the effects of printing material and design height on the printability requirements of an extrusion-based 3D printing system.

1.3 Research Novelty and Contributions

This study introduces a novel, standardized methodology for 3D printing cementitious materials, addressing a significant gap in both academic literature and industry standards. Unlike conventional approaches that rely on empirical observations and qualitative assessments, this methodology offers a quantitative evaluation of printability based on measurable parameters such as shape retention and buildability. Printability limits regarding static yield stress and viscosity were defined, providing a more precise and reproducible framework. This method serves as a foundational framework for developing a standardized approach, potentially contributing to the formulation of an ASTM standard for defining the printability zone in non-pressurized extrusion-based 3D printing systems. Furthermore, the concept of specific yield strength is introduced, which integrates rheological properties with material density, to enhance the assessment of multi-layered structures. This two-phase methodology establishes a robust foundation for developing consistent and reliable standards in extrusion-based 3D printing, applicable to both research and practical industry applications.

1.4 Thesis Outline

The thesis presented is in an article-based format and is divided into five chapters that are organized as follows.

1. Chapter 1, Introduction, provides a background of this study and defines the research objectives and methodology performed in the research.
2. Chapter 2, a comprehensive literature review of 3D printing, rheological, material properties and its effect on printability.
3. Chapter 3 contains the first article, a rheological test method for determining the printability zone of cementitious 3D printers. The main objective of this chapter is to define the rheological printability limits for the printer, and it is crucial for subsequent phases of the study.

4. Chapter 4 contains the second article, the effect of printing material and design height on the printability zone. The main objective of this chapter is to identify the minimum buildable specific yield strength for 40 mm and 120 mm design heights.
5. Chapter 5 summarizes and discusses the results obtained in chapters 3 and 4, highlighting the key findings and recommendations for future work.

1.5 References

Barbosa, F., Woetzel, L., Mischke, J., Ribeirinho, M. J., Sridhar, M., Parsons, M., Bertram, N., & Brown, S. (2017). *Reinventing construction through a productivity revolution*. https://www.mckinsey.com/capabilities/operations/our-insights/reinventing-construction-through-a-productivity-revolution

Buswell, R. A., Leal de Silva, W. R., Jones, S. Z., & Dirrenberger, J. (2018). 3D printing using concrete extrusion: A roadmap for research. *Cement and Concrete Research*, *112*, 37–49. https://doi.org/10.1016/j.cemconres.2018.05.006

González, V. A., Hamzeh, F., & Alarcón, L. F. (2022). *Lean Construction 4.0* (V. A. González, F. Hamzeh, & L. F. Alarcón, Eds.; First). Routledge. https://doi.org/10.1201/9781003150930

He, L., Tan, J. Z. M., Chow, W. T., Li, H., & Pan, J. (2021). Design of novel nozzles for higher interlayer strength of 3D printed cement paste. *Additive Manufacturing*, *48*, 102452–102452. https://doi.org/10.1016/j.addma.2021.102452

International Standard Organization / American Standards for Testing and Materials. (2021). *ISO/ASTM 52900:2021 – Additive Manufacturing – General Principles – Terminology.* https://www.iso.org/obp/ui/#iso:std:iso-astm:52900:ed-2:v1:en

James Manyika, Sree Ramaswamy, Somesh Khanna, Hugo Sarrazin, Gary Pinkus, Guru Sethupathy, & Andrew Yaffe. (2015). *Digital America: A tale of the haves and have-mores*. https://www.mckinsey.com/industries/technology-media-and-telecommunications/our-insights/digital-america-a-tale-of-the-haves-and-have-mores

Kazemian, A., Yuan, X., Cochran, E., & Khoshnevis, B. (2017). Cementitious materials for construction-scale 3D printing: Laboratory testing of fresh printing mixture. *Construction and Building Materials*, *145*, 639–647. https://doi.org/10.1016/j.conbuildmat.2017.04.015

Muthukrishnan, S., Ramakrishnan, S., & Sanjayan, J. (2021). Effect of alkali reactions on the rheology of one-part 3D printable geopolymer concrete. *Cement and Concrete Composites*, *116*. https://doi.org/10.1016/j.cemconcomp.2020.103899

National Research Council Canada. (2023). *Platform to Decarbonize the Construction Sector at Scale*. https://nrc.canada.ca/en/research-development/research-collaboration/platform-decarbonize-construction-sector-scale

National Research Council of Canada. (2024). *Construction Sector Digitalization and Productivity Challenge program*. https://nrc.canada.ca/en/research-development/research-collaboration/programs/construction-digitalization-productivity-challenge-program

Oke, A. E., Aigbavboa, C. O., Segun, S. S., & Thwala, W. D. (2022). Robotics for sustainable construction. In *Sustainable Construction in the Era of the Fourth Industrial Revolution* (1st ed., Vol. 1, pp. 144–155). Routledge. https://doi.org/10.1201/9781003179849-15

Panda, B., & Tan, M. J. (2018). Experimental study on mix proportion and fresh properties of fly ash based geopolymer for 3D concrete printing. *Ceramics International*, *44*(9), 10258–10265. https://doi.org/10.1016/j.ceramint.2018.03.031

Rehman, A. U., & Kim, J. H. (2021). 3D concrete printing: A systematic review of rheology, mix designs, mechanical, microstructural, and durability characteristics. *Materials*, *14*(14). https://doi.org/10.3390/ma14143800

Rehman, A. U., Lee, S.-M., & Kim, J.-H. (2020). Use of municipal solid waste incineration ash in 3D printable concrete. *Process Safety and Environmental Protection*, *142*, 219–228. https://doi.org/10.1016/j.psep.2020.06.018

Roussel, N. (2018). Rheological requirements for printable concretes. *Cement and Concrete Research*, *112*, 76–85. https://doi.org/10.1016/j.cemconres.2018.04.005

Sanjayan, J. G., Nazari, A., & Nematollahi, B. (2019). *3D concrete printing technology: Construction and building applications* (J. G. Sanjayan, A. Nazari, & B. Nematollahi, Eds.). Butterworth-Heinemann, an imptint of Elsevier.

Tay, Y. W. D., Qian, Y., & Tan, M. J. (2019). Printability region for 3D concrete printing using slump and slump flow test. *Composites. Part B, Engineering*, *174*, 106968–106968. https://doi.org/10.1016/j.compositesb.2019.106968

United Nations Environment Programme & Yale Center for Ecosystems. (2023). *Building Materials and the Climate: Constructing a New Future*. https://wedocs.unep.org/handle/20.500.11822/43293

Wangler, T., Roussel, N., Bos, F. P., Salet, T. A. M., & Flatt, R. J. (2019). Digital Concrete: A Review. *Cement and Concrete Research*, *123*. https://doi.org/10.1016/j.cemconres.2019.105780

Zhong, H., & Zhang, M. (2022). 3D printing geopolymers: A review. *Cement and Concrete Composites*, *128*. https://doi.org/10.1016/j.cemconcomp.2022.104455

Chapter 2

2.1 Theoretical and Technical Background

2.2 Additive Manufacturing

2.2.1 General

During the 1980s, Rapid Prototyping (RP) emerged as the historical term for what is now popularly known as Additive Manufacturing (AM) or 3D printing. AM has emerged from advancements across multiple technological domains, including processing power, graphics capability, networking, and computer integration. The development of 3D Computer-Aided Design (CAD) relies on computers' ability to render 3D graphic images, which in turn depends on these technological advancements. Today, CAD technologies support the design of structures ranging from large buildings to nano-scale microprocessors. The rapid evolution of CAD has been largely driven by the needs of Computer-Aided Manufacturing (CAM), which serves as the bridge between virtual models and physical products. These technological advancements have made it possible to fabricate parts using either an additive or conventional approach (Gibson, 2021; Wong et al., 2012). The conventional approach, known as subtractive manufacturing, is typically performed using Computer Numerical Controlled (CNC) machining. In this process, the material is removed by cutting tools to form the product. However, CNC machining requires a block of material at least as large as the final product, resulting in material waste. Subtractive manufacturing has notable disadvantages compared to AM in areas such as material efficiency, speed, complexity, accuracy, geometry and programming. For example, creating intricate designs, such as a ship inside a bottle is not feasible with conventional methods unless the components are machined separately and assembled. In contrast, Additive Manufacturing can produce such designs seamlessly in a single build process. Figure **2-1** highlights the limitations of CNC machining (subtractive manufacturing) (Gibson, 2021). The ASTM Technical Committee later formalized the term “Additive Manufacturing” defining it as: “A process of joining materials to make objects from 3D model data, usually layer upon layer, as opposed to subtractive manufacturing methodologies” (International Standard Organization / American Standards for Testing and Materials, 2021).

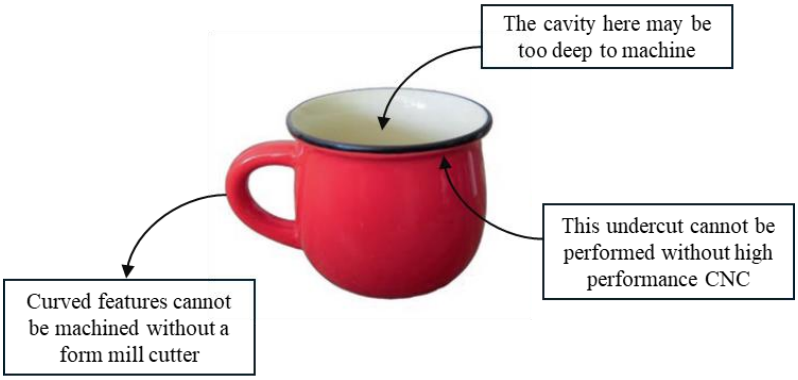

Figure 2-1: Features that represent problems using CNC machining (Gibson, 2021)

2.2.2 Additive Manufacturing in the Construction Industry

A crucial insight from Pegna's study highlights the challenges of automation in the construction industry: "The last 15 years of extensive experiments in construction robotics, however, have yielded little or no productivity improvement". This statement underscores the slow pace of technological adoption in construction, especially compared to the aerospace, automobile, retail and manufacturing industries, which began embracing automation as early as the 1970s (Sanjayan et al., 2019). Joseph Pegna was the first researcher to investigate powder-based additive manufacturing for construction, drawing inspiration from sand painting techniques in 1997. In the groundbreaking study, sand was uniformly layered, and cement layers were patterned on top. Several methods were tested to activate the cement, including spraying water, adding water droplets, curing the sample in a pressurized steam chamber at 300 ^{0}C, and applying water vapour. Notably, activating Portland Cement with water vapour achieved a maximum compressive strength of 28.3 MPa (Pegna, 1997). Since then, numerous academics, industry professionals and hobbyists have built upon Pegna's work, leading to a significant increase in related projects, especially in states and European countries, as depicted in *Figure **2-2*** (Buswell et al., 2018; Labonnote et al., 2016). The 3D printing technology offers numerous advantages. It delivers high efficiency, and significantly reduces labour requirements, thereby minimizing injury rates by automating hazardous tasks and enhancing on-site safety. Compared to traditional construction methods, 3D printing is remarkably faster by enabling continuous and automated operations. Additionally, the use of eco-friendly materials and the reduction of formwork contribute to the sustainability of 3D printing construction. The technology provides unparalleled accuracy and control over the shape and size of concrete structures, resulting in uniform and precise outcomes. Moreover, it enables the creation of complex designs and shapes that are challenging or even impossible to achieve through traditional methods (Tu et al., 2023). *Figure **2-3*** illustrates the 3D printing construction around the world (COBOD, 2023; Michelle Starr, 2016). Two state-of-the-art processes

dominate 3D printing in the construction industry: extrusion-based and powder-based technology (Sanjayan et al., 2019).

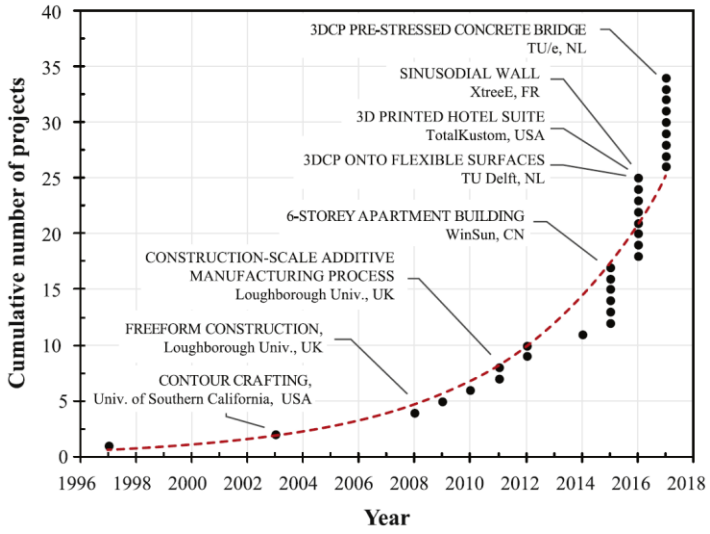

Figure 2-2: Rise in large-scale additive manufacturing in the construction industry (Buswell et al., 2018)

Figure 2-3: First 3D printed Post office in India (Left) and Dubai Future Foundation office (Right) (COBOD, 2023; Michelle Starr, 2016)

2.2.3 Extrusion-based 3D Printing Technology

The extrusion-based method is most widely used in the 3D printing construction industry due to its ease of large-scale implementation. Approximately half the processes under development worldwide rely on this technology (Tu et al., 2023). In extrusion, material is forced through a nozzle and deposited in precise locations by a print head that moves through space. This layer-by-layer building process resembles the well-known “Fused Deposition Modelling” technique used with polymers (Buswell et al., 2018; Wangler et al., 2019). The first successful extrusion-based AM technology in construction, known as Contour Crafting (CC), was invented by Dr. Behrokh Khoshnevis and patented in 2005. Initially designed for human

colonization on the Moon and Mars, CC marked a major advancement in construction technology (Khoshnevis, 2004). The CC machine developed by Khoshnevis and his team features a work envelope dimension of 5 m x 8 m x 3m, corresponding to a 120 m^2 printing zone as illustrated in Figure 2-4 (Kazemian et al., 2017). The three common types of 3D printers in construction are gantry-style, robotic arms and delta printers. Contour Crafting, as the pioneering extrusion-based technique, falls under the gantry-style category. These printers use a printhead controlled along three axes with a fixed rectangular frame. Robotic arm printers have a print head attached at the end of the robotic arm offering both translational (3) and rotational (3) degrees of freedom. Delta printers, typically smaller in scale feature a print head suspended by three retractable extension arms and extrude material with or without pressure, which enables the printing of individual elements. *Figure **2-4*** illustrates the gantry (A) and robotic arm (B) printers with three and six degrees of freedom, respectively (Wangler et al., 2019). Building components can be printed on-site or as prefabricated elements and assembled on-site (hybrid construction).

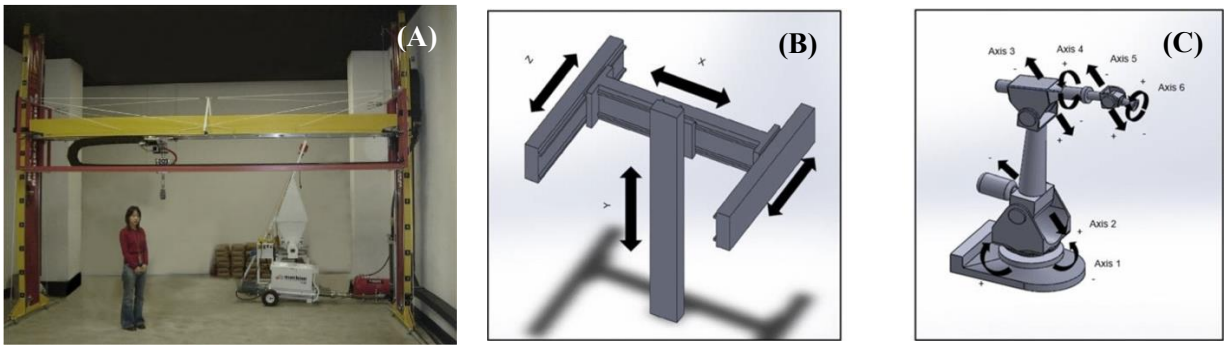

Figure 2-4: Contour Crafting machine (A), gantry-style (B) and robotic arm printer (C) (Wangler et al., 2019)

2.3 3D Printing Process

Regardless of the type of 3D printer used (gantry-style, robotic arms or delta printers), the 3D printing process in the construction industry generally follows a three-step workflow: the design stage, the material stage and the printability limits/region stage (Ambily et al., 2024; Kazemian et al., 2017; Sanjayan et al., 2019; Wangler et al., 2019; Zhang et al., 2019). The design stage involves creating a 3D model of the structure and slicing it into layers using specialized software, and the material stage involves using the optimized material for printing. Finally, the printability window stage is tailored to meet the project's specific requirements and ensures that the material is suitable for printing.

2.3.1 Design Stage

The first step in the 3D printing process is conceptualization (i.e., developing an idea for the structure's appearance and function). This stage may take many forms, from textual and narrative descriptions to sketches and representative models. The design stage plays a crucial role in defining key parameters, such as the design height and shape of the model, ensuring that structural and functional requirements are met. For 3D printing, the design must be converted to a digital format that enables the creation of a physical model. The ability to digitally represent solid objects was a prerequisite for developing the technology to physically reproduce them. The 3D printing process begins with creating a 3D CAD model, which serves as the foundational input. These models are often constructed by combining surfaces or adding thickness to a surface. However, CAD software may occasionally produce solids that are not fully enclosed, resulting in unreliable outputs. Such issues are typically identified during the conversion of the model into STL format originates from Stereolithography, which is a prerequisite for the 3D printing process (Labonnote et al., 2016).

STL provides a simplified geometric representation of CAD models by removing construction data, modelling history and other details. Technological advancements have introduced a wide range of CAD software for creating 3D models and converting them to STL format, with popular options including AutoCAD, SolidWorks and Fusion 360. The final step of the design stage is slicing the STL model. Slicing is the process of converting a 3D model into instructions for the 3D printer. During this process, slicer software takes the STL file and translates it into G-Code, a set of commands that directs the operations of the printer. The G-Code contains critical information, including:

a) Printer properties – Nozzle diameter and printer bed volume (circular or rectangular).

b) Print settings – layer heights, outline perimeters, infill shape, infill percentage and pattern, and support structure.

The most used slicer software includes Ultimaker Cura and Simplify3D. Notably, many 3D printing companies in the construction industry develop proprietary slicer software tailored to their specific needs. For instance, COBOD uses a COBOD slice, while XTreeE employs XtreeE slice (COBOD, 2024; XtreeE, 2025). *Figure 2-5* provides a pictorial representation of a rectangular panel designed in SolidWorks (A), converted into STL format (B), and sliced using Simplify 3D (C).

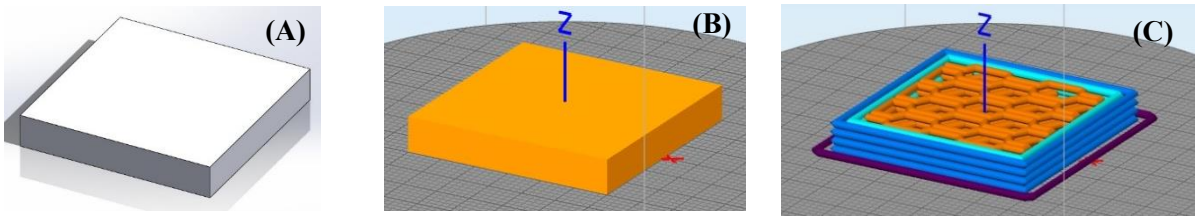

Solidworks model *STL format* *Sliced using Simplify 3D*

Figure 2-5: Pictorial representation of the design stage

2.3.2 Material Stage

Although the construction industry is poised to adopt 3D printing technology for ambitious large-scale projects, several aspects of material characteristics remain poorly understood (Khan et al., 2020; Mohan et al., 2021). In the extrusion-based method, structures are created layer by layer, with a nozzle depositing fresh cementitious material along a defined path. To ensure the quality of printed components, the material must exhibit specific characteristics: First, the fresh material must be extrudable, allowing it to pass smoothly through the nozzle (extrudability). Second, the deposited filament should retain its shape without deformation (shape retention). Finally, the material should withstand the weight of overlying layers without significant deformation (buildability) (Buswell et al., 2018; Khan et al., 2020).

Extrudability

Extrudability refers to the ability to smoothly extrude the printable mixture from the nozzle without discontinuity or breakage (Al-Noaimat et al., 2023). Depending on the type of printer used, extrusion may occur with or without additional pressure. The nozzle plays a critical role in the extrusion process, influencing both the formation of layers and their appearance during printing. For instance, circular nozzles with a tapered section facilitate extrusion compared with straight-sectional circular or rectangular (Zhang et al., 2021). Generally, extrudability is assessed by printing the whole designed model without any dimensional changes (Tu et al., 2023). Since the workability of fresh cementitious materials evolves, extrudability is also time-dependent, and this characteristic is referred to as the open time (i.e., the initial setting time duration of the printing material and can be altered by the addition of retarders or accelerators.) (Chen et al., 2021; Zhang et al., 2019).

Shape Retention

Shape retention refers to the initial rigidity of the mix in its fresh state, which determines its ability to retain its shape once deposited under its own weight before structural build-up (Paritala et al., 2023). The shape retention behaviour is quantified using the shape retention factor, which is the ratio of printed width to the

designed width(or the nozzle width) or the ratio of the printed model's cross-sectional area to the designed model's cross-sectional area (or the nozzle's cross-sectional area) (Bong et al., 2019; Khan et al., 2025). It is important to distinguish between shape retention and shape stability as described in the literature. While shape retention pertains to maintaining the initial shape after deposition, shape stability refers to the ability to withstand deformations during the buildability process.

Buildability

Buildability refers to the ability of the printed mixture to maintain its geometry under the load exerted by upper layers without collapsing or distorting (Al-Noaimat et al., 2023; Mechtcherine et al., 2020; Rahman et al., 2024). It is influenced by printing parameters and the model geometry, with various methods available for its evaluation. The most common approach involves printing a model and comparing its layer count and final height to the intended design. Yuan et *al.* assessed the green strength by applying incremental loads at specified time intervals, considering deformation acceptable if it remained below 0.2 percent of the total height (Yuan et al., 2019). Similarly, Kazemian et *al.* evaluated buildability by printing two layers and measuring the compression of the bottom layer due to the first layer's weight (Kazemian et al., 2017; Rahul et al., 2019).

2.3.3 Printability Limit/Region Stage

The concept of the printability window in terms of printing limits was introduced by Kazemain *et al.,* and their proposed framework is illustrated in *Figure 2-6*. The printability window represents the period when a printing mixture can be extruded to an acceptable quality. Kazemain *et al.* further analyzed the printability window in terms of two key limits: the printability limit and the blockage limit. The printability limit refers to the maximum duration for which a mixture can be printed with acceptable quality. The blockage limit is the maximum time the material can remain in the nozzle before hardening and blocking the extrusion (Kazemian et al., 2017).

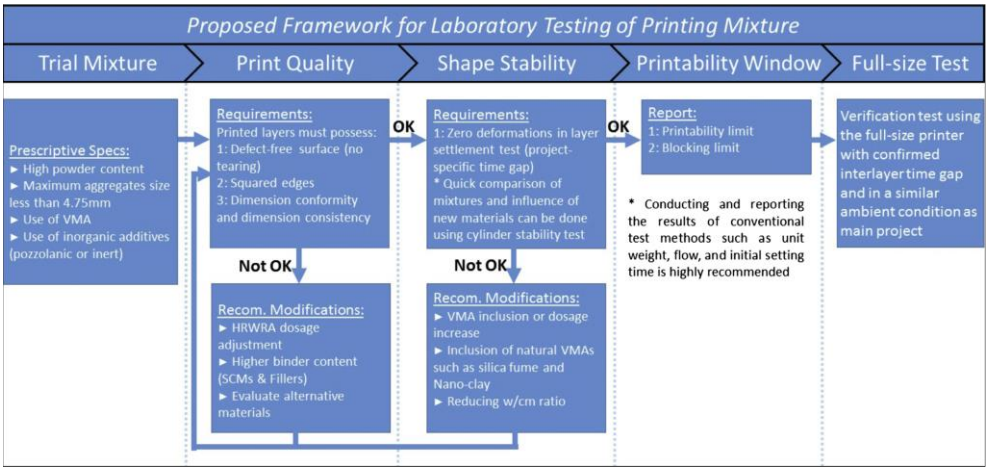

Figure 2-6: Proposed framework of printing mixture by Kazemian *et al.*

Tay *et al.* investigated the printable and non-printable regions for mortar based on slump and slump-flow measurements to evaluate the material suitability for 3D concrete printing. However, 3D printing mixes are typically characterized by low slump values and high structural buildup, which often result in poor resolution. Therefore, the slump test is not considered a reliable method for assessing printability (Jayathilakage et al., 2020). For a small gantry printer with a cavity pump, they determined the acceptable slump range to be 4 mm to 8 mm, using a 50 mm slump cone, while the slump flow should be between 150 mm to 190 mm (Tay et al., 2019). The printability region based on slump and slump flow data is shown in Figure 2-7. Similarly, Kondepudi *et al.* examined the yield stress and viscosity ranges favourable for non-segregated mixtures with shape retention. They reported that mixtures with yield stress exceeding 760 Pa and viscosity above 8 Pa.s exhibited segregation for an actuator ram-type extruder with a nozzle size of 11 mm. A cross plot illustrating yield stress and viscosity ranges for all mixes is presented in *Figure 2-8* (Kondepudi and Subramaniam, 2021). It is also important to note that the viscosity considered in this study refers to Bingham viscosity, which is lower in magnitude compared to yield stress.

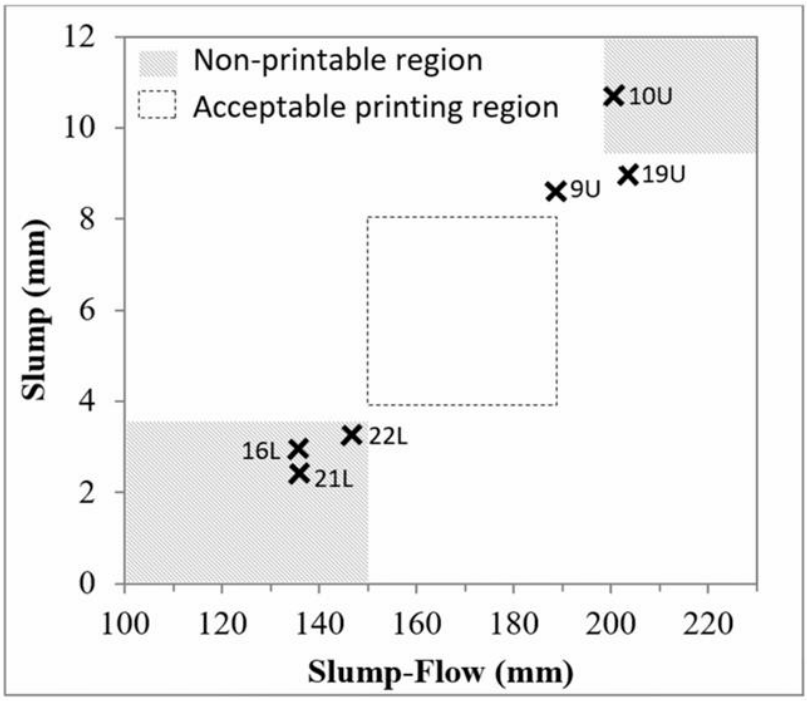

Figure 2-7: Printable and non-printable region based on slump and slump-flow by Tay et. al

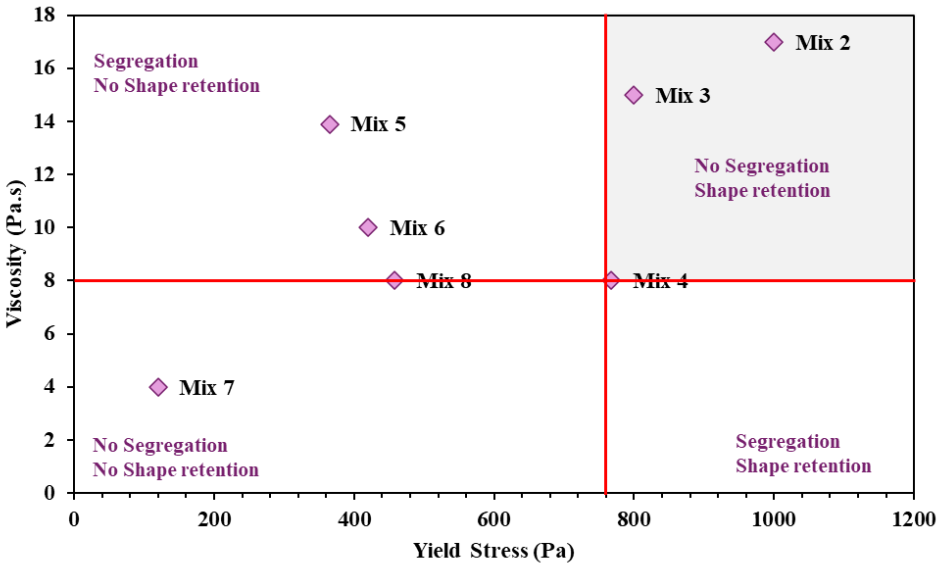

Figure 2-8: Modified cross plot of mixes performed by Kondepudi

Zhang *et al.* emphasized that "the rheological properties of cementitious printing materials are a critical factor impacting printing parameters such as extrudability, shape retention, and buildability" (Ambily et al., 2024; Zhang et al., 2019). This highlights their significance, making them one of the fundamental pillars for successful 3D printing.

2.4 Rheology

2.4.1 Basics of Rheology

Rheology is the science that studies the deformation and flow behaviour of various materials. The term "rheology" originates from the Greek word "rheos" meaning "the river", flowing", or "streaming". Thus, rheology can be understood as "flow science". The term was introduced by Prof. Bingham and Prof. Reiner in 1920 (Mezger, 2006). Rheological experiments reveal information about the flow behaviour of fluids and the deformation behaviour of solids. When a force is applied to a fluid, it flows, and upon removal of the force, the fluid does not regain its original shape. Fluids lose or dissipate energy as flow and heat. The flow properties are used to characterize fluids. Conversely, when a force is applied to a solid, it deforms, and once the force is removed, the solid returns to its original shape. Solids store energy and use it to recover or maintain their shape. Rheometry is the measuring technology used to determine rheological data. It focuses on measuring systems, instruments, and test and analysis methods. The behaviour of real materials typically combines both viscous and elastic characteristics, which is why they are referred to as viscoelastic. The various types of behaviour exhibited by materials under an applied load over time are outlined below (M. Clara Gonçalves, 2015). A visual representation of these behaviours is illustrated in *Figure 2-9*.

a) Elastic deformation – In this type of behaviour, strain is independent of time and the material returns fully to its original shape once the applied stress is removed.

b) Viscous deformation – Here, strain is time-dependent and continues to develop as long as the stress is applied. Once the stress is removed, the deformation is not recovered, indicating a permanent change in shape.

c) Viscoelastic deformation – This behaviour is characterized by partially time-dependent strain. Upon removal of the applied stress, the material exhibits partial recovery; however, the deformation is not fully reversible.

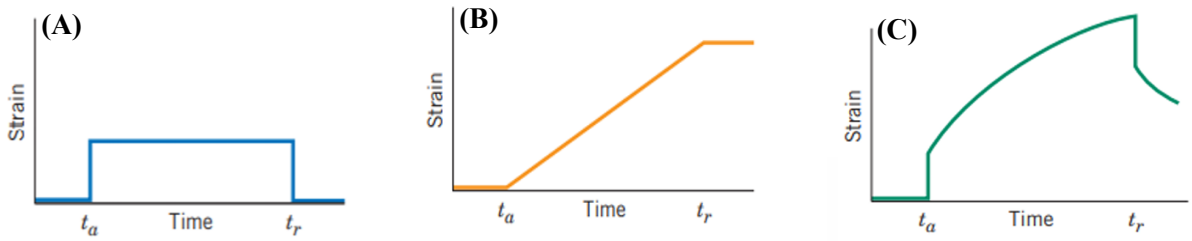

Elastic behaviour Viscous behaviour Viscoelastic behaviour

Figure 2-9: Deformation behaviour

2.4.2 Shear Stress and Shear Rate

The two-plate model is used to define the fundamental rheological parameters, as shown in *Figure 2-10*. The upper plate with the shear area A is set in motion by the shear force F, and the resulting velocity v is measured. The lower plate is stationary (v = 0). The distance h is the distance between the plates, and the liquid sample is sheared in this shear gap. It is assumed that the sample adheres to both plates and does not slide or slip among them, and there are laminar flow conditions (i.e. flow in the form of layers) (Mezger, 2006).

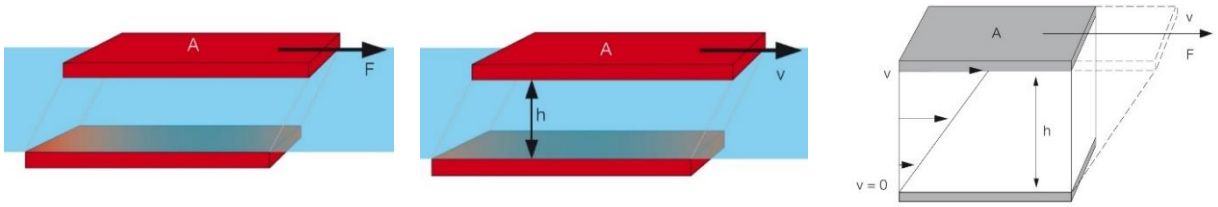

Figure 2-10: Two-plate model to define rheological parameters (Mezger, 2006)

The **shear stress** is defined as the shear force per unit area ($\tau = F/A$) with shear stress τ (pronounced as tau), shear force F (in N, Newtons) and shear area A (in m^2). The unit for shear stress is 1 N/m^2 = 1 Pa (Pascal). The rheometer records the shear force via the torque at each measuring point. The **shear rate** is defined as the change of velocity with distance ($\dot{\gamma} = v/h$) with shear rate $\dot{\gamma}$ (pronounced as gamma dot), velocity v (in m/s) and shear gap h (in m). The unit for shear rate is 1/s = 1 s^{-1}, also called reciprocal seconds. The rheometer records the velocity as the rotational speed at each measuring point.

Many liquids, gel-like, or semi-solid everyday substances are typically characterized by measuring a sample's shear stress, viscosity, flow curve, and yield point using a rotational viscometer or rheometer. The results of an experiment can be displayed as a flow curve diagram, which can be generated via predefined settings. The preset parameters can be either shear rate or shear stress. If the speed or shear rate is set or controlled, it is called a Controlled Shear Rate (CSR) test, and a typical CSR graph is shown in Figure 2-11 (Zhang et al., 2021). In contrast, if the torque or shear stress is set or controlled, it is called Controlled Shear Stress (CSS). Shear rate and Shear stress can be increased stepwise, linearly or logarithmically, with a defined measurement point duration for each point while keeping the temperature constant. Usually, flow curves are plotted with shear rate ($\dot{\gamma}$) on the x-axis and shear stress (τ) on the y-axis.

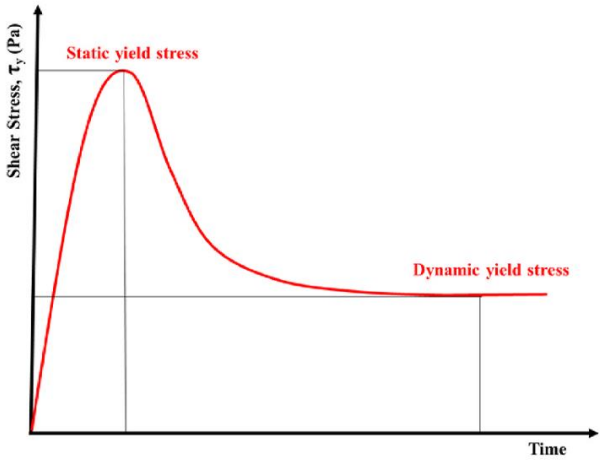

Figure 2-11: A typical Controlled Shear Rate (CSR) test (Zhang et al., 2021)

2.4.3 Viscosity

In all flowing fluids, molecules exhibit relative motion, which is inherently accompanied by internal frictional forces. This resistance, present in all moving fluids, is quantified as viscosity. In simpler terms, viscosity is a property of fluids that resists flow when an applied force is applied. Figure 2-12 illustrates a comparison between high-viscosity and low-viscosity fluids at the same temperature, highlighting that high-viscosity fluids flow more slowly than their low-viscosity counterparts (Mezger, 2006; Paar, 2025a, 2025b, 2024). Viscosity behaviour is commonly represented using viscosity curves, where shear rate ($\dot{\gamma}$) is plotted on the x-axis and viscosity (η) on the y-axis.

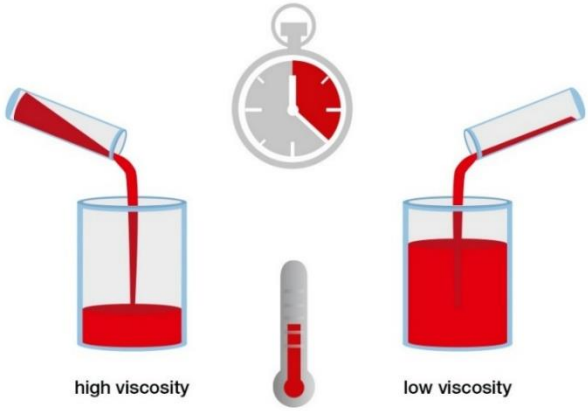

Figure 2-12: Comparison of high viscosity and low viscosity fluids at the same temperature (Mezger, 2006)

2.4.4 Newtonian and non-Newtonian fluids

Materials can be classified along a continuum from solid to liquid, with solids exhibiting elastic behaviour and liquids exhibiting viscous behaviour. However, many materials lie between these two extremes and are termed viscoelastic, as they possess both elastic and viscous properties. Based on their dominant characteristics, they are further classified as viscoelastic solids (e.g. sweet jelly) or viscoelastic liquids (e.g. a yogurt drink or shower gel). The field of viscometry encompasses both ideally viscous liquids (Newtonian fluids) and viscoelastic liquids (non-Newtonian fluids).

The flow resistance of Newtonian fluids is independent of external forces such as shear rate or shear stress. Typical Newtonian liquids include low molecular liquids – those with a molar mass below 10,000 g/mol - such as water, solvents, and salad oil. For a Newtonian fluid measured at constant temperature, the ratio of shear stress τ to the corresponding shear rate $\dot{\gamma}$ is a material constant known as **shear viscosity** ($\eta = \tau/\dot{\gamma}$) with shear viscosity η (pronounced as eta). The unit of shear viscosity is Pa.s (pascal seconds) (Mezger, 2006). Newtonian fluids exhibit a linear relationship between shear stress (τ) and shear rate ($\dot{\gamma}$), meaning their viscosity (η) remains constant regardless of changes in shear rate or shear stress (Mezger, 2006; Paar, 2025b). The flow curve and viscous curve of two ideally viscous liquids (Newtonian fluid) are illustrated in Figure 2-13.

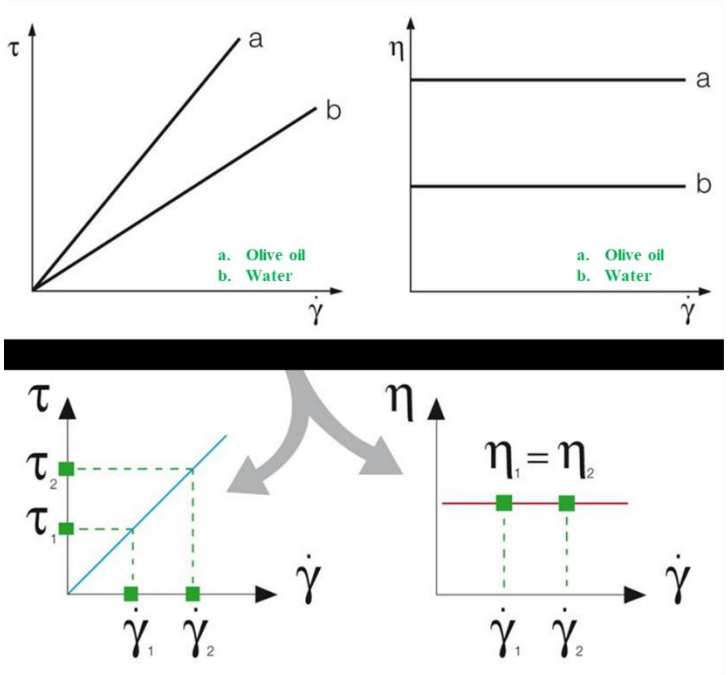

Figure 2-13: Flow curves of two different ideally viscous fluids (Mezger, 2006)

Non-Newtonian fluids exhibit flow behaviour that depends on external forces – specifically shear stress (τ) and shear rate ($\dot{\gamma}$). These fluids can demonstrate two primary types of flow behaviour: shear-thinning and shear-thickening. In shear-thinning fluids, the slope of the shear stress curve decreases with increasing shear rate, indicating that viscosity decreases as shear rate increases. This behaviour is common in everyday materials such as creams, lotions, ketchup, molten chocolate, paints and coatings. A typical flow curve and viscosity curve for shear-thinning behaviour are shown in Figure 2-14. The ratio of shear stress to shear rate varies with shear rate and is referred to as "apparent viscosity" or "apparent shear viscosity" at the corresponding shear rate. These viscosity values represent individual points on a broader viscosity function and are specific to the conditions under which they are measured.

The terms shear-thinning and pseudoplastic flow behaviour are synonyms and describe a response driven by the material's internal structure. In cementitious suspensions, shear-thinning behaviour is often explained using the breakdown of agglomerated particles in suspensions. At rest, agglomerates in a suspension can trap portions of the dispersion liquid, effectively immobilizing it. When shear is applied, these larger agglomerates gradually break down into smaller aggregates or even primary particles. As these smaller structures offer less resistance to flow, and the previously immobilized liquid (water) is released, the system exhibits shear-thinning behaviour, with viscosity decreasing as shear rate increases. In terms of particle scale, primary particles typically range from 1 nm to 10 nm, aggregates (formed by strongly bonded particles) can reach up to 100 nm, and agglomerates, composed of loosely bonded aggregates, can be as large as 100 µm (Gina Paroline, 2016; Kamykowski, 2019; Mezger, 2006; Paar, 2025c). The concept of agglomeration in cementitious suspensions and the reduction of viscosity is illustrated in Figure 2-15.

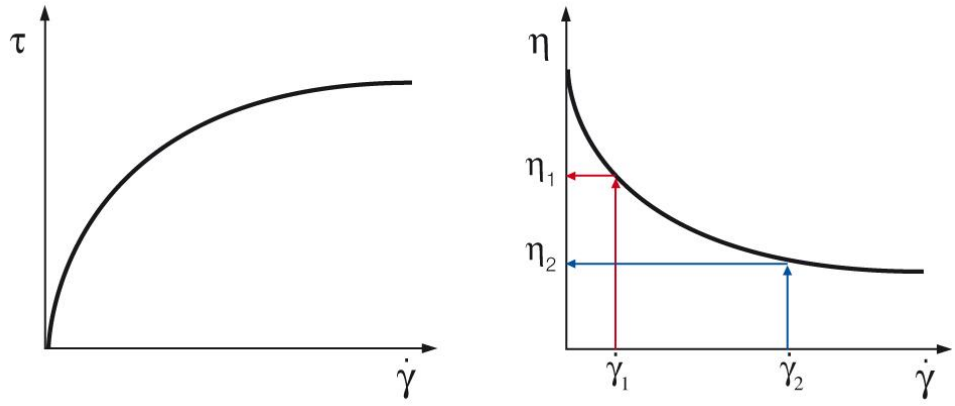

Figure 2-14: Flow curve (Left) and viscosity curve (Right)of a shear-thinning material

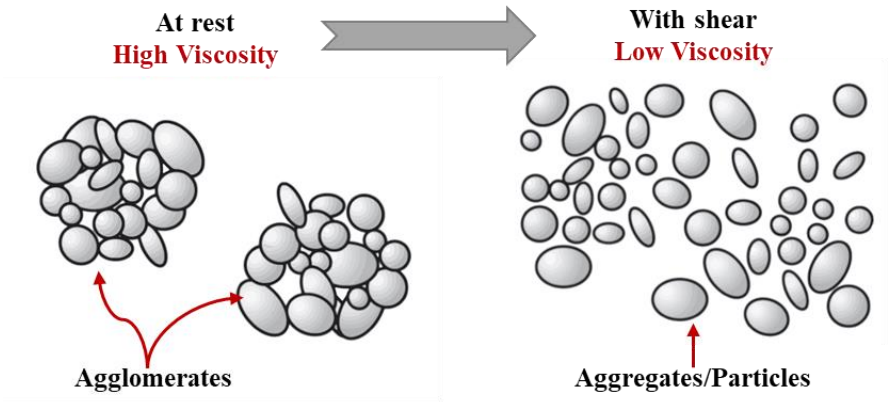

Figure 2-15: Structural changes of suspension exhibiting shear-thinning behaviour (Mezger, 2006)

For materials with shear-thickening flow behavior, the gradient of the shear stress increases at higher shear rates. This means that the sample's viscosity increases at higher shear rates. This is a relatively rare flow behavior, typically seen in samples with a high solid content, such as ceramic suspensions, starch dispersions, or dental composites. The concept of apparent viscosity is like the shear-thinning viscosity and is reported for a specific shear rate. Shear-thickening materials are much less common in industrial practice compared to shear-thinning materials (Paar, 2025d). A typical flow curve and viscosity curve for shear-thinning behaviour are shown in Figure 2-16.

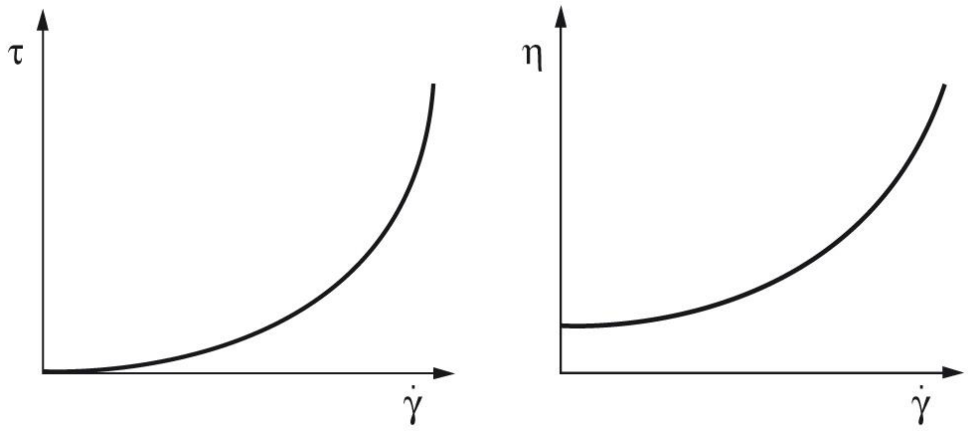

Figure 2-16: Flow curve (Left) and viscosity curve (Right)of a shear thickening material (Mezger, 2006)

The terms shear-thickening and dilatant are used interchangeably to describe the same rheological behaviour. Shear-thickening typically occurs in fluids with a high concentration of solids. In such systems, viscosity is strongly influenced by the particle concentration. At a particle volume concentration of zero ($\phi = 0$), the fluid exhibits ideal viscous flow behaviour (Newtonian fluid). As the solid fraction increases, particle collisions become more frequent, acting as obstacles to flow. These interactions introduce

additional frictional resistance, requiring greater shear forces to maintain flow. As the particle concentration approaches the maximum packing fraction (ϕ_{max}), particle-particle interactions dominate, significantly increasing the shear stress needed to deform the materials. This results in a marked increase in viscosity (Gina Paroline, 2016; Mezger, 2006; Paar, 2025e). The relationship between viscosity and solid fraction at a constant shear rate is illustrated in Figure 2-17.

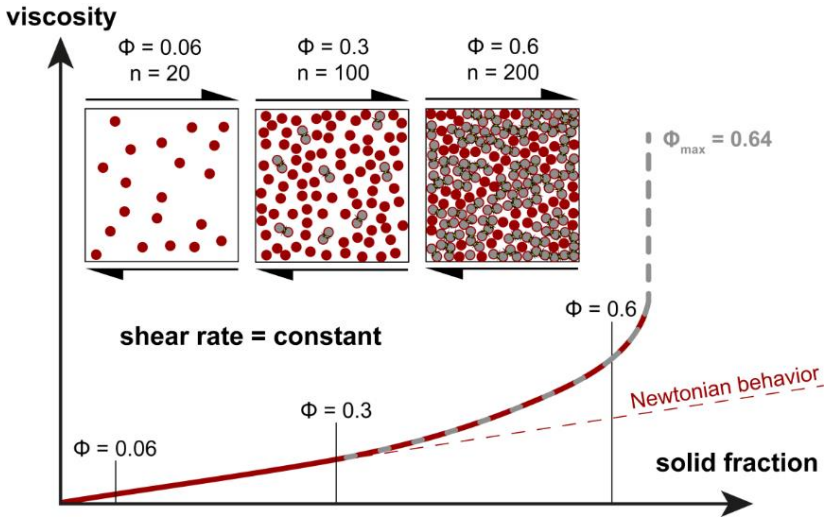

Figure 2-17: Relationship between solid fraction and viscosity (Mezger, 2006)

2.4.5 Flow Behaviour with a Yield point

Some common and complex fluids do not begin to flow until the applied stress exceeds a critical threshold known as yield stress. Yield stress is defined as the minimum stress that must be applied to the sample before it starts to flow. Below the yield stress, the material deforms elastically, like stretching a spring, while above it, the material begins to flow. In contrast, ideal viscous fluids (Newtonian fluids) exhibit a linear relationship between shear stress and shear rate and do not possess a yield point. However, many non-Newtonian fluids exhibit either shear-thinning or shear-thickening behaviour with a yield point. For instance, water is a typical sample with low viscosity (0.001 Pa.s at 20° C and has no yield point. Conversely, toothpaste is a shear-thinning fluid with a noticeable yield point and a much higher viscosity (200 Pa.s at 0.9 s^{-1} at 20° C) (AMETEK Brookfield, 2024; Paar, 2025d).

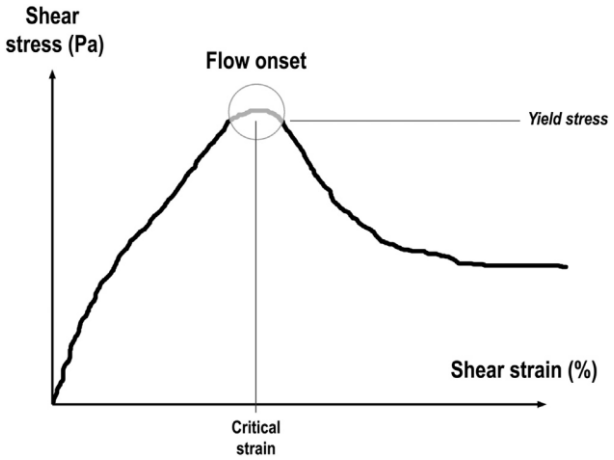

Figure 2-18: Flow behaviour with a static yield point and critical strain (Roussel, 2018)

Cementitious materials also require a minimum stress to initiate flow from a static state – this is referred to as static yield stress, and the corresponding strain rate is known as critical strain, as illustrated in *Figure 2-18* (Roussel, 2018). Below this yield stress, the material behaves elastically and does not exhibit flow (Zhang et al., 2021). It is important to emphasize that the yield point is not a fixed material constant; it depends on the specific measurement and analysis method used. Similarly, viscosity values should always be reported along with their corresponding shear rate and temperature (Malvern Instruments, 2015; Mezger, 2006; Paar, 2025f). A representative flow curve of non-Newtonian fluids showing a shear-thinning behaviour without (1) and with a yield point (2) is represented in Figure 2-19.

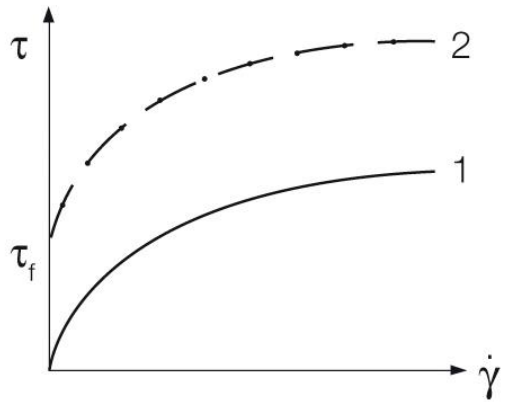

Figure 2-19: Shear thinning behaviour with and without a yield point (Mezger, 2006)

2.4.6 Time-dependent Flow Behaviour and Viscosity Function

The rheological properties of certain fluids, such as shear stress and viscosity, can vary over time under constant shear conditions and are commonly categorized based on changes in viscosity. One such time-dependent behaviour is thixotropy, where a fluid's viscosity progressively decreases under constant shear but gradually recovers once the shear is removed. This phenomenon is observed in everyday products, such as hair gels, creams, and toothpaste, which flow easily when squeezed or applied but quickly regain a solid-like structure to stay in place. A classic example is ketchup, which becomes thinner and thinner when shaken continuously, but gradually thickens and returns to its original consistency after a period of rest, typically within 10 minutes (Mezger, 2006).

Thixotropic behaviour is defined as the reduction of structural strength or viscosity during a shear load phase, followed by a more or less rapid but complete structural regeneration during the subsequent period of rest. This behaviour requires evaluating both the breakdown (decomposition) and recovery (regeneration) of the internal structure. A widely used method for evaluating thixotropic behaviour is the "Three Intervals Thixotropy Test (3ITT)", which involves applying shear in three distinct phases to simulate real-world processing conditions. The test is conducted as follows:

1. *Low-shear phase (First Interval):* A constant low shear rate is applied to establish the sample's baseline viscosity at rest. This serves as the reference point for assessing structural changes.
2. *High shear phase (Second Interval)*: A high, constant shear rate is applied to simulate conditions experienced during processing activities such as stirring, pumping, or extrusion. During this phase, structural breakdown occurs, and the extent of shear-thinning is evaluated.
3. *Low-shear phase (Third Interval)*: The shear rate is returned to the same low level used in the first interval to observe the recovery of the material's structure and viscosity. The degree of structural regeneration can be assessed by comparing the final viscosity to the initial reference value (Paar, 2025g).

A typical 3ITT graph comprises three intervals - t_0-t_1, t_1-t_2, and t_2-t_3, along with two key viscosities η_1, representing the reference viscosity during the initial low-shear phase, and η_3, indicating the recovered viscosity after a defined recovery period. Prior to conducting the test, the user must determine the specific time point at which structural recovery will be assessed. This time point should align with the practical requirements of the intended application. The viscosity values measured at this recovery point are then compared against the reference viscosity (η_1) to evaluate the extent of recovery. For example, as illustrated in Figure 2-20 the structure of the paint sample recovered approximately 80 % of its original viscosity after 60 seconds in the third interval (Paar, 2025g, 2025h, 2025i).

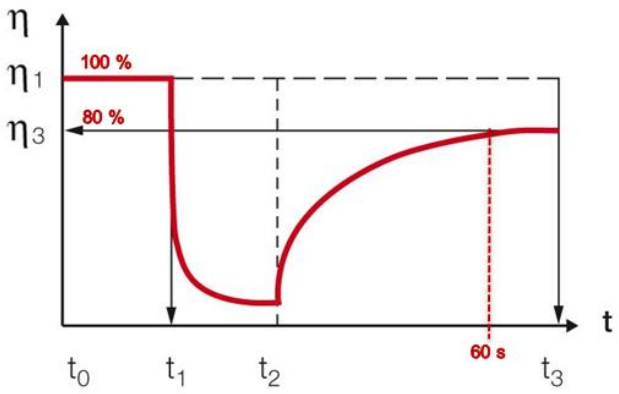

Figure 2-20: 80 percent viscosity recovery for paint after 60 seconds (Mezger, 2006)

Materials that exhibit structural decomposition during the shear phase over time demonstrate time-dependent behaviour. However, this behaviour is not classified as thixotropic unless the material's initial structural strength is fully restored after a period of rest. If structural regeneration remains incomplete even after extended resting, the material is considered to exhibit non-thixotropic behaviour or incomplete or false thixotropy, indicating a permanent structural change. For example, yogurt remains considerably thinner (compared to the initial state) even after prolonged rest (Mezger, 2006).

The other form of time-dependent rheological behaviour is known as rheopectic or rheopexy, characterized by an increase in viscosity over time under constant shear. Rheopectic behaviour involves the build-up of structural strength during a high-shear process, followed by a relatively rapid but complete decomposition of this increased structure during a subsequent rest period. Unlike non-thixotropic behaviour, rheopectic responses are fully reversible, though they are often mistakenly conflated with the former. Although rheopectic behaviour is less commonly observed than thixotropy, certain materials such as casting slips and plastisol pastes exhibit this property. A well-known example is a mixture of corn starch and water, which becomes more resistant to flow the longer shear is applied (Mezger, 2006; Paar, 2025h, 2025g, 2025i).

2.5 Relationship between Rheology and Printability Factors

Protocols for measuring the structuration behaviour of cement-based materials are often more complex and challenging to correlate with the properties required for specific processes (Roussel, 2018). From the perspective of fresh material requirements, the focus shifts from the typical fresh self-compacting concrete requirement from being fluid enough to fill a mould of a given shape under the sole effect of gravity-induced pouring to being capable of being shaped and maintaining this shape until setting. Digital fabrication of concrete eliminates the need to construct forms before shaping an element, offering greater design freedom. However, this increased simplicity comes with more stringent requirements for printable materials

(Wangler et al., 2019). The complexity lies in optimizing the fresh-state properties of cementitious materials for 3D printing (Chandra Paul et al., 2023). The major rheological properties and printability factors studied in the literature are illustrated in *Figure 2-21*. It is important to note that in this research, the manually fed extruder does not support pumpability, and thus, pumpability is not discussed.

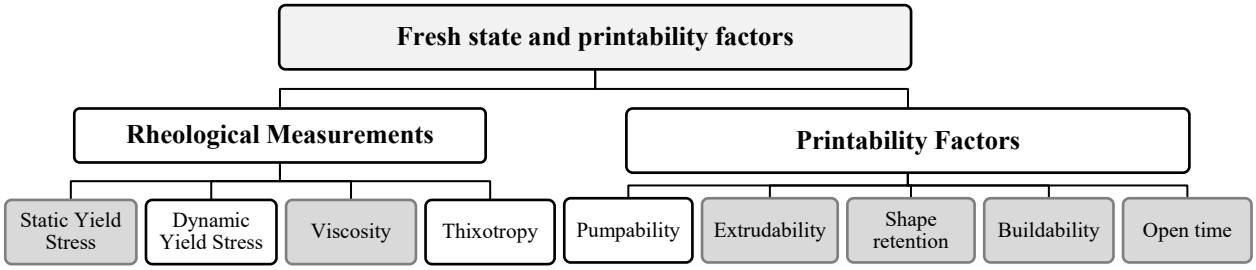

Figure 2-21: Major fresh state and printability factors

2.5.1 Correlation of Extrudability to Rheology

Extrudability is primarily influenced by the composition and size distribution of the dry constituents in the mix (Zhang et al., 2021). Additionally, the fresh state properties, such as static yield stress and viscosity, are affected by the volume fraction of solids in the mix (Coussot, 2005). This highlights that extrudability depends on both static yield stress and viscosity. When material is deposited, it initially exhibits a yield stress, and over time, these rheological parameters evolve and increase. This same principle applies to the material in the hopper; as yield stress increases with time, it can lead to breakage or reduced extrusion, ultimately affecting extrudability. The relationship between shear stress and shear rate for increasing open time is shown in *Figure 2-22*. Similarly, viscosity, which measures resistance to flow, is another key factor. If viscosity is too high, the high volume of solids fraction can negatively impact extrudability, potentially causing issues even before the printing process begins.

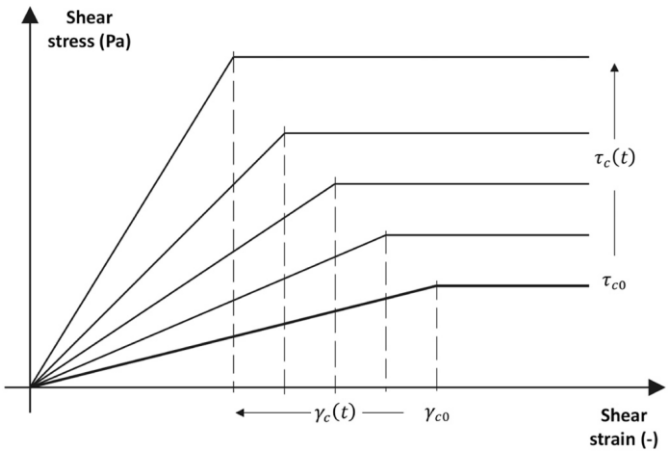

Figure 2-22: Shear stress for increasing resting time (Zhang et al., 2021)

2.5.2 Correlation of Shape Retention to Rheology

The shape retention behaviour is closely related to the fresh state viscosity of the printing material. For instance, materials with low viscosity (e.g., olive oil - 1 Pas) tend to flow easily and fail to form stable shapes, whereas high-viscosity materials (e.g., plasticine – 100 Pas) can retain their shape effectively. The shape retention behaviour is quantified using the shape retention factor, which is the ratio of printed width to the designed width(or the nozzle width) or the ratio of the printed model's cross-sectional area to the designed model's cross-sectional area (or the nozzle's cross-sectional area) (Bong et al., 2019). A typical graph illustrating the shape retention factor is shown in *Figure 2-23*. It is important to distinguish between shape retention and shape stability as described in the literature. While shape retention pertains to maintaining the initial shape after deposition, shape stability refers to the ability to withstand deformations during the buildability process. Shape stability depends on both the static yield stress and the viscosity of the material. (Khan et al., 2025).

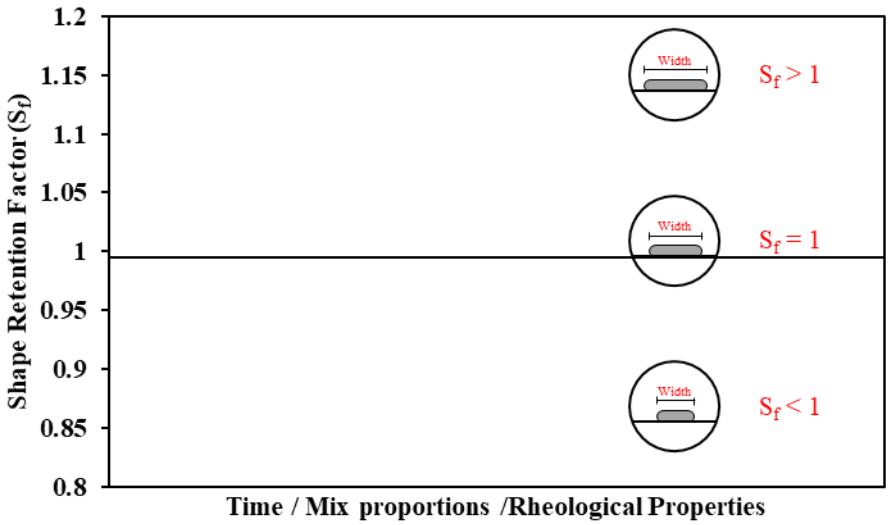

Figure 2-23: Typical shape retention factor graph

2.5.3 Buildability

Buildability is a critical property in evaluating the suitability of a material for 3D printing. Structure collapse is primarily caused by significant cumulative plastic deformation in the bottom layers (Chen et al., 2021; Muthukrishnan et al., 2022). Therefore, the printing mix must exhibit sufficient early green strength to ensure that the first layer can support the weight of subsequent layers without excessive distortion and failures (Zhang et al., 2021). Perrot *et al.* proposed a predictive framework for determining the failure time, which indicates when the printed structure is likely to collapse under its weight. In this model, the vertical stress (σ_v) exerted on the first layer is expressed as: ρgh, where ρ is the density of the material, h is the height of the vertical structure located above the first deposited layer. To estimate the maximum height during continuous deposition, the expression can be reformulated by introducing the building rate (R), defined as the vertical growth rate of the structure (i.e., printing speed) and time (t), representing the elapsed time since the deposition of the first layer: $h = Rt$, Thus, the vertical stress becomes ρgRt. Building on this concept, the authors developed an expression (Equation 1) to evaluate a critical failure time, t_f, which represents the time at which the printed structure can no longer sustain its weight and collapses. It is evaluated by incorporating $\tau_{0,0}$ (yield stress), ρ (density of the printing material), R (building rate), and α_{geom} is the geometrical factor for the structure (Perrot et al., 2016). The comparison between the critical stress (σ_c) and vertical stress (σ_v) for various building rates, along with the corresponding experimental and analytically derived failure times (t_f), is illustrated in Figure 2-24.

$$t_f = \frac{\tau_{0,0}}{\rho g R/\alpha_{geo} - A_{thix}}$$ Equation 1

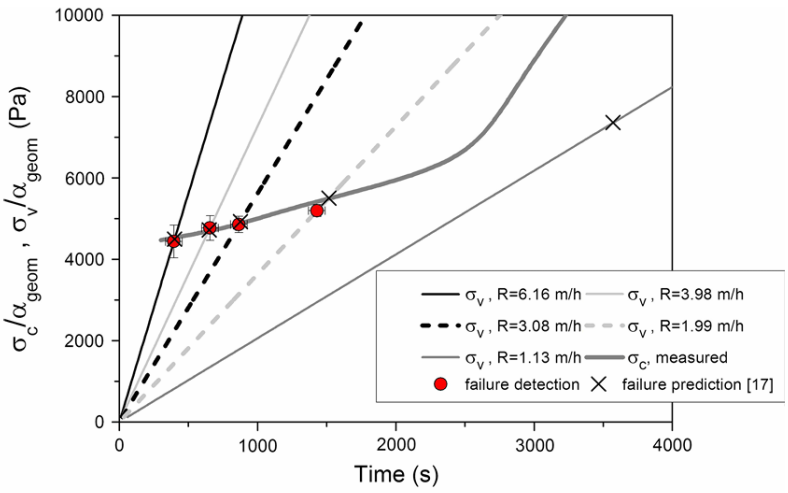

Figure 2-24: Comparison of experimental failure time and the expression value (Perrot et al., 2016)

Similarly, Roussel studied the requirements for printing material, emphasizing that they must exhibit an initial yield stress to support buildability. Additionally, the final yield stress of the printing material should be greater than ρgH/√3 to ensure structural stability (Khan et al., 2023; Roussel, 2018). In any specific case, buildability or the resistance to failure during printing is not solely governed by rheological properties. It is also influenced by material characteristics such as density, as well as printing parameters including design height and process parameters.

2.6 Effect of Material Properties

2.6.1 General

The printing material itself serves as a foundational element for the success of 3D printing. The embodied carbon of the printing materials plays a critical role in determining the overall environmental impact of the 3D printed structures (Rehman and Kim, 2021; Zhang et al., 2021). With the increasing emphasis on sustainable construction, there is a pressing need to develop eco-efficient materials that support the design and implementation of high-performance civil infrastructure with enhanced mechanical properties, durability, constructability, resilience and affordability (Biernacki et al., 2017). To meet performance requirements, the developed material must demonstrate extrudability, buildability and shape retention.

2.6.2 Density of the Printing Material

The concept of buildability refers to the ability of a printed structure to resist mechanical failure during the layer-by-layer deposition process, specifically in terms of the mechanical strength of the first deposited

layer under the increasing weight from subsequent layers. For a mix to be considered buildable, it must exhibit sufficient yield stress to support the deposition of additional layers without structural collapse.

Perrot et *al*. established a relationship between static yield stress, density and the buildability of 3D printing mixtures, described by the following equation:

$$H = \frac{\propto}{\rho g}\tau_s \qquad \text{Equation 2}$$

where H is the printed height, α is the geometric factor of the printed structure, ρ and g are the density and gravitational constant, respectively, and τ_s is the static yield stress.

It is important to note that Perrot *et al.*'s study applied a geometric factor corresponding to a solid cylinder, which may not fully represent geometries used in 3D printing. To address this limitation, Weng *et al.* modified the geometric factor for a hollow cylinder. Their study incorporated Fuller-Thompson's theory and the Marson-Percy model to determine the quantity of different sand gradations. They evaluated the model height using the modified equation and compared it with the experimentally printed height (Perrot et al., 2016; Weng et al., 2018). The resulting graph, which illustrates the relationship between maximum predicted, experimental height and static yield stress, is presented in Figure 2-25.

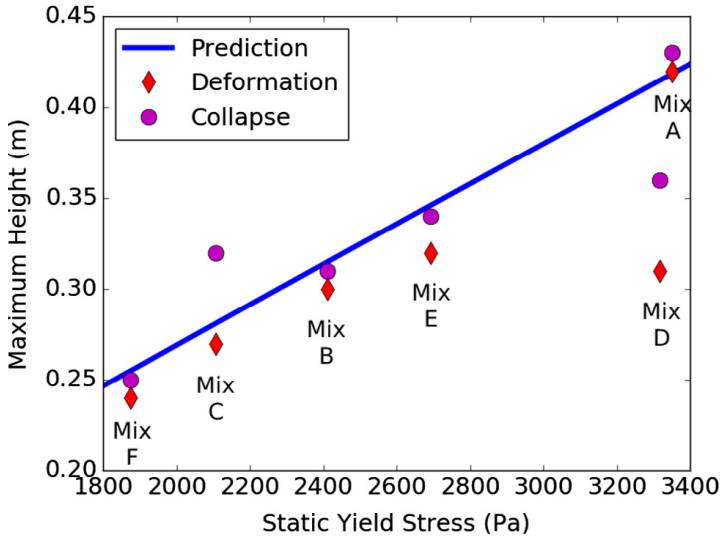

Figure 2-25: Prediction and experimental maximum build-up heights by Weng *et al.*

Furthermore, Weng *et al.* evaluated the material density at 7 days, 14 days and 28 days, noting that the density of cementitious mixtures is directly influenced by particle packing, with continuous gradation resulting in higher packing density and therefore higher bulk density. Their results, shown in Figure 2-26, indicating that the average density of hardened samples was approximately 1.85 g/cc (Weng et al., 2018). However, for 3D printing applications, it is the density of fresh mix that is of primary relevance, which is

typically higher, around 2.5 g/cc (Relis and Soroka, 1977). It is important to note that both Equation 1 and Equation 2 include density in the denominator, indicating an inverse relationship between density and buildability. This implies that, for a given static yield stress and geometric configuration, a lower material density enhances the buildability, enabling the printed model to achieve greater height before mechanical failure occurs.

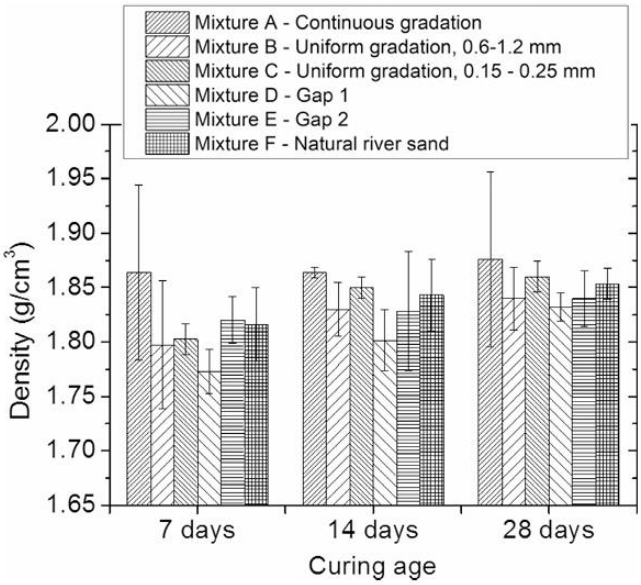

Figure 2-26: Density of various mixtures with different gradations (Relis and Soroka, 1977)

2.6.3 Effect of Printing Material

Most research focuses on printing material based on Ordinary Portland Cement. Alternatives include the partial or full replacement of OPC with Supplementary Cementitious Materials (SCMs), geopolymer or Alkali-Activated Materials (AAMs) (Khan et al., 2020). To improve printability, various additives such as nano clay, superplasticizers, fibres, and Viscosity Modifying Agents (VMA) are incorporated. Additionally, different types of aggregate with varying gradations are used to further modify the printing material properties (Zhong and Zhang, 2022). The selection and combination of raw materials, including SCMs, superplasticizer and VMAs, directly influence the rheological behaviour of the printable mix (Lu et al., 2019). It is important to highlight that raw materials influence not only the rheological properties but also the density of the printing material.

The use of various SCMs can significantly influence the rheological behaviour of cementitious mixtures, largely due to the differences in particle characteristics and mineralogical composition. Among these, Class F fly ash is one of the most widely adopted SCMs in 3D printing applications. Fly ash particles exhibit a smooth surface texture and typically range in size from 0.4 to 100 mm. Additionally, fly ash has a relatively

low density of approximately 2.1 g/cc compared to OPC, which has a density of 3.15 g/cc. The substitution of OPC with fly ash not only increases the paste volume due to its lower density but also helps reduce flocculation and segregation of particles within the fresh mix. Moreover, the spherical shape and smooth surface of fly ash enhance the flow and facilitate the extrusion process in 3D printing. In contrast, silica fume, despite its extremely fine particles and pozzolanic activity, exhibits a high-water demand, which can negatively affect the flow and printability of cementitious mixtures. As a result, silica fume is typically incorporated in small quantities as a filler rather than as a primary SCM in 3D printing applications (Manikandan et al., 2020; Rahman et al., 2024; Zhang et al., 2019).

Nano-clay and silica fume are commonly incorporated into 3D printing mixtures to enhance buildability by increasing the static yield stress of the fresh material (Douba and Kawashima, 2021; Zhang et al., 2018). In a study conducted by Arunothayan *et al*., the effect of nano-clay on the printability of fibre-reinforced mortar was examined. The addition of nano-clay at dosages of 0.1% and 0.2 % (by weight) with 2 % fibre volume was investigated. The results demonstrated that the inclusion of 0.2% nano-clay significantly improved buildability, enabling the printing of up to 50 layers, compared to only 21 layers in the reference mixture without nano-clay (Arunothayan et al., 2023). The flow behaviour of printing material with 0.1 % and 0.2 % and without nano-clay is shown in Figure 2-27.

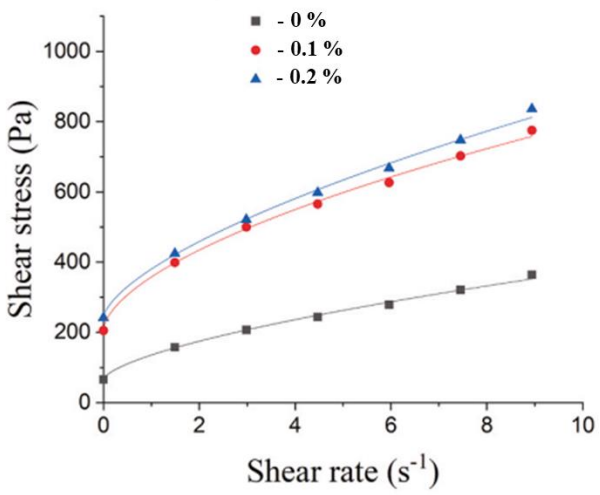

Figure 2-27: Flow curve of printing material with and without nano-clay (Arunothayan et al., 2023)

Limestone Filler (LF) is a by-product of limestone quarrying, has been used in cementitious systems for decades. LF primarily consists of Calcium Carbonate ($CaCO_3$) and is characterized by irregular, rough-textured particles that promote enhanced particle-particle adhesion and friction within the mixture. Literature reports indicate that the incorporation of LF can increase the viscosity recovery of the mix,

thereby improving the material's ability to support stacked layers during the printing process (Barbosa et al., 2022). In addition to mineral additives, the use of chemical admixtures plays a critical role in tailoring the flow behaviour of cementitious materials. The incorporation of superplasticizers, such as high-range water-reducing admixture, enhances flowability and reduces yield stress and viscosity, thereby improving extrudability. Conversely, the use of Viscosity Modifying Agents (VMAs), such as hydroxypropyl methyl cellulose (HPMC), decreases flowability while increasing the static yield stress, contributing positively to buildability and shape retention during the printability process (Rahman et al., 2024).

2.7 Effect of Printer and Process Parameters

The design of the 3D printing machine, particularly its printing methodology, plays a critical role in the success of the printing process. The process design must consider several factors related to both the fresh and hardened properties of the cementitious mix. The primary components of a typical 3D printer include the material tank or hopper, the pumping mechanism, and the extrusion nozzle. Among these, the nozzle size and shape are especially important, as they directly influence the flow characteristics of the printing material (Wei et al., 2024). In pressurized systems, the pumping pressure becomes a key parameter for sustaining a stable material flow. Additionally, the distance between the pump and the nozzle significantly affects the extrudability, with longer distances potentially reducing flow consistency. Large-scale printing applications may encounter challenges such as material segregation, filament discontinuity, and instability (Rahman et al., 2024; Sanjayan et al., 2019).

The process of printing a component involves guiding the extrusion along a predefined path to accurately position the deposited material, a path that is typically repeated for each successive layer to achieve the desired vertical build-up. The length of the extrusion path and the printing speed are critical factors that directly influence the total time required for layer deposition. Printing speeds in cementitious 3D printing typically range from 10 mm/s to 500 mm/s, depending on the system configuration, such as gantry-based and robotic arm printers (Buswell et al., 2018). Printing speed not only affects the production rate but also plays a significant role in determining the dimensional accuracy of the printed model. For a fixed nozzle diameter, an increase in printing speed generally results in a reduction of the printed layer width. This phenomenon is attributed to the reduced amount of material per unit length at higher speeds, whereas lower speeds allow a greater volume of material to be extruded, thereby producing wider layers. Zhang *et al.* investigated the relationship between printing speed and the resulting layer width for nozzle diameters of 25 mm and 30 mm, and observed that beyond a speed of 50 mm/s, the layer width decreased significantly (Zhang et al., 2022). The relationship between printing speed and layer width for (A) a rectangular box-shaped path and (B) a circular-shaped path is illustrated in Figure 2-28.

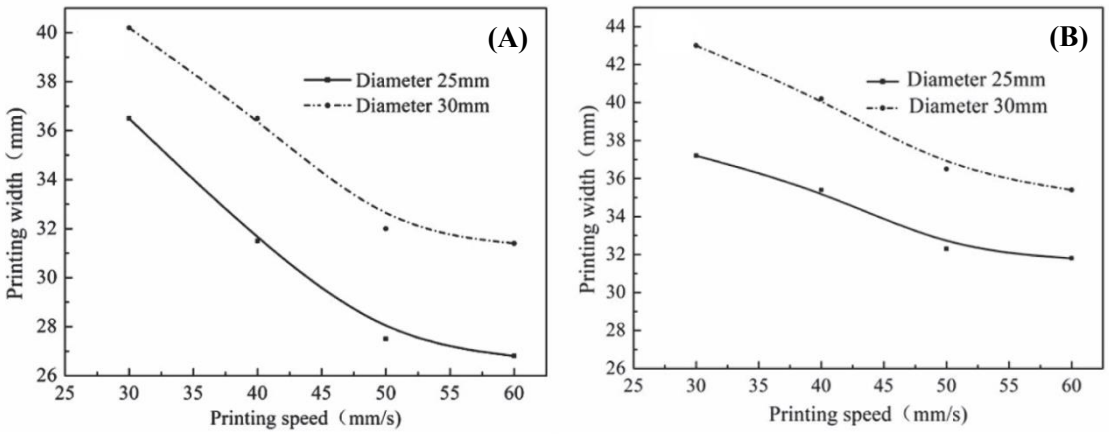

Figure 2-28: Relationship between printing width (mm) and printing speed (mm/s) for (A) rectangular box shape and (B) circular box shape (Zhang et al., 2022)

For printers equipped with circular nozzles, an increase in the nozzle standoff distance can alter the cross-sectional shape of the extruded filament, typically transitioning from a rectangular profile to a semi-circular one. Studies in literature have demonstrated that the velocity of the printing material remains relatively uniform within the printer's tank or hopper. However, as the material enters the nozzle, the velocity increases significantly due to the reduction in the nozzle's inner diameter, reaching its peak at the nozzle outlet. Wei *et al.* reported that the peak velocity exceeded 60 mm/s for a 10 mm nozzle, approximately 50 mm/s for a 20 mm nozzle, and around 30 mm/s for a 30 mm nozzle. Once the material is extruded from the nozzle, its velocity gradually decreases until it reaches 0 mm/s upon deposition, allowing the filament to stabilize in place. Based on the velocity distribution, the material flow can be categorized into three stages: (1) material inside the tank or hopper, (3) the material during extrusion, and (2) the deposited filament that has ceased deformation. To ensure optimal dimensional accuracy and surface quality, it is generally recommended to select a nozzle diameter smaller than the intended width of the printing model (Wei et al., 2024). A schematic representation of the velocity distribution across these three stages for (a) 10 mm, (b) 20 mm and (c) 30 mm nozzle diameters is shown in Figure 2-29.

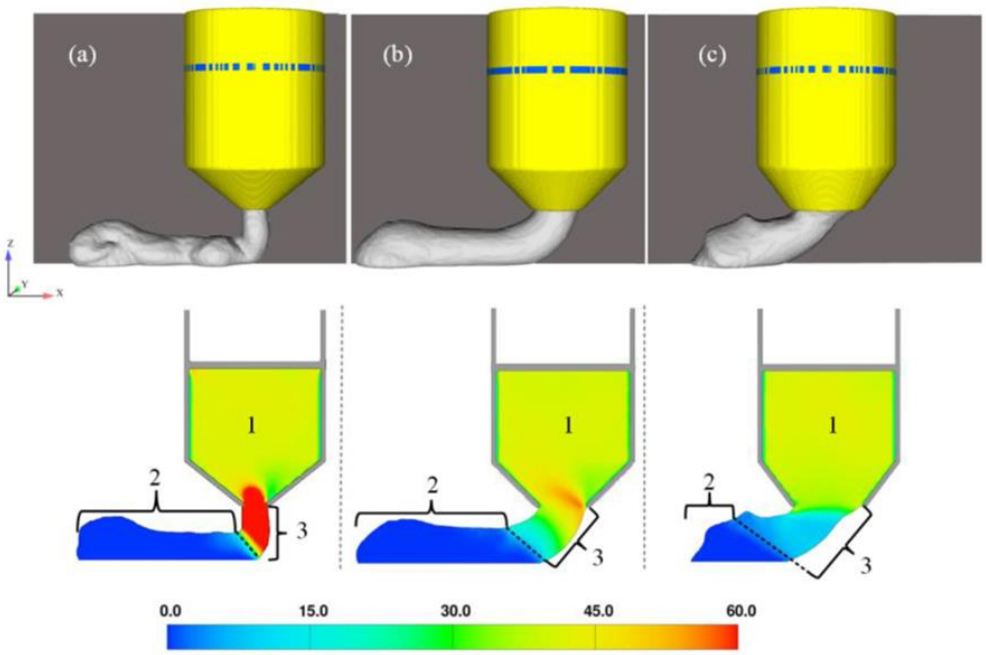

Figure 2-29: Velocity variations for (a) 10 mm, (b) 20 mm (c) 30 mm nozzle diameter (Wei et al., 2024)

2.8 Knowledge Gap

The 3D printing of cementitious materials has predominantly relied on empirical approaches. Existing research highlights the use of various rheological methods, or slump and slump flow tests, to evaluate fresh state properties and their influence on printability factors. However, there is no standardized method to identify optimized mixtures suitable for 3D printing based on the rheological properties. Developing a standard methodology would enable the determination of rheological properties that are optimal and acceptable for specific extruders and their configurations. In response to this gap, the first phase of this study conducted rheological tests to measure the static yield stress and viscosity using Portland Cement as a reference material. The printability limits were established by correlating rheological measurements and printability factors such as extrudability, shape retention, and buildability of a single layer for the delta WASP 40100 printer equipped with a manually fed extruder. Buildability is real-time applications is not limited to a single layer but rather depends on the material's ability of the material to achieve the designed height without significant deformations and within acceptable tolerances. While previous studies have established the relationship between density and height in buildability, they have not adequately addressed their relationship with the printability zone. To the best of the authors' knowledge, the role of density has been largely overlooked in existing literature on 3D printing. This presents a critical research gap, as density could significantly impact parameters such as buildability and stability during the printing process. This gap was addressed in the second phase of this study by developing a methodology tailored to specific design

heights. The specific yield strength was introduced, defined as the ratio of static yield stress to the density of the printing material and the printability plots was refined for each design height and the printability limits.

2.10 References

Al-Noaimat, Y.A., Chougan, M., Al-kheetan, M.J., Al-Mandhari, O., Al-Saidi, W., Al-Maqbali, M., Al-Hosni, H., Ghaffar, S.H., 2023. 3D printing of limestone-calcined clay cement: A review of its potential implementation in the construction industry. Results in engineering 18, 101115–101115. https://doi.org/10.1016/j.rineng.2023.101115

Ambily, P.S., Kaliyavaradhan, S.K., Rajendran, N., 2024. Top challenges to widespread 3D concrete printing (3DCP) adoption–A review. European Journal of Environmental and Civil Engineering 28, 300–328. https://doi.org/10.1080/19648189.2023.2213294

AMETEK Brookfield, 2024. Viscosity of Toothpaste.

Arunothayan, A.R., Nematollahi, B., Khayat, K.H., Ramesh, A., Sanjayan, J.G., 2023. Rheological characterization of ultra-high performance concrete for 3D printing. Cement & concrete composites 136, 104854–104854. https://doi.org/10.1016/j.cemconcomp.2022.104854

Barbosa, M.S., dos Anjos, M.A.S., Cabral, K.C., Dias, L.S., 2022. Development of composites for 3D printing with reduced cement consumption. Construction and Building Materials 341, 127775–127775. https://doi.org/10.1016/J.CONBUILDMAT.2022.127775

Biernacki, J.J., Bullard, J.W., Sant, G., Brown, K., Glasser, F.P., Jones, S., Ley, T., Livingston, R., Nicoleau, L., Olek, J., Sanchez, F., Shahsavari, R., Stutzman, P.E., Sobolev, K., Prater, T., 2017. Cements in the 21st century: Challenges, perspectives, and opportunities. Journal of the American Ceramic Society 100, 2746–2773. https://doi.org/10.1111/jace.14948

Bong, S.H., Nematollahi, B., Nazari, A., Xia, M., Sanjayan, J., 2019. Method of optimisation for ambient temperature cured sustainable geopolymers for 3D printing construction applications. Materials 12, 902–902. https://doi.org/10.3390/ma12060902

Buswell, R.A., Leal de Silva, W.R., Jones, S.Z., Dirrenberger, J., 2018. 3D printing using concrete extrusion: A roadmap for research. Cement and Concrete Research, SI : Digital concrete 2018 112, 37–49. https://doi.org/10.1016/j.cemconres.2018.05.006

Chandra Paul, S., Basit, M.A., Hasan, N.M.S., Dey, D., Panda, B., 2023. 3D printing of geopolymer mortar: Overview of the effect of mix design and printing parameters on the strength. Materials Today: Proceedings. https://doi.org/10.1016/j.matpr.2023.04.292

Chen, Y., He, S., Zhang, Y., Wan, Z., Çopuroğlu, O., Schlangen, E., 2021. 3D printing of calcined clay-limestone-based cementitious materials. Cement and Concrete Research 149, 106553–106553. https://doi.org/10.1016/J.CEMCONRES.2021.106553

COBOD, 2024. What is 3D Construction Printing [WWW Document]. URL https://cobod.com/what-is-3d-construction-printing/

COBOD, 2023. India's and the world's first 3d printed post office made by construction giant L&T construction praised by Modi, India's prime minister [WWW Document]. URL https://cobod.com/indias-and-the-worlds-first-3d-printed-post-office-made-by-construction-giant-lt-construction-praised-by-modi-indias-prime-minister/

Coussot, Philippe., 2005. Rheometry of pastes, suspensions, and granular materials : applications in industry and environment. Wiley, Hoboken, N.J.

Douba, A., Kawashima, S., 2021. Use of nanoclays and methylcellulose to tailor rheology for three-dimensional concrete printing. ACI materials journal 118, 275–289. https://doi.org/10.14359/51733129

Gibson, I. (Ian), 2021. Additive manufacturing technologies., Third edition / I... ed. Springer, Cham, Switzerland. https://doi.org/10.1007/978-3-030-56127-7

Gina Paroline, 2016. Basics of Applied Rheology Gina Paroline Manager of Technical and Professional Development Anton Paar USA.

International Standard Organization / American Standards for Testing and Materials, 2021. ISO/ASTM 52900:2021 – Additive Manufacturing – General Principles – Terminology.

Jayathilakage, R., Rajeev, P., Sanjayan, J.G., 2020. Yield stress criteria to assess the buildability of 3D concrete printing. Construction & building materials 240, 117989–117989. https://doi.org/10.1016/j.conbuildmat.2019.117989

Kamykowski, G.W., 2019. Materials Characterization by Rheological Methods.

Kazemian, A., Yuan, X., Cochran, E., Khoshnevis, B., 2017. Cementitious materials for construction-scale 3D printing: Laboratory testing of fresh printing mixture. Construction and Building Materials 145, 639–647. https://doi.org/10.1016/j.conbuildmat.2017.04.015

Khan, M.A.H., Ahmed, A., Ali, T., Qureshi, M.Z., Islam, S., Ahmed, H., Ajwad, A., Khan, M.A., 2025. Comprehensive review of 3D printed concrete, life cycle assessment, AI and ML models: Materials, engineered properties and techniques for additive manufacturing. Sustainable Materials and Technologies 43, e01164–e01164. https://doi.org/10.1016/J.SUSMAT.2024.E01164

Khan, M.S., Sanchez, F., Zhou, H., 2020. 3-D printing of concrete: Beyond horizons. Cement and Concrete Research 133. https://doi.org/10.1016/j.cemconres.2020.106070

Khan, S.A., Jassim, M., Ilcan, H., Sahin, O., Bayer, İ.R., Sahmaran, M., Koc, M., 2023. 3D printing of circular materials: Comparative environmental analysis of materials and construction techniques. Case Studies in Construction Materials 18, e02059–e02059. https://doi.org/10.1016/J.CSCM.2023.E02059

Khoshnevis, B., 2004. Automated construction by contour crafting - Related robotics and information technologies. Presented at the Automation in Construction, pp. 5–19. https://doi.org/10.1016/j.autcon.2003.08.012

Kondepudi, K., Subramaniam, K.V.L., 2021. Formulation of alkali-activated fly ash-slag binders for 3D concrete printing. Cement and Concrete Composites 119. https://doi.org/10.1016/j.cemconcomp.2021.103983
Labonnote, N., Rønnquist, A., Manum, B., Rüther, P., 2016. Additive construction: State-of-the-art, challenges and opportunities. Automation in construction 72, 347–366. https://doi.org/10.1016/j.autcon.2016.08.026
Lu, B., Weng, Y., Li, M., Qian, Y., Leong, K.F., Tan, M.J., Qian, S., 2019. A systematical review of 3D printable cementitious materials. Construction & building materials 207, 477–490. https://doi.org/10.1016/j.conbuildmat.2019.02.144
M. Clara Gonçalves, F.M., 2015. Materials for Construction and Civil Engineering.
Malvern Instruments, 2015. Understanding Yield Stress Measurements.
Manikandan, K., Wi, K., Zhang, X., Wang, K., Qin, H., 2020. Characterizing cement mixtures for concrete 3D printing. Manufacturing Letters 24, 33–37. https://doi.org/10.1016/j.mfglet.2020.03.002
Mechtcherine, V., Bos, F.P., Perrot, A., da Silva, W.R.L., Nerella, V.N., Fataei, S., Wolfs, R.J.M., Sonebi, M., Roussel, N., 2020. Extrusion-based additive manufacturing with cement-based materials – Production steps, processes, and their underlying physics: A review. Cement and Concrete Research 132. https://doi.org/10.1016/j.cemconres.2020.106037
Mezger, T.G., 2006. The rheology handbook : for users of rotational and oscillatory rheometers, 2nd rev. ed. ed. Vincentz Network, Hannover, Germany.
Michelle Starr, 2016. Dubai unveils world's first 3D-printed office building.
Mohan, M.K., Rahul, A.V., De Schutter, G., Van Tittelboom, K., 2021. Extrusion-based concrete 3D printing from a material perspective: A state-of-the-art review. Cement and Concrete Composites 115. https://doi.org/10.1016/j.cemconcomp.2020.103855
Muthukrishnan, S., Ramakrishnan, S., Sanjayan, J., 2022. In-line activation of geopolymer slurry for concrete 3D printing. Cement and Concrete Research 162. https://doi.org/10.1016/j.cemconres.2022.107008
Paar, A., 2025a. Basics of Viscometry [WWW Document]. URL https://wiki.anton-paar.com/ca-en/basic-of-viscometry/
Paar, A., 2025b. A Basic Introduction to Rheology Shear Flow [WWW Document]. URL https://wiki.anton-paar.com/ca-en/basics-of-rheology/
Paar, A., 2025c. Internal structures of samples and shear-thinning behavior [WWW Document]. URL https://wiki.anton-paar.com/ca-en/internal-structures-of-samples-and-shear-thinning-behavior/

Paar, A., 2025d. Flow curve and yield point determination with rotational viscometry [WWW Document]. URL https://wiki.anton-paar.com/ca-en/flow-curve-and-yield-point-determination-with-rotational-viscometry/
Paar, A., 2025e. The influence of particles on suspension rheology [WWW Document]. URL https://wiki.anton-paar.com/ca-en/the-influence-of-particles-on-suspension-rheology/
Paar, A., 2025f. Yield point, evaluation using the flow curve [WWW Document]. URL https://wiki.anton-paar.com/ca-en/yield-point-evaluation-using-the-flow-curve/
Paar, A., 2025g. Basics of Thixotropy [WWW Document]. URL https://wiki.anton-paar.com/ca-en/basics-of-thixotropy/
Paar, A., 2025h. Time-dependent behavior (oscillation) [WWW Document]. URL https://wiki.anton-paar.com/ca-en/time-dependent-behavior-oscillation/
Paar, A., 2025i. Evaluation of the time-dependent flow behavior [WWW Document]. URL https://wiki.anton-paar.com/ca-en/evaluation-of-the-time-dependent-flow-behavior/
Paar, A., 2024. Basics of Rheology [WWW Document]. URL https://wiki.anton-paar.com/ca-en/basics-of-rheology/
Paritala, S., Singaram, K.K., Bathina, I., Khan, M.A., Jyosyula, S.K.R., 2023. Rheology and pumpability of mix suitable for extrusion-based concrete 3D printing – A review. Construction and Building Materials 402. https://doi.org/10.1016/j.conbuildmat.2023.132962
Pegna, J., 1997. Exploratory investigation of solid freeform construction. Automation in construction 5, 427–437. https://doi.org/10.1016/S0926-5805(96)00166-5
Perrot, A., Rangeard, D., Pierre, A., 2016. Structural built-up of cement-based materials used for 3D-printing extrusion techniques. Materials and structures 49, 1213–1220. https://doi.org/10.1617/s11527-015-0571-0
Rahman, M., Rawat, S., Yang, R. (Chunhui), Mahil, A., Zhang, Y.X., 2024. A comprehensive review on fresh and rheological properties of 3D printable cementitious composites. Journal of Building Engineering 91, 109719–109719. https://doi.org/10.1016/j.jobe.2024.109719
Rahul, A.V., Santhanam, M., Meena, H., Ghani, Z., 2019. 3D printable concrete: Mixture design and test methods. Cement & concrete composites 97, 13–23. https://doi.org/10.1016/j.cemconcomp.2018.12.014
Rehman, A.U., Kim, J.H., 2021. 3D concrete printing: A systematic review of rheology, mix designs, mechanical, microstructural, and durability characteristics. Materials 14. https://doi.org/10.3390/ma14143800
Relis, M., Soroka, I., 1977. Variation in density of portland cement hydration products. Cement and Concrete Research 7, 673–680. https://doi.org/10.1016/0008-8846(77)90050-3

Roussel, N., 2018. Rheological requirements for printable concretes. Cement and Concrete Research 112, 76–85. https://doi.org/10.1016/j.cemconres.2018.04.005
Sanjayan, J.G., Nazari, A., Nematollahi, B., 2019. 3D concrete printing technology : construction and building applications. Butterworth-Heinemann, an imptint of Elsevier, Oxford.
Tay, Y.W.D., Qian, Y., Tan, M.J., 2019. Printability region for 3D concrete printing using slump and slump flow test. Composites. Part B, Engineering 174, 106968–106968. https://doi.org/10.1016/j.compositesb.2019.106968
Tu, H., Wei, Z., Bahrami, A., Ben Kahla, N., Ahmad, A., Özkılıç, Y.O., 2023. Recent advancements and future trends in 3D concrete printing using waste materials. Developments in the Built Environment 16. https://doi.org/10.1016/j.dibe.2023.100187
Wangler, T., Roussel, N., Bos, F.P., Salet, T.A.M., Flatt, R.J., 2019. Digital Concrete: A Review. Cement and Concrete Research 123. https://doi.org/10.1016/j.cemconres.2019.105780
Wei, Y., Han, S., Chen, Z., Lu, J., Li, Z., Yu, S., Cheng, W., An, M., Yan, P., 2024. Numerical simulation of 3D concrete printing derived from printer head and printing process. Journal of Building Engineering 88. https://doi.org/10.1016/j.jobe.2024.109241
Weng, Y., Li, M., Tan, M.J., Qian, S., 2018. Design 3D printing cementitious materials via Fuller Thompson theory and Marson-Percy model. Construction & building materials 163, 600–610. https://doi.org/10.1016/j.conbuildmat.2017.12.112
Wong, K.V., Hernandez, A., Anifantis, N., Findik, F., 2012. A Review of Additive Manufacturing. ISRN Mechanical Engineering 2012, 1–10. https://doi.org/10.5402/2012/208760
XtreeE, 2025. An end-to-end software suite [WWW Document]. URL https://www.xtreee.com/softwares
Yuan, Q., Li, Z., Zhou, D., Huang, T., Huang, H., Jiao, D., Shi, C., 2019. A feasible method for measuring the buildability of fresh 3D printing mortar. Construction and Building Materials 227, 116600–116600. https://doi.org/10.1016/J.CONBUILDMAT.2019.07.326
Zhang, C., Nerella, V.N., Krishna, A., Wang, S., Zhang, Y., Mechtcherine, V., Banthia, N., 2021. Mix design concepts for 3D printable concrete: A review. Cement and Concrete Composites 122. https://doi.org/10.1016/j.cemconcomp.2021.104155
Zhang, H., Wang, J., Liu, Y., Zhang, X., Zhao, Z., 2022. Effect of processing parameters on the printing quality of 3D printed composite cement-based materials. Materials letters 308, 131271–131271. https://doi.org/10.1016/j.matlet.2021.131271
Zhang, J., Wang, J., Dong, S., Yu, X., Han, B., 2019. A review of the current progress and application of 3D printed concrete. Composites Part A: Applied Science and Manufacturing 125. https://doi.org/10.1016/j.compositesa.2019.105533

Zhang, Yu, Zhang, Yunsheng, Liu, G., Yang, Y., Wu, M., Pang, B., 2018. Fresh properties of a novel 3D printing concrete ink. Construction & building materials 174, 263–271. https://doi.org/10.1016/j.conbuildmat.2018.04.115

Zhong, H., Zhang, M., 2022. 3D printing geopolymers: A review. Cement and Concrete Composites 128. https://doi.org/10.1016/j.cemconcomp.2022.104455

Chapter 3

3.1 A rheological method for determining the printability zone of cementitious 3D printers[1]

Abstract

This study establishes a standardized methodology for defining the printability zone of a manually fed extruder using a delta 3D printer. Portland cement-based reference materials were prepared by varying the water-cement ratios from 0.32 to 0.36 and superplasticizer content ranging from 0.1 to 0.5 percent. A successful 3D model was designed based on the printer and extruder specifications and transferred to the 3D printer using Geometric Code (G-Code). The controlled Shear Stress (CSS) method was employed to determine the rheological properties of all mixtures, such as static yield stress and viscosity at a critical shear rate of 0.02 s-1. Concurrently, the printability factors - extrudability, shape retention, and minimum buildability were studied and evaluated. The results revealed that nozzle diameter significantly affects shape retention behaviour. Reducing the nozzle diameter to 6 mm increased the velocity at the nozzle tip, resulting in wider extrusions and is unsuitable for 3D printing. Conversely, the 8 mm nozzle with an 8 mm layer height encountered challenges extruding materials and underwent excessive plastic deformation; however, the 4 mm layer height allowed for printing a wide range of rheological properties. The printability zone was determined based on four limits: minimum and maximum printable yield stresses and minimum and maximum printable viscosities. Ultimately, a plot correlating yield stresses and viscosities with printability factors was created to determine the printability zone of the 8 mm nozzle with 4 mm and 8 mm layer height for the manual feeding extruder.

Keywords:

Rheology, Portland Cement, 3D printer, Nozzle diameter, Layer height, Printability zone

[1] Authors: Kamesh Solaiappan and Reza Foruzanmehr

A version of this chapter is under review in the Journal of Building Engineering

Graphical Abstract

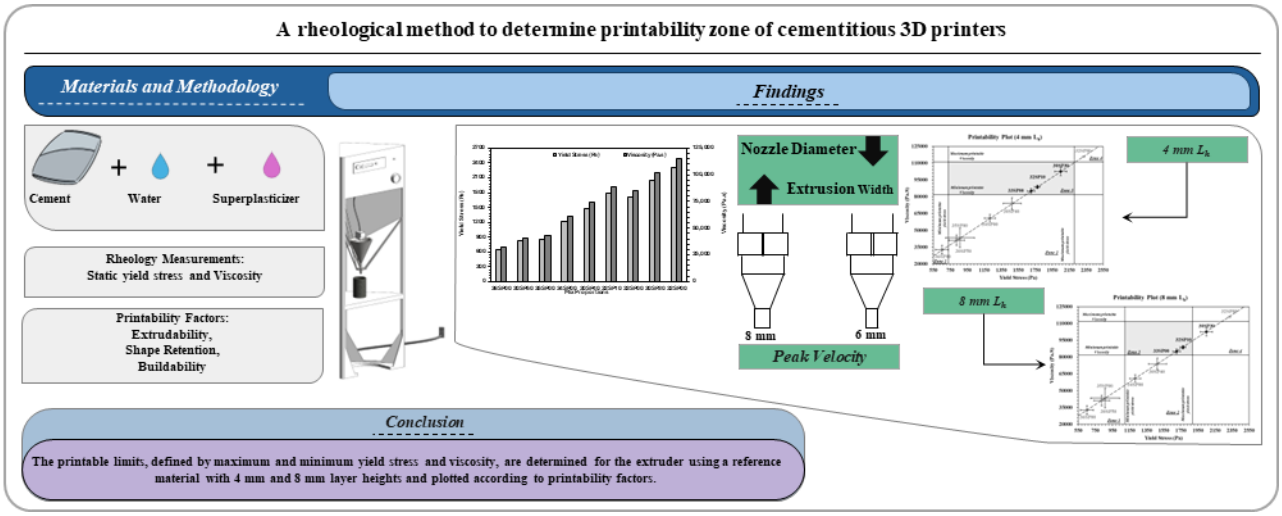

3.2 Introduction

In September 2023, the construction industry became the fourth-largest contributor to Canada's GDP, accounting for 7.4% (Statistics Canada, 2024). Despite this significant contribution, it still faces challenges in meeting the growing demand for affordable housing due to its labour-intensive, time-consuming, and expensive processes. Construction materials play a pivotal role in the industry, both in terms of cost and environmental impact. Among the construction materials, cementitious ones are vital building blocks widely used in the building industry. These materials offer exceptional water resistance and the ability to be cast into different shapes and sizes due to their versatility (Mehta, 2014). Formwork has been the conventional method for casting building elements made from cementitious materials. However, this approach has limitations, particularly in accommodating curved surfaces and intricate designs, often requiring extensive customization and labour. Additionally, Inefficient formwork design can lead to substantial materials waste, creating a dual economic and environmental burden (Llatas, 2011).

In recent years, modular prefabrication has emerged as a promising construction approach within the industry, especially regarding sustainable construction practices. Studies have shown that it can significantly reduce both material waste and the requirement for on-site formwork (Jiang et al., 2019). However, prefabrication primarily represents a shift from on-site construction to factory manufacturing (Feldmann, 2022). Despite this transition, customizing building elements remains challenging, and the process continues to be impractical from a manufacturing perspective. One solution to tailoring the shape and size of construction elements in a prefabrication set-up is to integrate additive manufacturing into their processes. As defined by ASTM F2792-12, additive manufacturing (AM) is "a process of joining materials to make objects from 3D model data, usually layer upon layer, as opposed to subtractive manufacturing

methodologies". The AM of the building elements offers several advantages, such as eliminating the need for formwork, reducing construction time, and the ability to create aesthetically pleasing and structurally complex buildings using 3D printers (Sanjayan et al., 2019).

Two prominent categories account for the industrially available 3D printing processes: extrusion-based and powder-bed fusion (Sanjayan et al., 2019). The extrusion-based method is widely adopted due to its relative simplicity. It involves the continuous feeding of cementitious materials with a nozzle, typically ranging from 4mm to 50mm in diameter, using wither a pressurized or pressure-free auger system for precise material deposition. Extrusion rates within this process can vary significantly, typically between 10 mm/s and 500 mm/s (Buswell et al., 2018). Large-scale applications use gantry-style or robotic arm printers for on-site fabrications, while smaller delta printers with extension arms handle individual components (Ambily et al., 2024; Khan et al., 2020). The printing process of cementitious materials can be classified into three phases: design phase, printability zone phase, and printing material phase (Sanjayan et al., 2019; J. Zhang et al., 2019). The initial phase involves designing a model using CAD software, saving it in the STL format, and slicing it to and slicing it into layers. The resulting output file (G-Code) specifies the extruder height, tool head position, and pathway. Ultimately, the printing success of a well-designed and sliced 3D model ultimately hinges on the rheological characteristics of the material used.

One of the significant challenges lies in material preparation, as the material must flow through the nozzle with or without supplemental pressure, and the layers should retain and be able to stack up high as designed in the software (Wangler et al., 2019; Wu et al., 2021). The second phase involves examining the printability zone, according to Kazemian et al. the printability zone was discussed in terms of two critical limits: the printability limit and the blockage limit. The printability limit signifies the duration for effective printing, while the blockage limit indicates the time before the mix hardens within the nozzle (Kazemian et al., 2017; Sanjayan et al., 2019). It demonstrates the methodology of characterizing the materials mixture using the printability factors. Tay et al. investigated the printability zone of the mix proportion based on the slump and slump flow test values and not the rheological properties (Tay et al., 2019). Kondepudi et al. plotted a graph showcasing the favourable range for non-segregated mixtures with rheological properties such as yield stress and viscosity. They assessed the printability factors such as buildability, shape retention, and segregation for each mix and plotted them in the same graph (Kondepudi & Subramaniam, 2021).

Studies have outlined qualitative methodologies for assessing printability factors, primarily through methods such as observing the width, cross-sectional area, and number of layers and comparing them with the intended design (Muthukrishnan et al., 2021; Panda & Tan, 2018; Rehman & Kim, 2021; Tay et al., 2019). However, the quantitative measurements of printability rheological properties must be considered. The mixtures with a static yield stress above a certain threshold cannot be extruded through the nozzle

(Panda & Tan, 2018; Rehman et al., 2020). Muthukrishnan et al. and Chandra Paul et al. have underscored the importance of viscosity recovery in achieving shape retention post-deposition (Chandra Paul et al., 2023; Muthukrishnan et al., 2021). For example, a paste with high viscosity may resist extrusion, whereas an overly fluid paste can be extruded smoothly but fails to retain its shape due to excessive flow (Ambily et al., 2024). To build up, the layers must possess sufficient strength to be stacked until they attain the desired height without experiencing deformation or collapse. The desired height depends on many parameters such as material and layer height. The feasibility of building up layers is linked to their static yield stress (Kondepudi & Subramaniam, 2021; Wangler et al., 2019; Wu et al., 2021). This necessitates that the cementitious materials exhibit adequate static yield stress (i.e., the minimum shear stress that makes a non-Newtonian fluid flow) and viscosity to define the printability zone for a 3D printer. Based on the literature review, it is worth mentioning that there are no standard methods to reveal the printability zone of 3D printers for cementitious materials, correlating rheological properties and printability factors (Zhong & Zhang, 2022).

The most commonly used materials in the 3D printing industry include cement-based mixes, combinations of cement and SCMs, and geopolymer-based materials (Rehman & Kim, 2021). Since each material exhibits distinct rheological properties, this study focuses on a standard methodology to determine the printability zone of a 3D printer capable of printing a single layer in its fresh state using a reference material. This was assessed by examining by correlating the rheological properties (specifically, static yield stress and viscosity) and key printability factors such as extrudability, shape retention, and buildability. Portland cement was chosen as the printing material due to its cost-effectiveness and widespread availability, serving as a benchmark material. The research utilized a delta printer to produce high-precision models resembling prefabricated interlocking building blocks.

3.3 Materials

The reference material used in this research consists of Type 1 Portland cement procured from Ciment Québec with a specific gravity of 3.2 and a specific surface area (Blaine) of 393 m^2/kg, which complies with the specifications outlined in ASTM standard C150. A typical chemical and mineralogical composition is presented in Table 3-1. The consistency of mix proportions is adjusted using MasterGlenium 7500 superplasticizer (SP), obtained from Master Builders Solutions. The SP is formulated based on polycarboxylates and conforms to ASTM C494/C 494 M for both Type A water-reducing admixtures and Type F high-range water-reducing admixtures.

Table 3-1: Chemical and mineral composition of cement

Chemical Composition (wt %)	
SiO_2	19.10
Al_2O_3	4.80
Fe_2O_3	3.60
CaO	60.20
MgO	2.60
SO_3	3.80
Na_2O	0.92
LOI	1.90
Mineralogical Composition (wt %)	
C_3S	47.0
C_2S	18.0
C_3A	7.0
C_4AF	11.0

3.4 Mix proportions

A series of continuum mixes with varying rheological properties was prepared to establish correlations between rheological parameters and printability factors. Accordingly, mix proportions were selected empirically to evaluate these factors both with and without the inclusion of SP. Each mix is designated based on a two-part code: the first two digits represent the water-cement ratio, followed by the letters 'SP' and concluding with the last two digits denoting the weight percentage of SP. For instance, a mix proportion with a 0.3 water-to-cement ratio (w/c) and 0.1 percent SP is labelled as "30SP10". The detailed mix trials are tabulated in ***Table 3-2*** and a high-performance mixer is used to mix the materials. The mixing procedure adopted to assess rheological and printability factors adheres to the ASTM standard C305-20.

Table 3-2: Mix proportions of cement paste

Mix Proportions	Solids		Liquids		
	Portland Cement	w/c	Water	Wt. Percentage of SP	Weight of Superplasticizer
	(g)	(ratio)	(g)	(%)	(g)
32SP00	1000	0.32	320	0.00%	0.0
33SP00	1000	0.33	330	0.00%	0.0

34SP00	1000	0.34	340	0.00%	0.0
35SP00	1000	0.35	350	0.00%	0.0
36SP00	1000	0.36	360	0.00%	0.0
30SP30	1000	0.3	300	0.30%	3.0
30SP40	1000	0.3	300	0.40%	4.0
30SP50	1000	0.3	300	0.50%	5.0
32SP10	1000	0.32	320	0.10%	1.0

3.5 Experimental setup

3.5.1 Rheological measurements

3.5.1.1 Controlled Shear Stress Method

Rheological measurements were conducted using an Anton Paar MCR 301 rotational rheometer. A vane spindle with four blades (40 mm in height) was used within a cylindrical cup (inner diameter of 28.939 mm) to determine the static yield stress and viscosity. A vane spindle is employed because the concentric cylindrical system is unsuitable for determining the rheological parameters due to the high-volume fraction of solids, which generates a force too high for the rheometer to keep the concentric cylinder in place. The rheometer and vane spindle geometry are shown in Figure **3-1**. After mixing, the measurements were performed at a constant temperature of 23 ± 1°C within 10 minutes. The cement paste was pre-sheared at a rate of 10 s^{-1} for 60 seconds, followed by a recovery period of 60 seconds. The standard Control Shear Stress (CSS) method involves applying shear stress while measuring the resulting shear rate. This study used a ramp of 3.33 pascals per second in the mix, and the corresponding shear rate was recorded. The static yield stress was determined at the shear stress threshold where the cement paste begins to flow, while the viscosity was calculated at the critical shear rate of 0.02 s^{-1}.

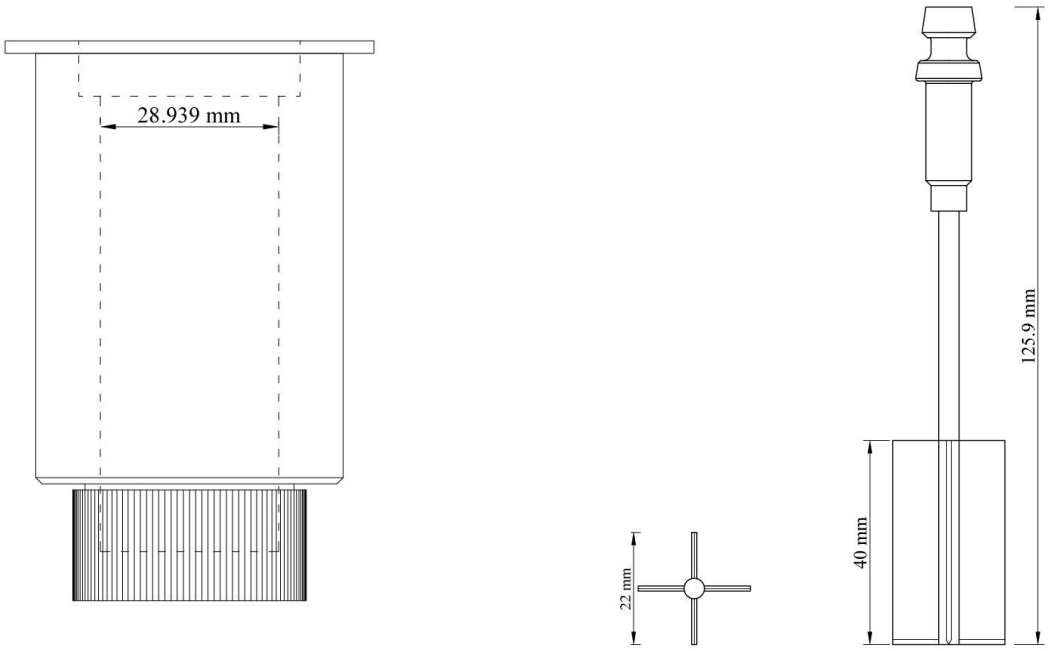

Figure 3-1: Rheological measurements – cylindrical cup and vane spindle geometry

3.5.2 Printability factors

This research employed a delta WASP 40100 3D printer featuring three extension arms and a manual feeding extruder, specifically designed for cementitious materials. Unlike the conventional extrusion systems, which rely on external pressure, this printer uses a pressure-free auger system, wherein the material is extruded solely with an auger mechanism without external pressure being applied to the cementitious materials. The manual feeding extruder operates with a torque output ranging from 1 to 2.5 Nm, and the printer has a build volume of 200 mm in diameter and 400 mm in height. Printability factors such as extrudability, shape retention, and buildability were examined to assess the printability behaviour of various mix proportions.

3.5.2.1 Extrudability

The extrudability was monitored to determine whether the cementitious material experienced clogging or discontinuous extrusion throughout the printing process of a single layer. This was assessed using two nozzle diameters (6mm and 8mm) at low and high printing speeds of 1000 mm/min and 3000 mm/min, respectively.

3.5.2.2 Shape retention

In this study, Shape retention was evaluated by printing a single-layer hollow cylinder with a diameter of 100 mm. The layer width (L_w) was chosen as the minimum width achievable, influenced by the nozzle size. For the 6 mm nozzle, the L_w was 7.2 mm, while for the 8 mm nozzle, it was 9.6 mm. The minimum widths, demonstrate high precision. However, it is important to note that the layer width is variable and can change according to design requirements. The shape retention factor (S_f) was calculated for all mix proportions (Chen et al., 2020; Panda et al., 2018). The shape retention factor (S_f) is defined as the ratio of the width of the printed layer (M_w) to the layer width (L_w) for a given nozzle (Buswell et al., 2018). To examine the effect of variable parameters such as nozzle diameter and printing speed, we analyzed two different nozzles (6 mm and 8 mm) at printing speeds ranging from 1000 mm/min to 3000 mm/min. The acceptable Sf for the mixtures was set at 1.2 (20 percent larger than L_w), ensuring that the extrusion widths within this tolerance could deliver prints with superior aesthetics and high precision.

$$\text{Shape retention factor}(S_{f6}) = \frac{(M_w)}{L_w(\,7.2\text{ mm})}$$

$$\text{Shape retention factor}(S_{f8}) = \frac{(M_w)}{L_w(9.6\text{ mm})}$$

3.5.2.3 Minimum buildability

In this study, a single-layer hollow cylinder with a 100 mm diameter was designed and sliced using Simplify 3D software. While layer height remains a variable parameter, adjustable based on specific design requirements, for the sake of identifying the procedure, layer heights equal to 8 mm and 4 mm were chosen for the 8 mm nozzle diameter. The weight of the upper layers exerts pressure on the bottom layer, affecting stability and causing dimensional variations. These variations depend on the extruder, the material properties, printer configurations and design requirements. This study focuses on the minimum buildability of a single layer (i.e., the ability of a printer to print one layer without deformations inspired by the slump). To quantify this, the single-layer buildability factor (S_{lf}) is defined as the ratio of the measured height (M_h) to the layer height (L_h). The rationale behind this approach is that S_{lf} reflects the minimum buildability performance, primarily determined by the printer's capabilities. Printing was halted if the mixes deviated from the intended design path or failed in extrusion. After 24 hours, the printed height was measured and reported.

$$\text{Single Layer Buildibility Factor } (S_{lf8}) = \frac{M_h}{L_h\ (8\text{ mm})}$$

$$\text{Single Layer Buildibility Factor } (S_{lf4}) = \frac{M_h}{L_h\ (4\text{ mm})}$$

3.5.3 Determination of printability zone

The printability zone of the manual feeding extruder is determined based on the printability limits correlating to the rheological properties of the cement paste mixes outlined in Table **3-2**. Hence, it is essential to define the printability limits, and they are tabulated in ***Table 3-3***.

Table 3-3: Printability limits and their corresponding criteria

Printability Limits	Definition
Maximum printable viscosity	The maximum viscosity that the printer can extrude without facing any interruptions or clogging, or significant variations in S_{lf}. This is determined as the median between the minimum value of non-extrudable viscosities (or viscosity exhibits S_{lf} less than 0.99) and the maximum value of extrudable viscosity with S_{lf} greater than 0.99.
Minimum printable viscosity	The minimum viscosity required for the cementitious material to maintain its acceptable shape retention factor. This is identified as the median between the minimum value of the viscosities exhibiting a S_f less than 1.2 and the maximum value of viscosities displaying a S_f that exceeds 1.2.
Minimum printable yield stress	The minimum yield stress required to print at least one layer with minimal dimensional variation in height. This is determined as the median between the minimum value of the yield stress exhibiting an S_{lf} greater than 0.99 and the maximum value of yield stress displaying an S_{lf} below 0.99.
Maximum printable yield stress	The maximum yield stress that the printer can extrude without facing any interruptions or clogging throughout the printing process. This is determined as the midpoint between the minimum value of non-extrudable yield stress and the maximum value of buildable yield stress.

Based on the observations made with printability factors and correlating them with yield stress and viscosity, the printability zone limits were determined for the manual feeding extruder. A complete framework for defining the printability zone is shown in Figure 3-2.

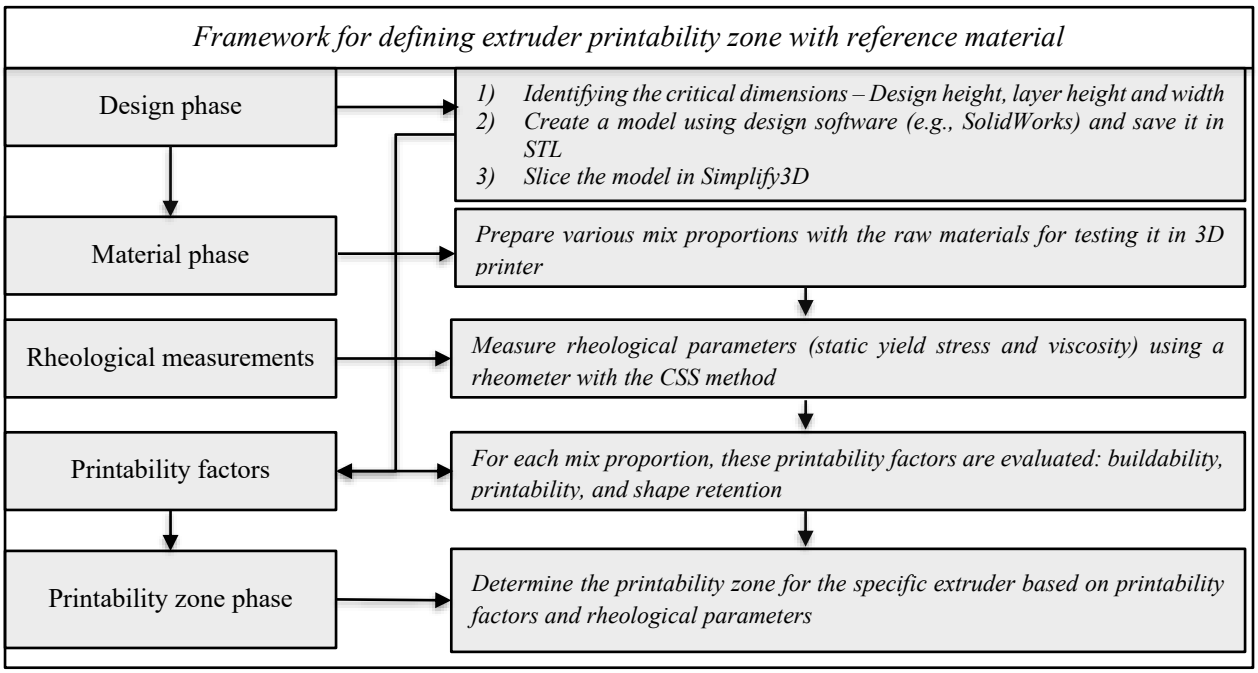

Figure 3-2:Framework for defining extruder printability zone

3.6 Results and Discussion

3.6.1 Rheological behaviour

The rheological parameters (i.e., yield stress and viscosity) are presented in Figure **3-3**. The results represent the arithmetic mean of three tested samples for each mix proportion. As anticipated, samples with a low w/c (i.e., w/c < 0.34) exhibited higher yield stress, while those with a high w/c (i.e., w/c > 0.34) demonstrated lower yield stress, ranging from 800 to 2400 Pascals. Among the tested mixes, 32SP00 showed the highest yield stress due to the higher solids concentration in the mix formulations. Adding 0.1 percent of superplasticizer in the mix (32SP10) reduced the yield stress by 500 Pa. This behaviour aligns with the findings of Coussot, who explained that, once the static yield stress is exceeded, the material begins to flow, resulting in structural breakdown and a corresponding decrease in viscosity at higher shear rates (Coussot, 2005).

The viscosity behaviour was observed using the Controlled Shear Rate (CSR) method, with the results summarized in Table **3-4**. For example, mix 32SP00 exhibited a viscosity of approximately 26 Pa.s at a shear rate of 25 s-1, which dropped to 9.8 Pa.s at 75 s-1. In contrast, mix 30SP30 showed a slightly lower viscosity of 23 Pa.s at 25 s-1, but exhibited a higher viscosity of 12.41 Pa.s at 75 s-1 compared to mix 32SP00. This observation underscores a potential limitation in determining printability limits based on viscosity at higher shear rates, particularly for the 3D printing of materials requiring the application of

superplasticizers, like clay and Supplementary Cementitious Materials (SCMs). Additionally, the rheological protocol is valid only in the fresh state and should be conducted within the initial setting time of the mix. Mixtures with high solid content may exceed this time window, resulting in invalid or unreliable rheological measurements. To address this, the viscosity was calculated at the critical shear rate of 0.02 s-1, representing the threshold beyond which the material initiates flow.

Table 3-4: Viscosities at different shear rates

Mix Proportions	Viscosity at 25 s^{-1} (Pa.s)	Viscosity at 75 s^{-1} (Pa.s)
32SP00	26.28	9.78
32SP10	23.63	9.80
30SP30	23.67	12.41
30SP40	20.98	11.73

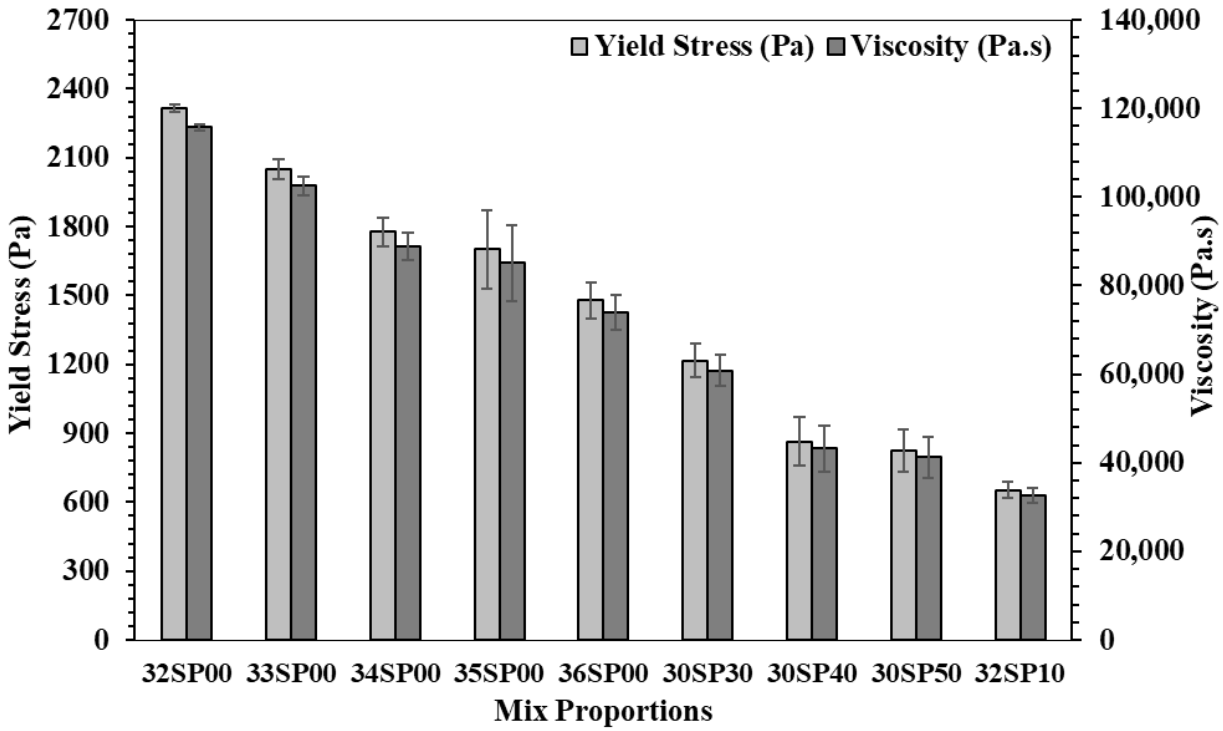

Figure 3-3: Rheological measurements – yield stress and viscosity

3.6.2 Printability limits

3.6.2.1 Minimum printable viscosity

The minimum printable viscosity is the lowest viscosity at which cement paste mixes can retain the shape retention criteria.

Effect of nozzle diameter

The difference between the printed and designed widths of all printed mixes was more pronounced with the 6 mm nozzle. This trend was observed regardless of the rheological properties of the printed mixes and is attributed to the effect of the reduction in the cross-sectional area of the nozzle diameter on the flow behaviour. According to the continuity equation, the velocity at the nozzle tip was 5.52 mm/s for the 8 mm nozzle, whereas it was 9.82 mm/s for the 6 mm nozzle. As shown in Figure **3-4**, the smaller diameter leads to a greater reduction in cross-sectional area, which consequently increases the extrusion velocity. This results in wider extrusions, deviating from the intended design requirements. Similar behaviour has been reported in the literature, where reductions in cross-section are associated with increased flow velocity (David et al., 2023; Wei et al., 2024). The difference between the printed widths and designed widths for 6 mm and 8 mm nozzle for 1000 mm/min are summarized in Table **3-5**.

Table 3-5: Effects of nozzle diameter in extrusion width

Mix Proportions	Viscosity (10^3 Pa.s)	Difference between printed and designed width (mm)	
		6 mm nozzle (D_w : 7.2mm)	8 mm nozzle (D_w : 9.6 mm)
30SP30	102.54 ± 3.59	2.4	0.6
32SP10	88.81 ± 1.74	2.5	1.1
33SP00	85.07 ± 2.1	3.1	1.5
30SP40	73.90 ± 5.27	4.4	2.6
34SP00	60.82 ± 3.18	5.7	2.8
35SP00	43.22 ± 8.52	8.3	4.7
30SP50	41.19 ± 4.59	11.0	7.1
36SP00	32.63 ± 3.92	8.6	4.9

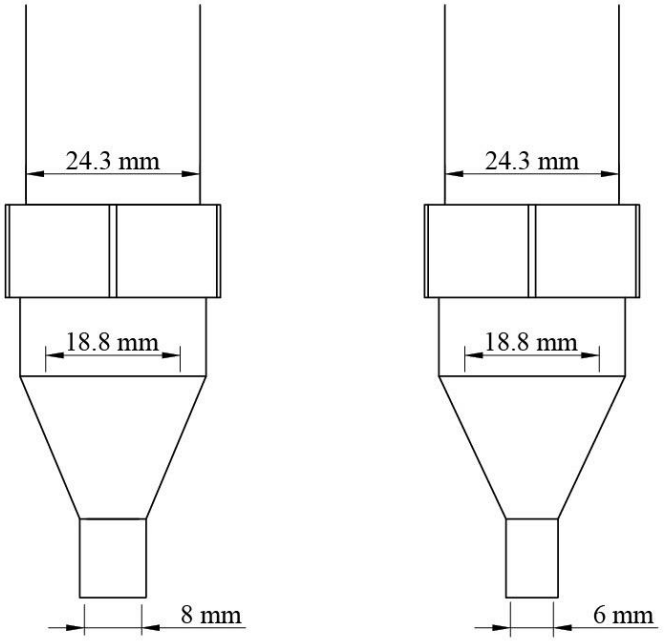

Figure 3-4: Inner diameter representation of 6 mm and 8 mm nozzle

Effect of printing speeds

It was observed that higher printing speeds resulted in narrower extrusion widths. This behaviour occurs because the flow rate cannot compensate for the required amount of material to be deposited at a given printing speed. This mismatch gets larger at high printing speeds, where an insufficient discharge occurs along the printing path resulting in a reduced printed width. The software proportionally adjusted the flow rate to compensate for the increased printing speed, and variations in extrusion widths remained minimal. Amongst the applied speeds,1000 mm/min consistently produced larger extrusions compared to the design width (Dw6 : 7.2 mm, Dw8 : 9.6 mm), irrespective of the rheological properties of the tested mixes. The maximum printable speed for the printer was 3000 mm/min, but higher speeds resulted in too small extrusion widths that never meet the acceptance shape retention criterion. Literature indicated that increasing the printing speed from 3000 mm/min to 7500 mm/min can reduce the extrusion width by half (Lee et al., 2019; H. Zhang et al., 2022). A printing speed of 1000 mm/min was selected for further investigation as it represents the worst-case scenario for studying the shape retention factor. The extrusion widths for different printing speeds with 6 mm and 8 mm nozzles are summarized in Table **3-6**.

Table 3-6: Effects of printing speed for 6 mm and 8 mm nozzle diameters

Mix Proportions	6 mm nozzle diameter (D_{w6} - 7.2 mm)			8 mm nozzle diameter (D_{w8} - 9.6 mm)		
	1000 mm/min	2000 mm/min	3000 mm/min	1000 mm/min	2000 mm/min	3000 mm/min
30SP30	9.6	9.2	9.0	10.2	9.6	9.3
32SP10	9.7	9.3	7.3	10.7	10.3	9.9
33SP00	10.3	10.2	9.00	11.1	10.9	10.7
30SP40	11.6	10.4	9.9	12.2	12.1	11.9
34SP00	12.9	12.6	11.9	12.4	12.2	11.9
35SP00	15.5	14.9	14.7	14.3	14.0	13.8
30SP50	18.9	15.4	15.4	16.7	15.1	14.6
36SP00	15.8	15.1	14.7	14.5	13.8	13.7

Discussion of Shape Retention factor (S_f)

The mixes with a viscosity of more than 80000 Pa.s exhibited the lowest shape retention factor, below 1.2 (20 percent). Conversely, mixes with viscosities below 45000 Pa.s demonstrated shape retention factors greater than 1.5 and 2 for the 8 mm and 6 mm nozzle diameters, respectively. Higher deviations from Sf = 1 indicate poorer shape retention behaviour of the printed paste. This highlights the critical role of viscosity in shape retention. When viscosity falls below the minimum printable threshold, the paste exhibits excessive deformation due to lower internal friction, resulting in inadequate structural stability and shape retention (Chen et al., 2020; Panda et al., 2018). The shape retention factors for 6 mm and 8 mm nozzles at a printing speed of 1000 mm/min for all viscosities are tabulated in Table **3-7**.

Table 3-7: Shape retention factors for 6 mm and 8 mm nozzle

Mix Proportions	Viscosity (10^3 Pa.s)	Shape Retention factor (S_f)	
		6 mm	8 mm
30SP30	102.54 ± 3.59	1.33	1.06
32SP10	88.81 ± 1.74	1.34	1.11
33SP00	85.07 ± 2.1	1.43	1.16
30SP40	73.90 ± 5.27	1.61	1.27
34SP00	60.82 ± 3.18	1.79	1.29
35SP00	43.22 ± 8.52	2.16	1.49

30SP50	41.19 ± 4.59	2.53	1.74
36SP00	32.63 ± 3.92	2.19	1.51

Mixes that demonstrated shape retention within a 20 percent tolerance (Sf <1.2) were printable only with an 8 mm nozzle diameter. Due to the reduction in cross-sectional area, the same mixes printed with a 6 mm nozzle diameter exhibited shape retention only within a 50 percent tolerance. As the minimum printable viscosity criterion was set at Sf=1.2, the 6 mm nozzle diameter is deemed unsuitable. Hence, there is no printability zone for the 6 mm nozzle diameter. Details of mixes capable of retaining their shape, along with their rheological properties, is presented in Table **3-8**. The minimum printable viscosity for an 8 mm nozzle diameter is the median between mix 30SP30 and mix 34SP00, calculated and rounded off to 80000 Pa.s within acceptable tolerances. The minimum printable viscosity plot for the 8 mm nozzle diameter is shown in Figure **3-5**. The white region in the plot defines the unacceptable mixes that fail to retain the shape as per the design for the manual feeding extruder.

Table 3-8: Correlation of viscosity to shape retention

Mix Proportions	Viscosity (10^3 Pa.s)	Tolerance criteria (8 mm)	Shape Retention
32SP00	115.76 ± 0.71	-	Not Extrudable
30SP30	102.54 ± 3.59	1.08 < 1.2	Acceptable shape retention
32SP10	88.81 ± 1.74	1.11 < 1.2	Acceptable shape retention
33SP00	85.07 ± 2.1	1.16 < 1.2	Acceptable shape retention
30SP40	73.90 ± 5.27	1.27 > 1.2	Unacceptable shape retention
34SP00	60.82 ± 3.18	1.29 > 1.2	Unacceptable shape retention
35SP00	43.22 ± 8.52	1.49 > 1.2	Unacceptable shape retention
30SP50	41.19 ± 4.59	1.74 > 1.2	Unacceptable shape retention
36SP00	32.63 ± 3.92	1.51 > 1.2	Unacceptable shape retention

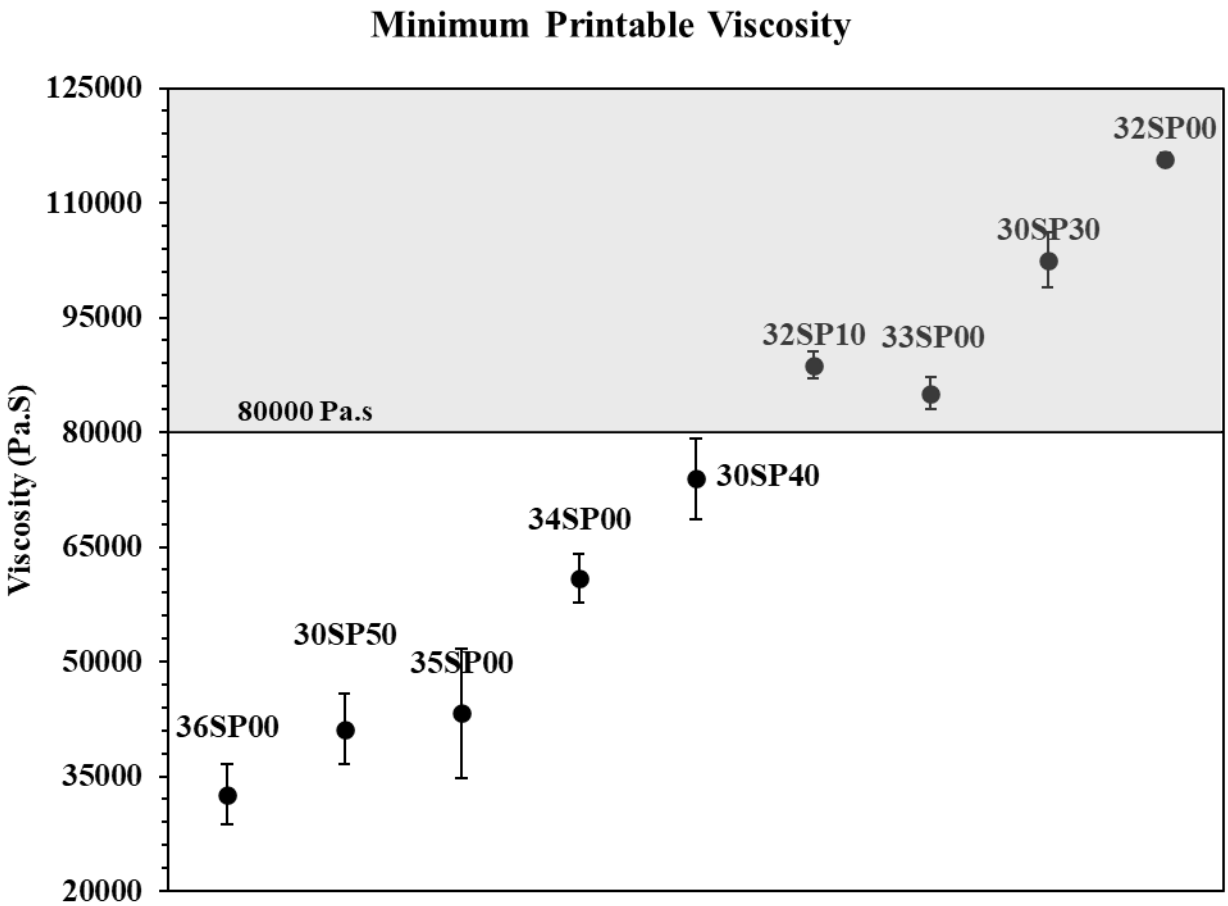

Figure 3-5: Minimum printable viscosity plot for 8 mm nozzle

3.6.2.2 Maximum printable viscosity

The maximum printable viscosity refers to the highest viscosity at which cementitious materials can effectively flow through the nozzle during 3D printing. Three distinct outcomes were observed during the process: successful extrusion, partial and complete extrusion failure. Mix 32SP00, characterized by a high viscosity (greater than 110000 Pa.s), demonstrated complete extrusion failure from the very first layer with a 6 mm nozzle diameter regardless of the printing speeds, as labelled as 'B' in Figure **3-6**. A similar trend was observed with the 8 mm nozzle diameter. At a printing speed of 1000 mm/min, the material could not achieve a complete shape, whereas at 3000 mm/min, it was able to form a complete shape but failed to follow the intended path, resulting in complete extrusion failure at both printing speeds. This phenomenon is attributed to auger rotations, which increase with printing speed, allowing the material to form a shape; however, the high viscosity (greater than 110000 Pa.s) prevents from sufficient flow. The printed models corresponding to 1000 mm/min and 3000 mm/min are labelled as 'C' and 'D' in Figure **3-6**, respectively.

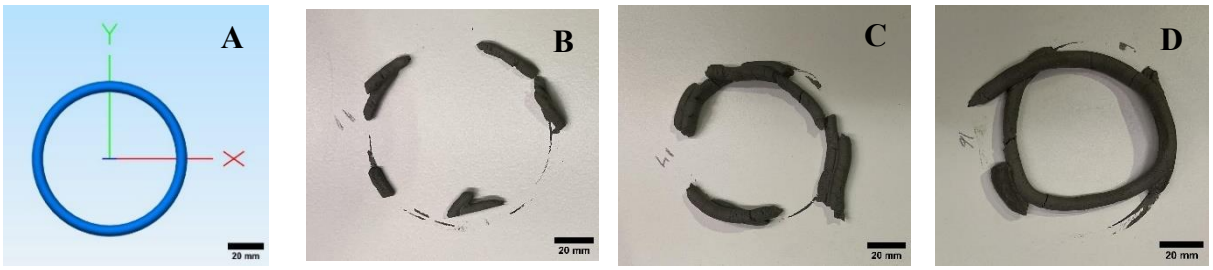

Designed and printed 6 mm nozzle dia model

Printed 8 mm nozzle dia with 1000 and 3000 mm/min

Figure 3-6: Complete extrusion failure of mix 32SP00

It was observed that mix 30SP30, with a viscosity of 102500 Pa.s, was unable to extrude the full height of the sample with the 8 mm layer height. In contrast, the same mix was successfully extruded at a 4 mm layer height. This behaviour is attributed to the increased frictional forces between the material and the walls of the extruder pipe, which led to partial extrusion failure at larger layer heights. In such cases, higher extrusion pressures are required to overcome these frictional forces and maintain continuous material flow. This observation is consistent with findings in the literature, which report that mixes with low water-to-cement ratios tend to exhibit higher viscosity and a limited ability to form a lubrication layer. This leads to increased frictional forces within the extrusion system, ultimately resulting in partial or complete extrusion failure (Paritala et al., 2023; Roussel, 2018). The correlation of maximum printable viscosity and extrudability for 8 mm and 4 mm layer heights are summarized in Table **3-9** and Table **3-10** respectively.

Table 3-9: Correlation of viscosity and extrudability for 8 mm layer height

Mix Proportions	Viscosity (10^3 Pa.s)	Tolerance criteria (8 mm)	Maximum extrudability
32SP00	115.76 ± 0.71	-	Complete extrusion failure
30SP30	102.54 ± 3.59	0.98 ± 0.01 < 0.99	Partial extrusion failure
32SP10	88.81 ± 1.74	1.02 ± 0.01 > 0.99	Extrudable
33SP00	85.07 ± 2.1	1.01 ± 0.01 > 0.99	Extrudable

Table 3-10: Correlation of viscosity and extrudability for 4 mm layer height

Mix Proportions	Viscosity (10^3 Pa.s)	Tolerance criteria (4 mm)	Maximum extrudability
32SP00	115.76 ± 0.71	-	Complete extrusion failure
30SP30	102.54 ± 3.59	1.02 ± 0.02 > 0.99	Extrudable
32SP10	88.81 ± 1.74	1.02 ± 0.01 > 0.99	Extrudable

33SP00	85.07 ± 2.1	1.03 ± 0.02 > 0.99	Extrudable

The maximum printable viscosity for 8 mm nozzle with an 8 mm layer height was determined as the median value between the viscosities of mix 30SP30 and mix 32SP10, calculated and rounded off to 96000 Pa.s. For the 4 mm layer height, the maximum printable viscosity was similarly determined as the median value between the mix 32SP00 and 30SP30, resulting in a value of 110000 Pa.s. These threshold values are illustrated in Figure **3-7** and Figure **3-8**, which present the printable viscosity limits for both layer heights. The gray zone depicts the range of extrudable mixes and is defined by the uppermost boundary line at 110000 Pa.s and 96000 Pa.s for 4 mm and 8 mm layer heights, respectively, beyond which mixes become non-extrudable (white zone) when using a manually fed extruder.

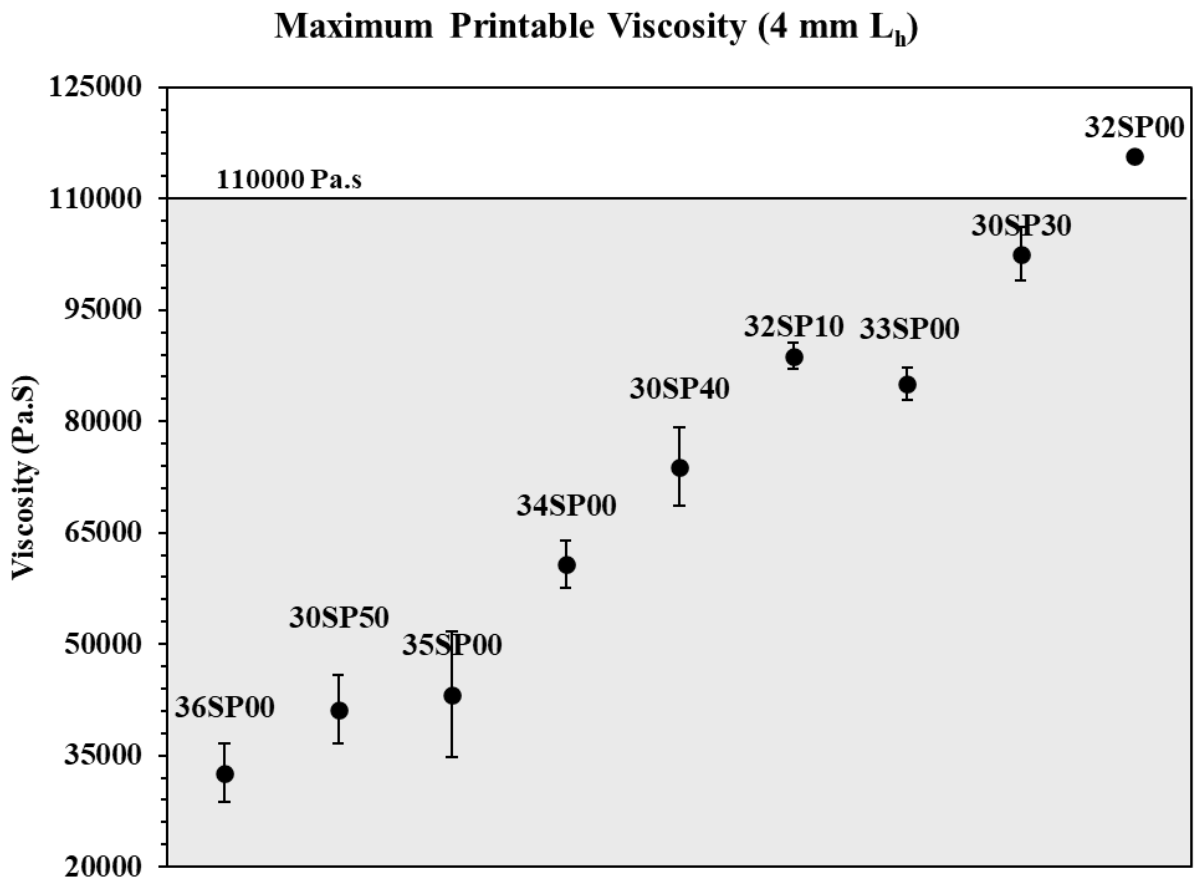

Figure 3-7: Maximum printable viscosity plot for 4 mm L_h

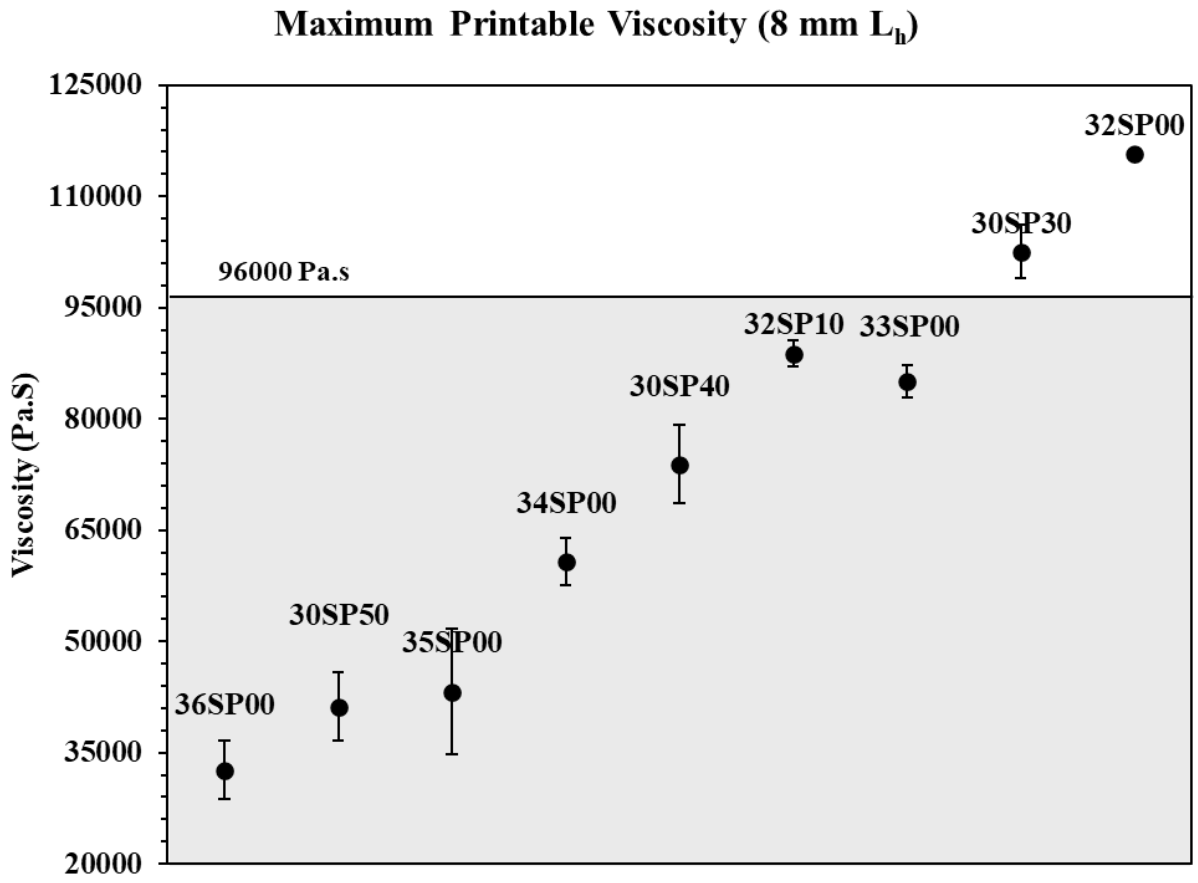

Figure 3-8: Maximum printable viscosity plot for 8 mm L_h

3.6.2.3 Minimum printable yield stress

The minimum yield stress is the threshold at which mixes can successfully print at least a single layer while maintaining minimal dimensional height variations within the tolerance ($S_{lf} > 0.99$).

Effect of layer height

For the 8 mm layer height, mixes with a yield stress exceeding 1040 Pa exhibited minimal dimensional variation, achieving an Slf factor greater than 0.99. In contrast, for a 4 mm layer height, mixes with yield stress above 740 Pa maintained an Slf of more than 0.99. This difference is primarily due to the slumped weight, which is approximately twice as high for the 8 mm layer height compared to the 4 mm layer height. The increased layer volume/weight at 8 mm introduces greater dimensional variations, requiring a minimum yield stress of 1040 Pa to support the slumped weight. It is important to note that, the higher layer volume will pose challenges for the mixes in supporting the weight of the upper layers within a short time frame, leading to reduced buildability. The 36SP00 mix characterized by the lowest yield stress of 650 Pa,

displayed a Slf factor of 0.95, indicating significant dimensional variation even under its own weight for both layer heights. Table **3-11** summarizes the measured height and Slf values for the 8 mm and 4 mm layer heights.

Table 3-11: Minimum printable assessment for 8 mm nozzle diameter

Mix Proportions	Static Yield Stress (Pa)	8 mm layer height		4 mm layer height	
		M_h	S_{lf}	M_h	S_{lf}
30SP30	2050.71	7.81 ± 0.08	0.98 ± 0.01	4.08 ± 0.1	1.02 ± 0.02
32SP10	1776.17	8.17 ± 0.04	1.02 ± 0.01	4.1 ± 0.03	1.02 ± 0.01
33SP00	1701.31	8.05 ± 0.08	1.01 ± 0.01	4.1 ± 0.09	1.03 ± 0.02
30SP40	1477.95	8.12 ± 0.11	1.02 ± 0.01	4.14 ± 0.11	1.03 ± 0.03
34SP00	1216.49	7.93 ± 0.17	0.99 ± 0.02	4.11 ± 0.09	1.03 ± 0.02
35SP00	864.30	7.59 ± 0.14	0.95 ± 0.02	4.21 ± 0.03	1.05 ± 0.01
30SP50	823.90	7.77 ± 0.15	0.97 ± 0.02	4.06 ± 0.12	1.01 ± 0.03
36SP00	652.64	6.94 ± 0.20	0.87 ± 0.02	3.85 ± 0.18	0.96 ± 0.05

The minimum printable yield stress with the 8 mm layer height is the median value point of yield stresses between mix 34SP00 and mix 35SP00, calculated and rounded off to 1040 Pa. The minimum printable yield stress for the 4 mm layer height is the median value between mix 30SP50 and 36SP00, calculated and rounded off to 740 Pa. The difference of 300 Pa between 8 mm and 4 mm layer height is primarily due to the higher layer volume and increased flow rate for one single layer. The minimum yield stress plot for 8 mm is illustrated in Figure **3-9** and Figure **3-10**, where the white region represents the unacceptable yield stress (less than 1040 Pa and 740 Pa) that is unable to support even a single layer. The correlation between buildability and yield stress for the 8 mm and 4 mm layer height are summarized in Table **3-12** and Table **3-13**.

Table 3-12: Correlation of yield stress to minimum buildability for 8 mm layer height

Mix Proportions	Static yield stress (Pa)	Tolerance criteria (8 mm L_h)	Minimum buildability
30SP30	2050.71 ± 71.80	0.98 ± 0.01 < 0.99	Partial Extrusion Failure
32SP10	1776.17 ± 34.81	1.02 ± 0.01 > 0.99	Acceptable
33SP00	1701.31 ± 42.00	1.01 ± 0.01 > 0.99	Acceptable
30SP40	1477.95 ± 105.37	1.02 ± 0.01 > 0.99	Acceptable
34SP00	1216.49 ± 63.66	0.99 ± 0.02 = 0.99	Acceptable

35SP00	864.30 ± 170.44	0.95 ± 0.02 < 0.99	Unacceptable
30SP50	823.90 ± 91.88	0.97 ± 0.02 < 0.99	Unacceptable
36SP00	652.64 ± 78.31	0.87 ± 0.02 < 0.99	Unacceptable

Table 3-13: Correlation of yield stress to minimum buildability for 4 mm layer height

Mix Proportions	Static yield stress (Pa)	Tolerance criteria (4 mm L_h)	Minimum buildability
30SP30	2050.71 ± 71.80	1.02 ± 0.02 > 0.99	Acceptable
32SP10	1776.17 ± 34.81	1.02 ± 0.01 > 0.99	Acceptable
33SP00	1701.31 ± 42.00	1.03 ± 0.02 > 0.99	Acceptable
30SP40	1477.95 ± 105.37	1.03 ± 0.03 > 0.99	Acceptable
34SP00	1216.49 ± 63.66	1.03 ± 0.02 > 0.99	Acceptable
35SP00	864.30 ± 170.44	1.05 ± 0.01 > 0.99	Acceptable
30SP50	823.90 ± 91.88	1.01 ± 0.03 > 0.99	Acceptable
36SP00	652.64 ± 78.31	0.96 ± 0.05 < 0.99	Unacceptable

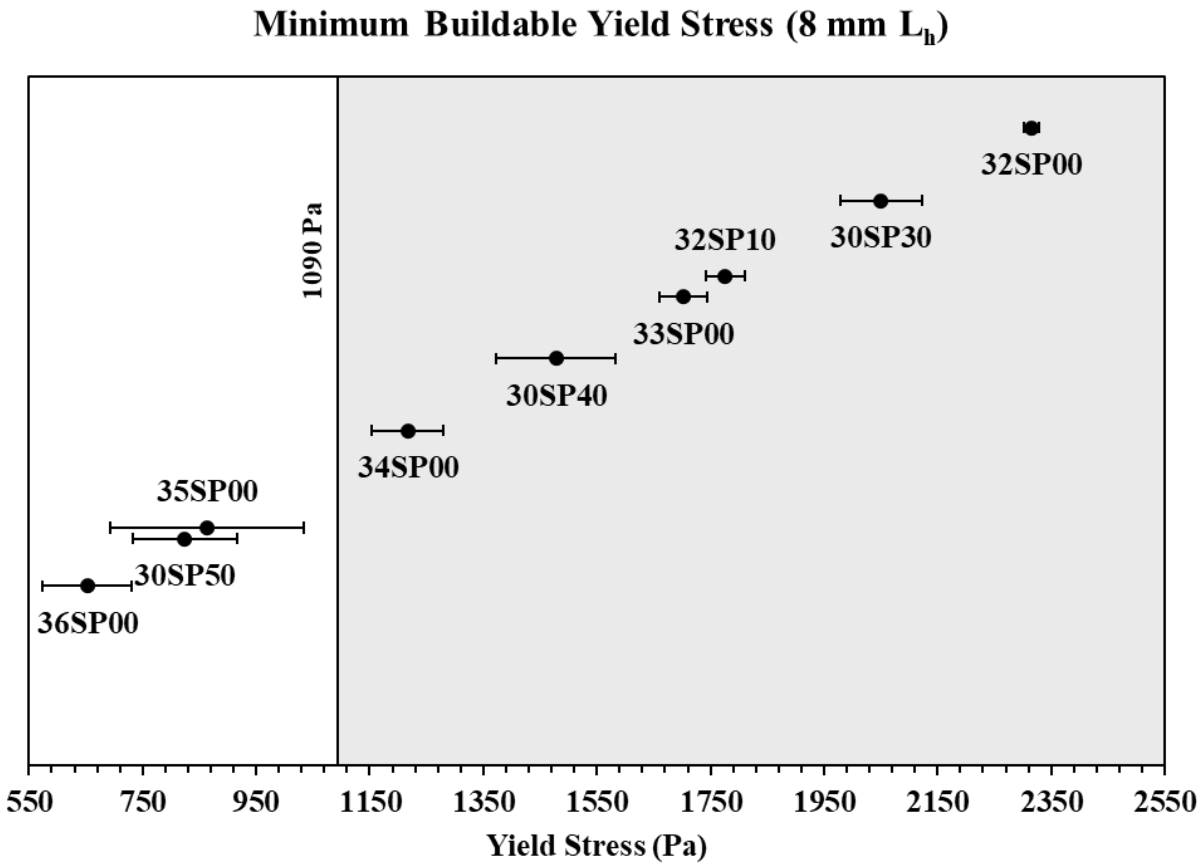

Figure 3-9: Minimum printable yield stress plot for 8 mm layer height

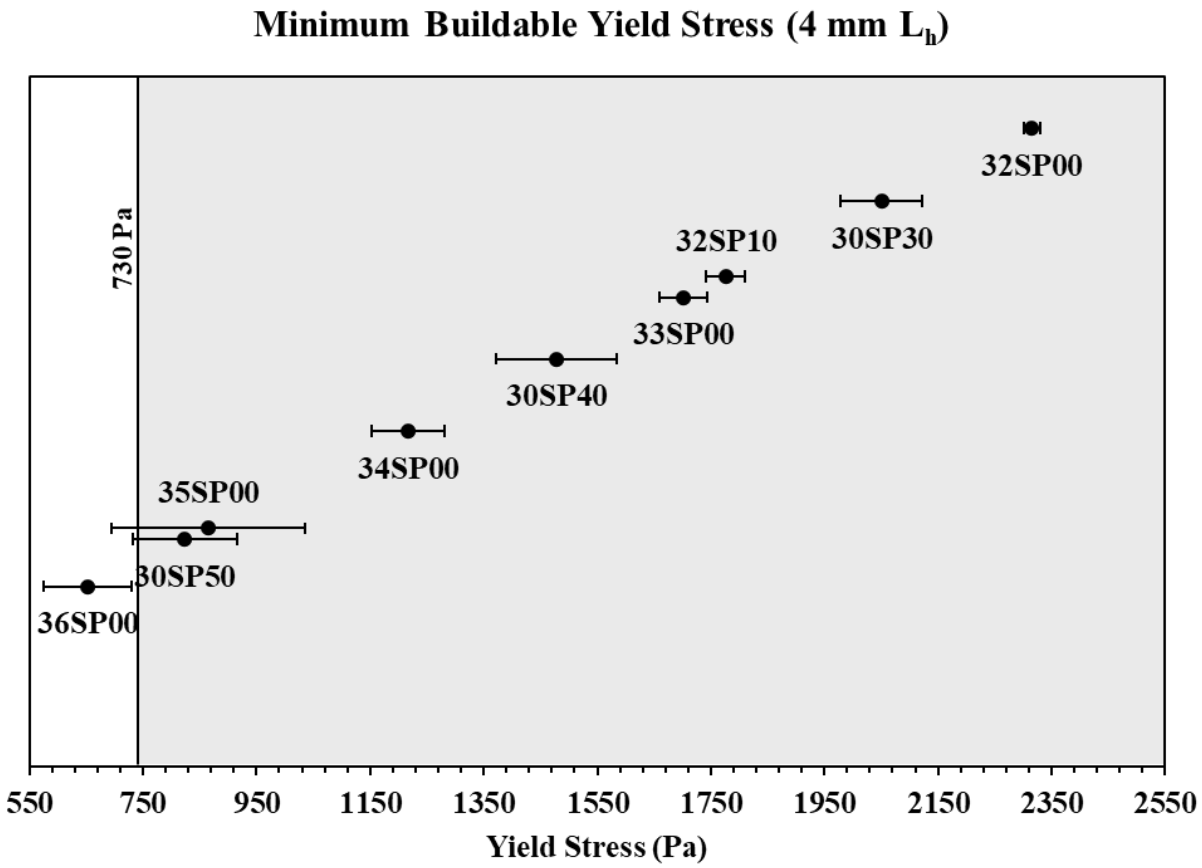

Figure 3-10: Minimum printable yield stress plot for 4 mm layer height

3.6.2.4 Maximum printable yield stress

The maximum printable yield stress represents the threshold beyond which the printer cannot operate without interruptions or clogging. It is important to note that open time is the time interval during which the material's properties remain consistent within acceptable tolerances. In this research, the entire printing duration remained within the open time for all mixtures that remained in a fresh state throughout the process. Consequently, open time was not a significant consideration in this study. However, literature suggests that open time is a critical factor for 3D printing (Chen et al., 2021; J. Zhang et al., 2019). Studies by Rehman et al. and Panda et al. have shown that material extrusion becomes unfeasible beyond a specific static yield stress limit (Panda & Tan, 2018; Rehman et al., 2020). It should also be noted that the application of external pressure, such as compressed air with a piston assembly, can enable mixes with high static yield stress to be extruded, as the shear forces can exceed the static yield stress of the cement paste mix (Panda & Tan, 2018). Mix 32SP00, which exhibited the highest yield stress of 2300 Pa, experienced complete extrusion failure. In contrast, mix 30SP30, despite demonstrating partial extrusion, was able to extrude continuously,

without experiencing clogging or discontinuity. The correlation between the yield stress and extrudability is tabulated in Table 14.

Table 3-14: Correlation of yield stress with non-extrudable and acceptable mixes

Mix Proportions	Static yield stress (Pa)	Maximum extrudability
32SP00	2315.23 ± 14.26	Clogged
30SP30	2050.71 ± 71.80	Unclogged and continuous extrusion
32SP10	1776.17 ± 34.81	Extrudable
33SP00	1701.31 ± 42.00	Extrudable

The maximum printable yield stress is the median value point of yield stresses between mix 32SP00 and 30SP30, calculated and rounded off to 2185 Pa. In terms of buildability, materials exceeding 2185 Pa require additional pressure to extrude and maintain the dimensions. However, this introduces concerns regarding segregation, making it essential to study its effects under increased pressure. It is important to study the effect of segregation with the additional pressure. The maximum yield stress plot is illustrated in Figure **3-11**, where the white-coloured region represents the unacceptable yield stress (more than 2185 Pa) that prevents the extrusion of even a single layer.

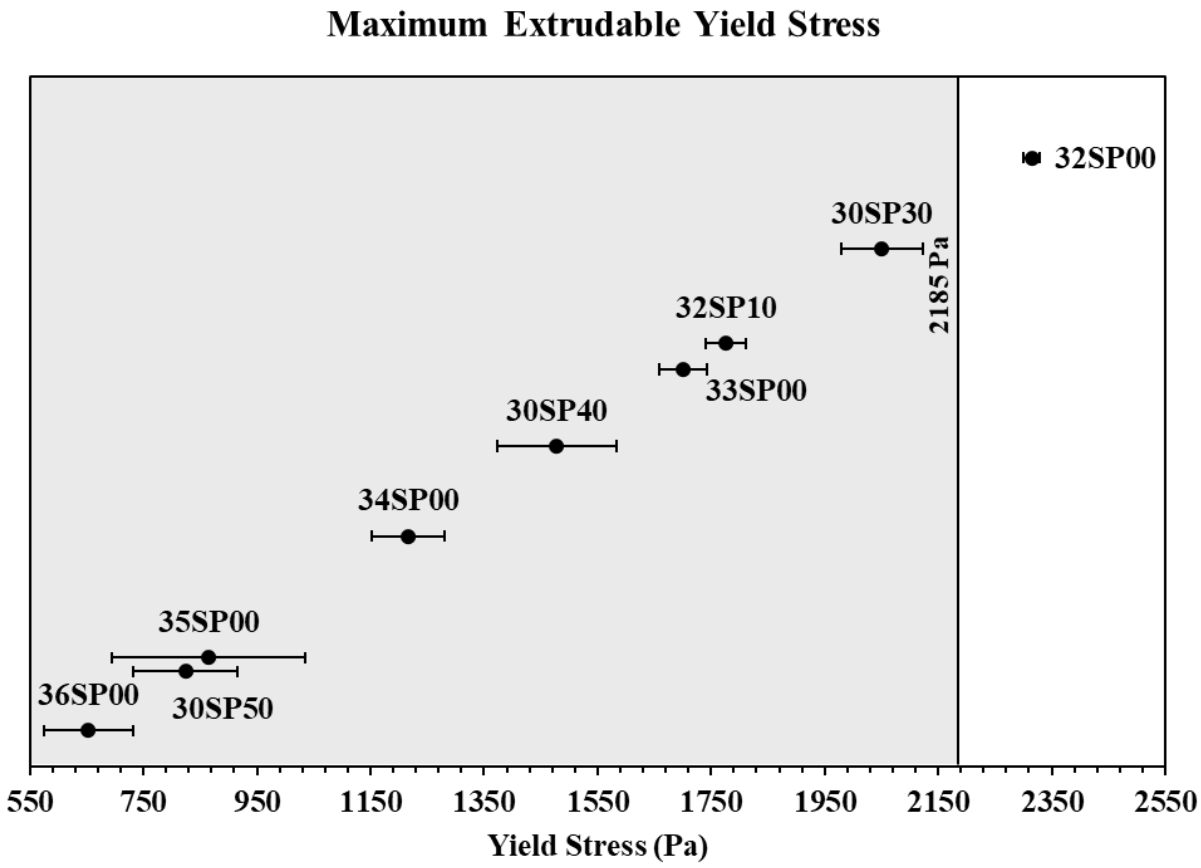

Figure 3-11: Maximum printable yield stress plot

3.6.3 Printability zone – manual feeding extruder

The printability plot correlates rheological properties (static yield stress and viscosity) with printability factors (extrudability, shape retention and buildability) for a given cementitious 3D printer. The plot uses static yield stress versus viscosity values calculated at 0.02 s^{-1}, with limits defined by the performance of printability factors. For extrudability, materials exceeding the maximum printable threshold of yield stress and viscosity are unable to extrude through the nozzle. The minimum viscosity (minimum printable) represents the ability to retain its shape under its own weight, while the minimum yield stress reflects the ability to print one single layer without deformation. The limits are determined based on criteria established for each printability factor. While determining the shape retention acceptance criterion heavily depends on the printing precision of a given 3D model (i.e., the object in question), for the sake of experimentation and to facilitate the development of the test method, the acceptable shape retention factor is set at 1.2, and the minimum printable viscosity is defined as the median value between materials with acceptable and

unacceptable performance. Rheological plots correlating yield stress and viscosity were developed to identify the four printability limits for the 8 mm nozzle, as shown in Figure **3-12**.

Based on the linear correlation between yield stress and viscosity, as well as the positioning of the maximum and minimum printable boundary lines, the printability plot delineates four distinct zones, each characterized by specific rheological properties, tolerance criteria, and printability factors, irrespective of layer height and nozzle size:

1. Zone 1: This zone lies below the minimum printable yield stress and minimum printable viscosity. Mixtures in this zone fail to meet all acceptable criteria for 3D printing and exhibit poor shape retention, and inadequate buildability.
2. Zone 2 (Minimum buildable zone): This zone lies above the minimum printable yield stress but below the minimum printable viscosity. The mixes in this zone can print a single-layered model in the fresh state however, their precision is not guaranteed as the extrusion width exceeds 20 percent ($Sf > 1.2$).
3. Zone 3 (printability zone): This is the optimal zone for successful 3D printing. This zone is situated between the maximum and minimum printable yield stress and viscosity boundary lines. It encompasses mixtures that are extrudable, maintain their shape, and can print a single layer without minimal dimensional variations. In rheological terms, zone 3 lies above the minimum printable yield stress and viscosity but below the maximum printable yield stress and viscosity. It is noteworthy that as the design height (i.e., the height of the object in question) increases, the area of Zone 3 shrinks due to the rise in the minimum required printable yield stress. This phenomenon will be explored in greater detail in a future study.
4. Zone 4 (non-extrudable zone): This zone is defined by mixtures with properties exceeding the maximum printable yield stress and viscosity. These materials require additional pressure to extrude and without additional pressure, they fail in minimum buildability and shape retention ($Slf < 0.99$ and $Sf < 1$).

In this study, a linear relationship was observed between static yield stress and viscosity, attributed to the rheological properties being measured in the material's rest state. The acceptable printability zone (Zone 3) for a 3D printer, representing the balance between extrudability, shape retention, and minimum buildability, is located in the middle range. A similar pattern was observed in the research by Tay et al. who examined the printability region using slump and slump flow test values. Their findings also revealed a linear correlation between slump and slump flow, with the acceptable printability region situated in the middle range of these values (Tay et al., 2019).

The nozzle diameter and layer height significantly influenced the position of printability boundary lines. The high peak velocity of the 6 mm nozzle diameter rendered it unsuitable for 3D printing with cementitious materials. In contrast, the 8 mm nozzle diameter produced an acceptable 3D printing outcome, and its printability zone was determined for 4 mm and 8 mm layer heights, as illustrated in Figure 3-13and Figure **3-12**, respectively. The increased layer volume for the 8 mm layer height posed challenges for mixes with yield stress values between 740 Pa to 1040 Pa to support their self-weight. Zone 4 was classified as non-extrudable at static yield stress above 2185 Pa, and at viscosities exceeding 110000 Pa.s and 96000 Pa.s for 4 mm and 8 mm layer heights, respectively. Zone 1 is non-printable below a static yield stress of 740 Pa and 1040 Pa for 4 mm and 8 mm layer height, respectively and viscosity lower than 80000 Pa.s. It is important to note that the defined limits for single-layer printing identify the printability zone of a given 3D printer, which is solely determined by its extrusion system. However, the printability zone is also influenced by design height and material properties. The effect of the mentioned factors will be extensively discussed in a separate study.

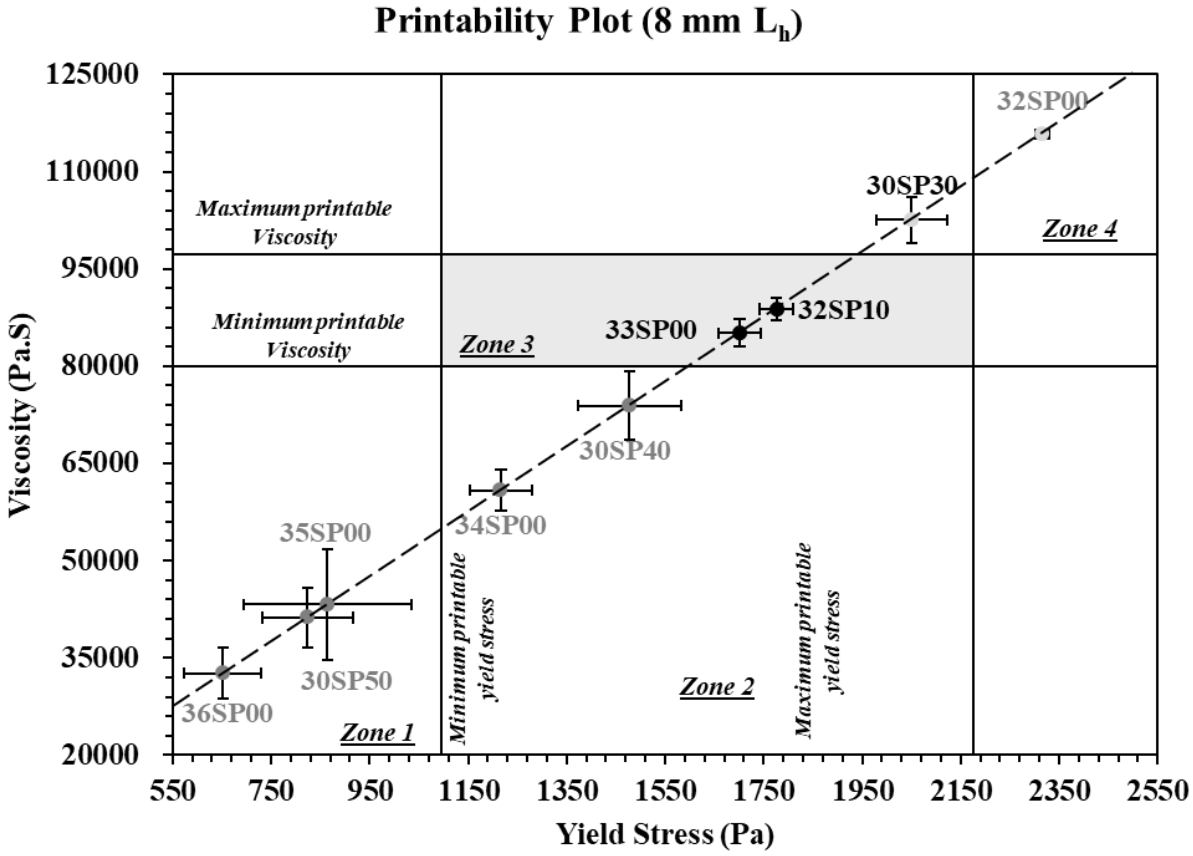

Figure 3-12: Printability plot for manual feeding extruder for an 8 mm layer height

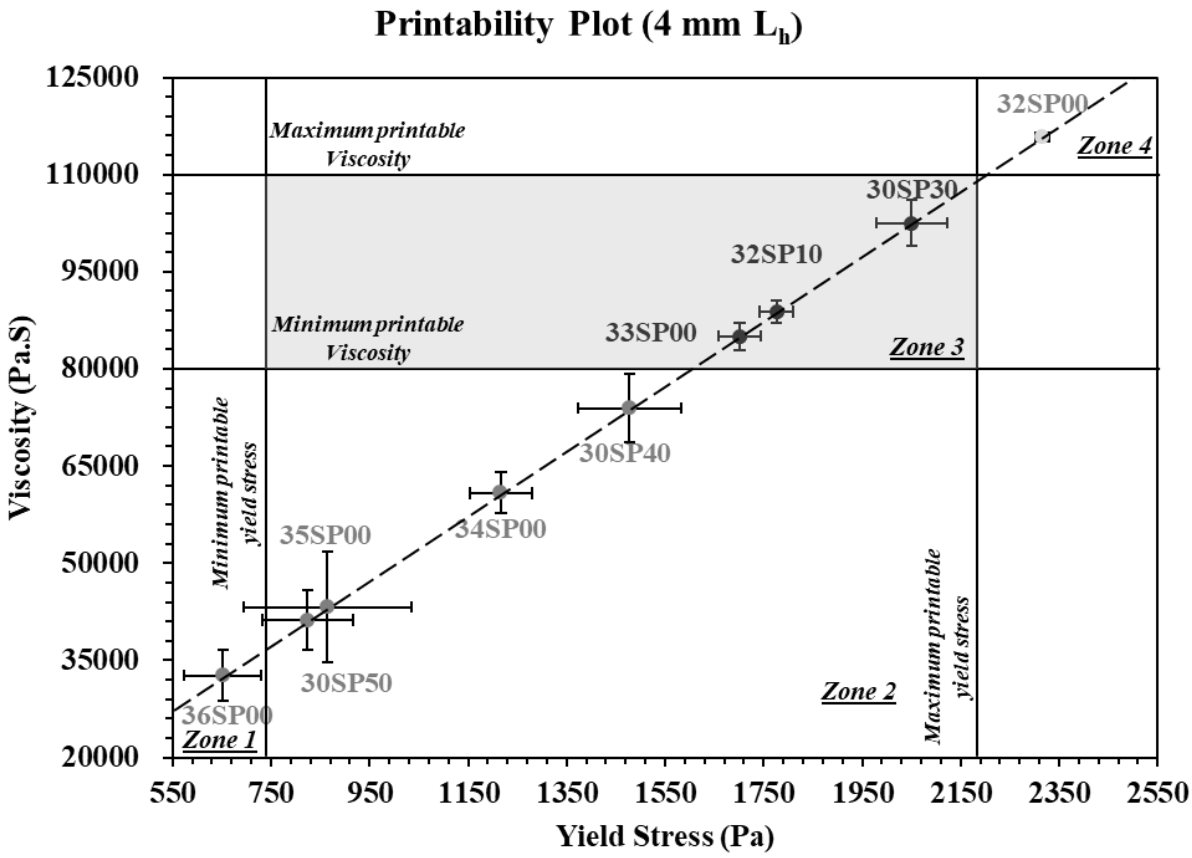

Figure 3-13: Printability plot for manual feeding extruder for a 4 mm layer height

3.7 Conclusion and future works

This study established a standardized methodology to determine the printability zone of a non-pressurized extruder using a Delta WASP printer by correlating rheological properties with key printability factors. Portland Cement (PC) was employed as a benchmark to define rheological printability limits necessary for printing a single layer within acceptable tolerances. The incorporation of superplasticizers extended the continuum of mixes by broadening the range of viable rheological properties. Quantitative assessments of shape retention and buildability for a single layer demonstrated their relevance to meet diverse design requirements. The results highlight that nozzle geometry significantly influences shape retention; the 6 mm nozzle diameter was found unsuitable for single-layer printing due to the high peak velocity. Likewise, layer height directly impacts buildability, as increased height adds weight, raising the risk of deformation. Based on these findings, both printability limits and corresponding printability zones were identified. This methodology facilitates the evaluation of various mix designs, including those incorporating SCMs, enabling predictive insights into printability behaviour from rheological characteristics. Future research

will focus on the effects of material properties and structural height on buildability and will extend the proposed methodology to pressurized extruders, thereby expanding the practical applications of 3D printing with cementitious materials.

Acknowledgements

The authors gratefully acknowledge the financial support received from the New Frontier Research Fund (NFRF) for providing the fund and Steven Beites for collaborating on this project.

3.8 References

Ambily, P. S., Kaliyavaradhan, S. K., & Rajendran, N. (2024). Top challenges to widespread 3D concrete printing (3DCP) adoption–A review. *European Journal of Environmental and Civil Engineering*, *28*(2), 300–328. https://doi.org/10.1080/19648189.2023.2213294

Buswell, R. A., Leal de Silva, W. R., Jones, S. Z., & Dirrenberger, J. (2018). 3D printing using concrete extrusion: A roadmap for research. *Cement and Concrete Research*, *112*, 37–49. https://doi.org/10.1016/j.cemconres.2018.05.006

Chandra Paul, S., Basit, M. A., Hasan, N. M. S., Dey, D., & Panda, B. (2023). 3D printing of geopolymer mortar: Overview of the effect of mix design and printing parameters on the strength. *Materials Today: Proceedings*. https://doi.org/10.1016/j.matpr.2023.04.292

Chen, Y., Chaves Figueiredo, S., Li, Z., Chang, Z., Jansen, K., Çopuroğlu, O., & Schlangen, E. (2020). Improving printability of limestone-calcined clay-based cementitious materials by using viscosity-modifying admixture. *Cement and Concrete Research*, *132*. https://doi.org/10.1016/j.cemconres.2020.106040

Chen, Y., He, S., Zhang, Y., Wan, Z., Çopuroğlu, O., & Schlangen, E. (2021). 3D printing of calcined clay-limestone-based cementitious materials. *Cement and Concrete Research*, *149*, 106553–106553. https://doi.org/10.1016/J.CEMCONRES.2021.106553

Coussot, Philippe. (2005). *Rheometry of pastes, suspensions, and granular materials: Applications in industry and environment*. Wiley.

David, M., Freund, N., Dröder, K., & Lowke, D. (2023). The effects of nozzle diameter and length on the resulting strand properties for shotcrete 3D printing. *Materials and Structures*, *56*(8). https://doi.org/10.1617/s11527-023-02246-1

Feldmann, F. G. (2022). Towards Lean Automation in Construction—Exploring Barriers to Implementing Automation in Prefabrication. *Sustainability (Basel, Switzerland)*, *14*(19), 12944–12944. https://doi.org/10.3390/su141912944

Jiang, Y., Zhao, D., Wang, D., & Xing, Y. (2019). Sustainable performance of buildings through modular prefabrication in the construction phase: A comparative study. *Sustainability (Basel, Switzerland)*, *11*(20), 5658–5658. https://doi.org/10.3390/su11205658

Kazemian, A., Yuan, X., Cochran, E., & Khoshnevis, B. (2017). Cementitious materials for construction-scale 3D printing: Laboratory testing of fresh printing mixture. *Construction and Building Materials*, *145*, 639–647. https://doi.org/10.1016/j.conbuildmat.2017.04.015

Khan, M. S., Sanchez, F., & Zhou, H. (2020). 3-D printing of concrete: Beyond horizons. *Cement and Concrete Research*, *133*. https://doi.org/10.1016/j.cemconres.2020.106070

Kondepudi, K., & Subramaniam, K. V. L. (2021). Formulation of alkali-activated fly ash-slag binders for 3D concrete printing. *Cement and Concrete Composites*, *119*. https://doi.org/10.1016/j.cemconcomp.2021.103983

Lee, H., Kim, J. H. J., Moon, J. H., Kim, W. W., & Seo, E. A. (2019). Evaluation of the mechanical properties of a 3D-printed mortar. *Materials*, *12*(24). https://doi.org/10.3390/ma12244104

Llatas, C. (2011). A model for quantifying construction waste in projects according to the European waste list. *Waste Management*, *31*(6), 1261–1276. https://doi.org/10.1016/j.wasman.2011.01.023

Mehta, P. K. (Povindar K.). (2014). *Concrete microstructure, properties, and materials* (P. J. M. Monteiro, Ed.; 4th ed.). McGraw-Hill.

Muthukrishnan, S., Ramakrishnan, S., & Sanjayan, J. (2021). Effect of alkali reactions on the rheology of one-part 3D printable geopolymer concrete. *Cement and Concrete Composites*, *116*. https://doi.org/10.1016/j.cemconcomp.2020.103899

Panda, B., & Tan, M. J. (2018). Experimental study on mix proportion and fresh properties of fly ash based geopolymer for 3D concrete printing. *Ceramics International*, *44*(9), 10258–10265. https://doi.org/10.1016/j.ceramint.2018.03.031

Panda, B., Unluer, C., & Tan, M. J. (2018). Investigation of the rheology and strength of geopolymer mixtures for extrusion-based 3D printing. *Cement and Concrete Composites*, *94*, 307–314. https://doi.org/10.1016/j.cemconcomp.2018.10.002

Paritala, S., Singaram, K. K., Bathina, I., Khan, M. A., & Jyosyula, S. K. R. (2023). Rheology and pumpability of mix suitable for extrusion-based concrete 3D printing – A review. *Construction and Building Materials*, *402*. https://doi.org/10.1016/j.conbuildmat.2023.132962

Rehman, A. U., & Kim, J. H. (2021). 3D concrete printing: A systematic review of rheology, mix designs, mechanical, microstructural, and durability characteristics. *Materials*, *14*(14). https://doi.org/10.3390/ma14143800

Rehman, A. U., Lee, S.-M., & Kim, J.-H. (2020). Use of municipal solid waste incineration ash in 3D printable concrete. *Process Safety and Environmental Protection*, *142*, 219–228. https://doi.org/10.1016/j.psep.2020.06.018

Roussel, N. (2018). Rheological requirements for printable concretes. *Cement and Concrete Research*, *112*, 76–85. https://doi.org/10.1016/j.cemconres.2018.04.005

Sanjayan, J. G., Nazari, A., & Nematollahi, B. (2019). *3D concrete printing technology: Construction and building applications* (J. G. Sanjayan, A. Nazari, & B. Nematollahi, Eds.). Butterworth-Heinemann, an imptint of Elsevier.

Statistics Canada. (2024). *Table 36-10-0449-01 Gross domestic product (GDP) at basic prices, by industry, quarterly average (x 1,000,000)*.

Tay, Y. W. D., Qian, Y., & Tan, M. J. (2019). Printability region for 3D concrete printing using slump and slump flow test. *Composites. Part B, Engineering*, *174*, 106968–106968. https://doi.org/10.1016/j.compositesb.2019.106968

Wangler, T., Roussel, N., Bos, F. P., Salet, T. A. M., & Flatt, R. J. (2019). Digital Concrete: A Review. *Cement and Concrete Research*, *123*. https://doi.org/10.1016/j.cemconres.2019.105780

Wei, Y., Han, S., Chen, Z., Lu, J., Li, Z., Yu, S., Cheng, W., An, M., & Yan, P. (2024). Numerical simulation of 3D concrete printing derived from printer head and printing process. *Journal of Building Engineering*, *88*. https://doi.org/10.1016/j.jobe.2024.109241

Wu, Y., Liu, C., Liu, H., Zhang, Z., He, C., Liu, S., Zhang, R., Wang, Y., & Bai, G. (2021). Study on the rheology and buildability of 3D printed concrete with recycled coarse aggregates. *Journal of Building Engineering*, *42*, 103030–103030. https://doi.org/10.1016/j.jobe.2021.103030

Zhang, H., Wang, J., Liu, Y., Zhang, X., & Zhao, Z. (2022). Effect of processing parameters on the printing quality of 3D printed composite cement-based materials. *Materials Letters*, *308*, 131271–131271. https://doi.org/10.1016/j.matlet.2021.131271

Zhang, J., Wang, J., Dong, S., Yu, X., & Han, B. (2019). A review of the current progress and application of 3D printed concrete. *Composites Part A: Applied Science and Manufacturing*, *125*. https://doi.org/10.1016/j.compositesa.2019.105533

Zhong, H., & Zhang, M. (2022). 3D printing geopolymers: A review. *Cement and Concrete Composites*, *128*. https://doi.org/10.1016/j.cemconcomp.2022.104455

Chapter 4

4.1 Effect of printing material and design height on printability zone[2]

Abstract

This study investigates the influence of printing materials (i.e., Portland cement (PC) and Alkaline Activated Materials (AAM)) and target design heights (40 mm and 120 mm) on buildability, as well as their corresponding impact on the printability zone. A layer height of 4 mm and a nozzle diameter of 8 mm were selected, as these parameters demonstrated acceptable shape retention with minimal plastic deformation. Fly ash-based alkaline-activated binders were formulated, and their rheological properties (i.e., static yield stress and viscosity) were tailored through a systematic mix design process. This approach aimed to evaluate the effect of material properties, particularly density, on the printability zone when using a Delta printer with a manually fed extruder. The concept of minimum specific yield strength was introduced and determined for all mix proportions. Among the materials assessed, AAM exhibited superior buildability compared to PC due to its lower density and specific yield strength. The results further revealed that an increase in design height leads to a corresponding increase in the minimum required specific yield strength. For a 40 mm design height, the minimum buildable specific yield strength was found to be 830 Pa.cc/g, increasing to 990 Pa.cc/g for a 120 mm design height. However, extrusion failure was observed once the specific yield strength reached the maximum extrudable specific yield strength. Finally, buildability plots were developed for two design heights by correlating specific yield strength and viscosity, in accordance with the established buildability factor criteria.

Keywords:

PC, Alkaline Activated Materials, Printing Material, Specific yield strength, Design height

4.2 Introduction

Portland Cement (PC), the conventional and widely used binder in concrete, accounts for approximately 7 percent of global carbon emissions (Mehta, 2014). Moreover, the traditional concrete methods involving formwork often lead to material waste due to inefficient design (Llatas, 2011). One effective strategy for

[2] Authors: Kamesh Solaiappan and Reza Foruzanmehr

A version of this chapter is submitted to Journal of Composites Part B

lowering the carbon footprint of cementitious materials is replacing conventional materials and methods with alternatives and incorporating digital technologies.

One of the ongoing initiatives to modernize the construction industry focuses on advancing digital manufacturing, with the integration of additive manufacturing identified as a key strategy (Mischke et al., 2024; Wangler et al., 2019). According to ASTM F2792-12, Additive Manufacturing (AM) is defined as "a process of joining materials to make objects from 3D model data, usually layer upon layer, as opposed to subtractive manufacturing methodologies". The extrusion-based 3D printers are the most widely adopted in the AM industry due to their ease of large-scale implementation. This innovation offers notable benefits, including increased design flexibility, reduced labour costs and shorter construction times (Sanjayan et al., 2019). Nevertheless, to fully realize the potential of 3D printing in construction, it is essential to conduct a comprehensive investigation of material properties, with particular emphasis on rheological properties and printability factors for a specific 3D printer (Wangler et al., 2019).

Successful 3D printing depends on factors such as extrudability, shape retention, buildability and the setting time of the mix proportion (Chaiyotha et al., 2023; Chen et al., 2024; Wu et al., 2016). Our previous work identified the printability zone for a manually fed extruder by correlating rheological properties with printability factors. The printability zone of a printer is determined solely by the extrusion system and printing parameters. It was identified by establishing the minimum and maximum rheological limits that allow the 3D printing of a single layer while meeting acceptable printing criteria (Solaiappan & Foruzanmehr, 2025). However, in real-world applications, design requirements are more demanding, and materials must be capable of supporting greater build heights. In such cases, the printability zone is influenced not only by the printer but also by design constraints and material properties.

The layer height equal to the nozzle diameter undergoes excessive plastic deformation due to the increased layer volume and fails to support its weight compared to the halved layer height (David et al., 2023; Solaiappan & Foruzanmehr, 2025; Wei et al., 2024). Although the terms layer height and nozzle standoff distance have been previously explored in the literature, it is crucial to differentiate between them as they refer to different concepts. Layer height (L_h) is the height of individual layers as specified in the slicing software. It is compared to the measured height of each printed layer. Nozzle standoff distance (N_{sd}) is the distance between the nozzle tip and the uppermost printed layer during extrusion. It accounts for both the intended height of the printed layer and any deviations caused by compression of the underlying layers. Defining these parameters is essential for understanding and optimizing the 3D printing process, as they directly influence buildability and print quality.

Buildability refers to a material's ability to sustain the designed height without deformations or collapse in the lowermost layer. Roussel established the yield strength requirement for the lowermost layer as greater than $\rho gH/\sqrt{3}$, where g is the gravitational constant, ρ is the density, and H is the total height of the model (Jayathilakage et al., 2020; Roussel, 2018). The density of the fresh paste is a critical material property influencing buildability, as it is directly related to the weight of the fresh paste. Consequently, the yield stress has to be large enough to support this weight on the lowermost layer. This relationship suggests an interdependence between the yield stress and the density of printing materials. To account for the combined effects of these two properties, this study introduces the concept of specific yield strength, defined as the ratio of static yield stress to the density of the fresh paste.

The density of printing cementitious materials is primarily influenced by the selection of raw materials and the efficiency of particle packing (Relis & Soroka, 1977; Weng et al., 2018). The former includes Portland Cement (PC), Supplementary Cementitious Materials (SCMs), fibres, nano clay, superplasticizers and Viscosity Modifying Agents (VMA) (Kondepudi & Subramaniam, 2021; Sanjayan et al., 2019). Existing literature highlights that the most prevalent strategies for reducing material density involve partially replacing PC with SCMs or using Alkali-Activated Materials (AAMs) and geopolymers formulated with different SCMs as source materials (Rehman & Kim, 2021; Zhong & Zhang, 2022). Furthermore, previous studies have established an inverse relationship between density and buildability, indicating that a reduction in material density leads to improved buildability performance (Rehman & Kim, 2021; Zhang et al., 2021).

This research study explores the use of AAMs and PC to examine the effect of the specific yield strength of printing materials on the buildability and printability zone limits. AAMs offer excellent mechanical properties, high resistance to elevated temperatures and a sustainable alternative to PC (Neupane, 2016; Nodehi & Taghvaee, 2022). This research uses fly ash as the primary source of aluminosilicates and employs Sodium and Calcium hydroxide as alkaline activators to develop AAMs. The study further examines the effect of PC and AAMs with their specific yield strengths for various design heights on the buildability factor. The rheological properties of the mixes are evaluated using the Controlled Shear Stress (CSS) method. A delta 3D printer equipped with extension arms and a manually fed extruder is used to assess the 3D printing behaviour, employing an 8 mm nozzle diameter and a 4 mm layer height.

4.3 Materials

Type 1 PC sourced from Ciment Québec has a specific gravity of 3.2 and a specific surface area (Blaine) of 393 m^2/kg, which complies with the specifications outlined in ASTM standard C150. The mix proportions are adjusted using MasterGlenium 7500 superplasticizer (SP) from Master Builders Solutions. The SP is formulated based on polycarboxylates and conforms to ASTM C494/C 494 M for both Type A

water-reducing admixtures and Type F high-range water-reducing admixtures. The materials used for AAMs in this study include Type F fly ash procured from Shaw Resources, Nova Scotia, Canada and hydrated lime purchased from Univar Solutions, Quebec, Canada. Sodium Hydroxide, with approximately 97 percent, was procured in pellets from VWR chemicals. The chemical composition of PC, fly ash and hydrated lime are tabulated in Table 4-1.

Table 4-1: Chemical composition

	SiO_2	Al_2O_3	Fe_2O_3	CaO	Na_2O	K_2O	MgO	P_2O_5	TiO_2	MnO	LOI
PC	19.10	4.80	3.6	60.2	0.92	-	2.60	-	-	-	1.90
Fly ash	50.063	21.693	15.076	2.887	0.825	1.997	1.45	0.363	0.737	0.083	4.413
Lime	1.456	0.249	0.155	72.8	0.024	0.09	0.714	0.008	0.037	0.007	24.359

4.4 Mix proportions

4.4.1.1 Portland Cement

The mix proportions were selected based on the established printability limits, with yield stress values ranging between 730 Pa to 2210 Pa, and viscosity values between 81070 Pa.s to 110590 Pa.s. Each mix is designated based on a two-part code: the first two digits represent the water-cement ratio, followed by the letters ‘SP’ indicating the presence of SP in the mix, with the last two digits denoting the weight percentage of SP. For instance, a mix proportion with a 0.3 water-to-cement ratio (w/c) and 0.1 percent SP is labelled as “30SP10”. The detailed mix proportioning trials are tabulated in Table **4-2** and a high-performance mixer is used to mix the materials. The mixing procedure adopted to assess rheological and printability factors adheres to the ASTM standard C305-20.

Table 4-2: Mix proportions of cement paste

Mix Proportions	Solids		Liquids		
	Portland Cement	w/c	Water	Wt. Percentage of SP	Weight of Superplasticizer
	(g)	(ratio)	(g)	(%)	(g)
33SP00	1000	0.33	330	0.00%	0.0
34SP00	1000	0.34	340	0.00%	0.0
35SP00	1000	0.35	350	0.00%	0.0
30SP30	1000	0.3	300	0.30%	3.0
30SP40	1000	0.3	300	0.40%	4.0

30SP50	1000	0.3	300	0.50%	5.0
32SP10	1000	0.32	320	0.10%	1.0

4.4.1.2 Alkali-Activated Materials

In this research, the mix design is based on molar ratios of Na_2O/SiO_2 fixed at 0.15, while CaO/SiO_2 is varied at 0.2, 0.4, 0.6, and 0.8. The H_2O/Na_2O ratio is adjusted accordingly for each CaO/SiO_2 variation to ensure rheological properties within printability limits. A 10M sodium hydroxide solution is used consistently throughout the study. The raw materials are weighed and mixed using a high-performance mixer for a total duration of 20 minutes. Fly ash is the only source of silicates in this study; hence, SiO_2/Al_2O_3 is not a factor in mix proportions.

Initially, the dry materials (fly ash and lime) are mixed at a low speed of 95 rpm for 30 seconds. Subsequently, the 10M NaOH solution is gradually introduced, with mixing continuing for 2 minutes while the speed increases from 95 rpm to 180 rpm to prevent material loss from the mixer. Similarly, water is added, and the mixture is blended for an additional 3 minutes, again with the speed gradually increasing from 95 to 180 rpm. Finally, the mix is scraped down and blended at a high speed of 280 rpm for 15 minutes, with the sides of the mixer scraped down every 5 minutes to ensure homogeneity.

The mixes are labelled using a two-part code, where the first two digits represent the CaO/SiO_2, followed by the letters "CS" which stands for Calcium oxide and Silicon dioxide and ending with the liquid-to-solids ratio. For instance, a mix with a molar ratio of 0.4 CaO/SiO_2 and a liquid-to-solids ratio of 0.3, is denoted as 40CS30. All mixing procedures are performed at room temperature (approximately 20°C). The detailed mix trials are presented in Table 4-3.

Table 4-3: Mix proportions of AAM

Mix Proportions	Solids			Liquids	
	Fly ash	Hydrated lime	NaOH Solution	Water	l/s
	(g)	(g)	(g)	(g)	(ratio)
40CS32	1000	218.7	317.5	190.2	0.32
60CS35	1000	349.3	318.7	269.2	0.35
80CS38	1000	481.0	319.9	361.1	0.38

4.5 Experimental setup

4.5.1 Rheological measurements

4.5.1.1 Controlled Shear Stress Method

Rheological measurements were conducted using an Anton Paar MCR 301 rotational rheometer. A four-blade vane spindle was used within a cylindrical cup to assess the static yield stress and viscosity. The vane spindle was chosen over the concentric cylindrical system because the latter is unsuitable for high-solid content mixtures. Measurements were conducted within 10 minutes at a constant temperature of 23 ± 1°C. The CSS method was used, in which shear stress is applied while the corresponding shear rate is recorded. A shear stress ramp of 3.33 pascals per second in the mix, and the corresponding shear rate was recorded. The static yield stress was identified as the shear stress at which the cement paste started to flow, while the viscosity was calculated at the critical strain point of 0.02 s^{-1}.

4.5.2 3D Printer

The Delta WASP 40100 with a manually fed extruder was used in this study. Models were created in SolidWorks and exported as STL files, which were then processed in Simplify3D to generate the necessary G-Code for 3D printing. The manually fed extruder functions through an auger system, allowing material extrusion without external pressure. The printability limits of a given manually fed extrusion printer, defined in the previous study, are tabulated in Table 4-4. These printability limits are determined based on the extrusion system and the 3D printer's ability to print a single layer.

Table 4-4: Printability limits and their corresponding criteria

Printability Limits	Definition
Maximum printable viscosity	The maximum viscosity that the printer can extrude without facing any interruptions or clogging, or significant variations in S_{lf}. This is determined as the median between the minimum value of non-extrudable viscosities (or viscosity exhibits S_{lf} less than 0.99) and the maximum value of extrudable viscosity with S_{lf} greater than 0.99.
Minimum printable viscosity	The minimum viscosity required for the cementitious material to maintain its acceptable shape retention factor. This is identified as the median between the minimum value of the viscosities exhibiting a S_f less than 1.2 and the maximum value of viscosities displaying a S_f that exceeds 1.2.

Minimum printable yield stress	The minimum yield stress required to print at least one layer with minimal dimensional variation in height. This is determined as the median between the minimum value of the yield stress exhibiting an S_{lf} greater than 0.99 and the maximum value of yield stress displaying an S_{lf} below 0.99.
Maximum printable yield stress	The maximum yield stress that the printer can extrude without facing any interruptions or clogging throughout the printing process. This is determined as the midpoint between the minimum value of non-extrudable yield stress and the maximum value of buildable yield stress.

4.5.3 Calculation of minimum specific buildable yield strength

The buildability limit for each design height is referred to as the minimum specific buildable yield strength, which is the lowest specific yield strength required to achieve the design height with a buildability factor, B_f, *(Equation 3)* of more than 0.99 and a minimal change in the width of the lowermost layer, $C_{lw} < 1.3$, *(Equation 4)*.

$$\text{Buildability factor } (B_f) = \frac{M_{ah}}{D_h} \qquad \textit{(Equation 3)}$$

$$\text{Change in lowermost layer width } (C_{lw}) = \frac{\text{Lowermost layer width } (W_{ll})}{\text{Layer width}(L_w)} \qquad \textit{(Equation 4)}$$

The process of determining B_f for each design height consists of three key steps: first, measuring the maximum printed height (M_{ph}), second, calculating the maximum achievable height (M_{ah}) with $C_{lw} < 1.3$ and third, determining the buildability factor (B_f) corresponding to each design height for a given mix.

The M_{ph} is the maximum height that the paste can print, exhibiting structural stability (i.e., without collapsing or showing visible deformations). The M_{ah} is the maximum height that can be printed while maintaining an acceptable C_{lw} below 1.3 (i.e., with a maximum 30 percent plastic deformation). It is important to note that this C_{lw} criterion can be made more stringent in cases where printing precision considerations are required. A schematic representation of C_{lw} is shown in Figure 4-1.

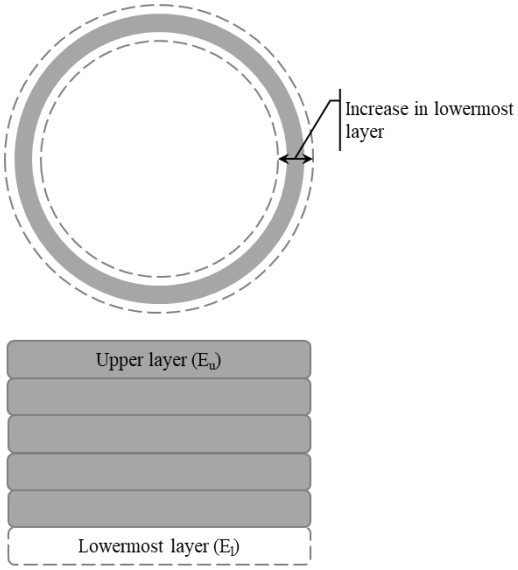

Figure 4-1: Schematic representation of C_{lw}

The M_{ah} is governed by two key factors: the setting time of paste (i.e., the printing duration must be shorter than the setting time) and the change in the dimensions of the lowermost layer. This study is conducted entirely within the fresh state, and the first factor is not considered. A correlation between the C_{lw} and printed height was established for all mix proportions. Subsequently, M_{ah} was determined through a linear interpolation, using the C_{lw} of a single layer and the C_{lw} at M_{ph}, to calculate the M_{ah} at C_{lw} equals 1.3 for a given paste. A sample linear interpolation graph for the mix 32SP10 is shown in Figure 4-2.

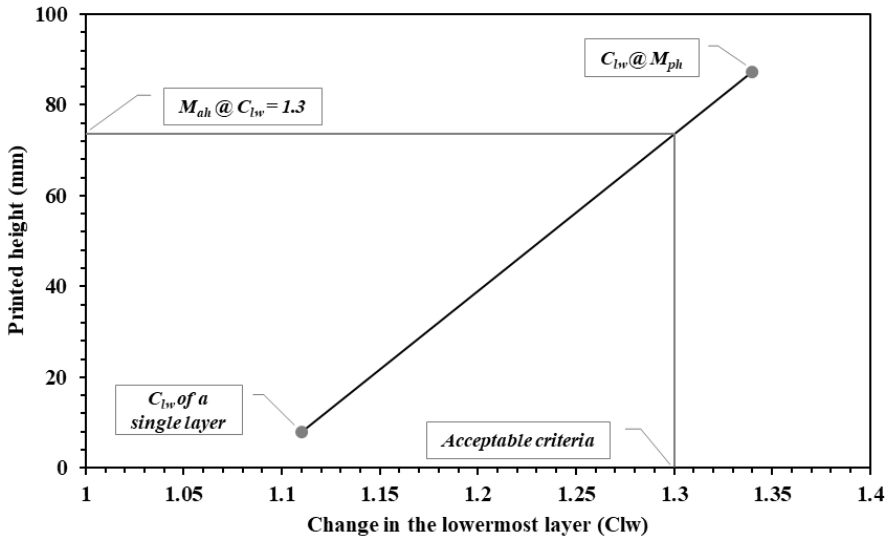

Figure 4-2: Sample linear interpolation graph – 32SP10

Buildability is evaluated using the B_f, defined as the ratio of the maximum achievable height (M_{ah}) to the design height (D_h), which must remain above 0.99 for a mix to be considered buildable. The B_f is influenced

by material properties, particularly specific yield strength, which accounts for both density and the static yield stress. To assess buildability, hollow cylinders with a 100 mm diameter were printed for all selected mix proportions. Based on prior findings, an 8 mm nozzle diameter with a 4 mm layer height was used, as it provided an acceptable shape retention factor (S_f) while minimizing plastic deformation. Printing was halted if the mixes deviated from the intended path or exhibited noticeable deformations or collapse. B_f and C_{lw} were obtained and reported after curing.

For this study, the maximum printed height (M_{ph}) was set at 140 mm, and the effects of design heights of 40 mm and 120 mm were evaluated. These design heights were chosen to ensure that the entire model could be printed while the material remained in the fresh state, with the total printing duration limited to under 30 minutes to prevent partial extrusion failures. The minimum specific buildable yield strength is calculated as the midpoint between the maximum specific yield strength at which B_f falls below 0.99 and the minimum specific yield strength that results in a B_f greater than 0.99.

4.6 Results and Discussion

4.6.1 Rheological behaviour

A previous study in our research revealed the printability zone for a manually fed extruder through 3D printing of a single layer using an 8 mm nozzle diameter with layer heights of 4 mm and 8 mm with PC as a reference material. As expected for AAMs, the effect of CaO/SiO_2 significantly impacted the rheological properties. The addition of hydrated lime in the AAMs demonstrated a direct proportionality to rheological properties, attributed to the increased volume of solids fraction at a constant liquids-to-solids ratio. Using an empirical approach, the optimized liquids-to-solids ratio was selected for each CaO/SiO_2, excluding 0.2. The resultant mix proportions are presented in Figure 4-3 where dark gray represents AAMs and light gray represents PC. The results are tabulated in Table **4-5** represent the arithmetic mean of three tested samples for each mix proportion and the printability limits for the manual feeding extruder with an 8 mm nozzle diameter and 4 mm layer height.

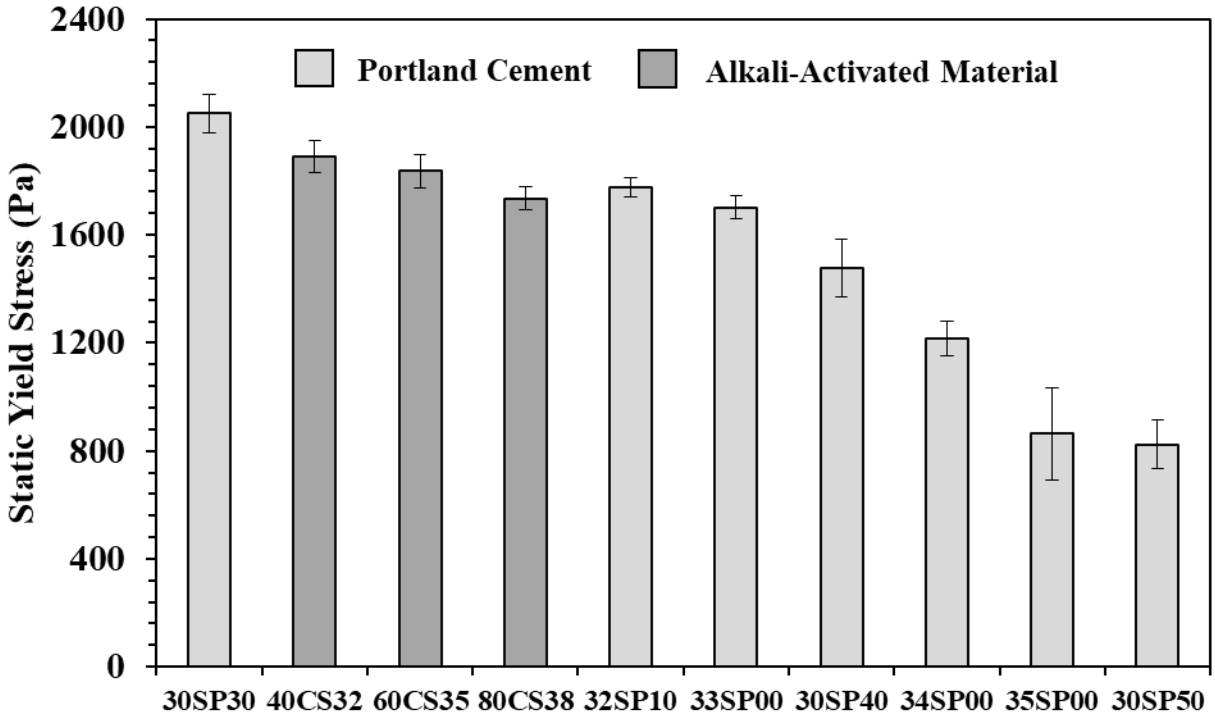

Figure 4-3: Rheological properties for the optimized mix proportions

Table 4-5: Printability limits and measured rheological properties

Mix Proportions	Static yield stress (Pa)	Minimum printable yield stress (For the printer)	Maximum printable yield stress (For the printer)
30SP30	2050.7 ± 71.80	740 Pa	2185 Pa
40CS32	1889.4 ± 60.30		
60CS35	1835.8 ± 61.41		
32SP10	1776.2 ± 34.81		
80CS38	1735.3 ± 41.84		
33SP00	1701.3 ± 42.00		
30SP40	1477.9 ± 105.37		
34SP00	1216.5 ± 63.66		
35SP00	864.30 ± 170.44		
30SP50	823.90 ± 91.88		

4.6.2 Effect of Material

Buildability is the only printability factor influenced by both material properties and design requirements. Previous research primarily focused on static yield stress limits for a single layer, which depend solely on the printer and extrusion system. However, in terms of buildability, density plays a crucial role, as the accumulated weight of the printed layers affects the model's stability. Therefore, characterizing the printability zone based on static yield stress limits is insufficient for assessing buildability. Instead, specific yield strength (i.e., the ratio of static yield stress to the density of the fresh paste) emerges as a key parameter for evaluating buildability. While static yield stress is governed by the volume fraction of solids and liquids, density is determined by the material composition.

This study compares PC and AAMs, focusing on how density and specific yield strength impact printability. AAMs exhibited superior buildability compared to PC, despite having similar rheological properties. For example, mix 80CS38 (AAM) and 32SP10 (PC) had comparable static yield stresses of 1735.3 Pa and 1776.1 Pa, respectively. However, their printability varied significantly, with PC printing a maximum of 22 layers, reaching only 87 mm, while AAM achieved 35 layers, reaching the M_{ph} of 140 mm under the same configuration. This difference is attributed to density variations, as PC had a higher density of 1.87 g/cc, increasing the weight per layer and leading to plastic deformation in the lower layers. By reducing the overall density by 0.2 g/cc, the AAM mixes significantly improved buildability, highlighting the critical role of density in the 3D printing performance of vertically extended builds. Consequently, AAMs exhibited a higher specific yield strength (1039 Pa.cc/g) compared to PC (950 Pa.cc/g), reinforcing its superior buildability. The static yield stress, density and specific yield strength values for all mixes are tabulated in Table **4-6**.

The minimum number of layers that AAM (40CS32) can print for the M_{ph} equals 140mm is 35, while the maximum number of layers PC (32SP10) can print is 22, labelled as 'B' and 'C' in Figure **4-4**. This highlights the importance of specific yield strength and its significant role in determining buildability.

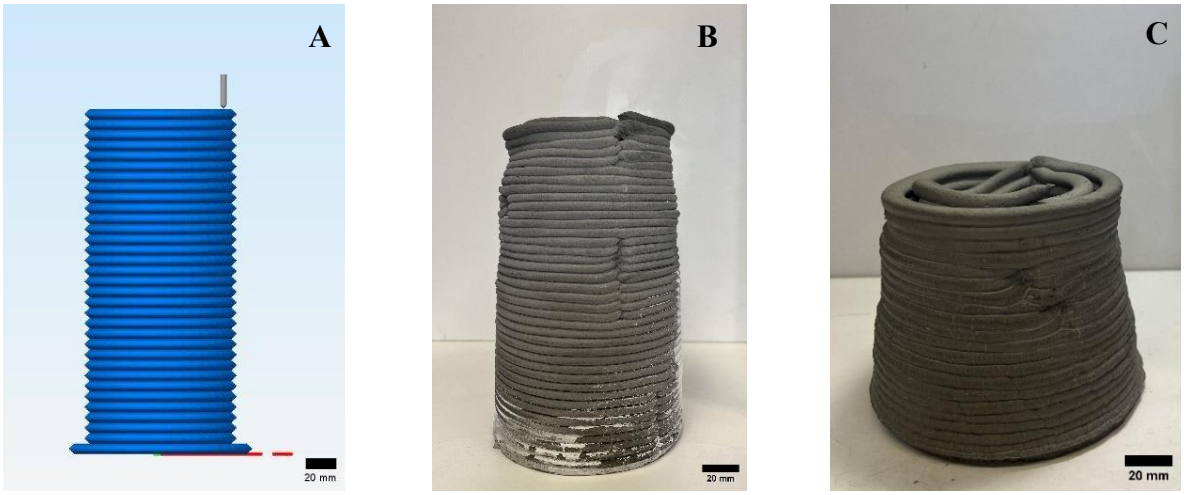

Figure 4-4: Effect of Material in buildability (A – Designed model, B – AAM, C- PC)

Table 4-6: Density data measurements and specific yield strength

Mix Proportions	Static yield stress (Pa)	Density (g/cc)	Specific yield strength (Pa.cc/g)
30SP30	2050.7 ± 71.80	1.93 ± 0.09	1063.12
40CS32	1889.4 ± 60.30	1.68 ± 0.04	1124.43
60CS35	1835.8 ± 61.41	1.70 ± 0.06	1079.95
32SP10	1776.2 ± 34.81	1.87 ± 0.08	950.77
80CS38	1735.3 ± 41.84	1.67 ± 0.09	1040.77
33SP00	1701.3 ± 42.00	1.87 ± 0.08	910.50
30SP40	1477.9 ± 105.37	1.93 ± 0.15	766.16
34SP00	1216.5 ± 63.66	1.86 ± 0.09	653.90

4.6.3 Effect of design height

The design height (D_h) refers to the required model height for a specific application. For successful 3D printing, the material must exhibit key properties such as high static yield stress and low density or in other words, high specific yield strength. A mix capable of printing 120 mm can also print 40 mm, but the reverse is not always feasible. It is important to note that the design height is a variable parameter that can be adjusted based on specific design requirements. In our previous study, nozzle diameter and layer height were identified as key factors influencing printability limits of a manually fed extrusion printer, whereas in this study, the design height plays a critical role in determining the buildability factor and buildable yield stress to 3D print a given object.

4.6.3.1 40 mm design height

The 40 mm design height is suitable for 3D printing panel applications with varying infill densities. Initially, the maximum printed height (M_{ph}) and change in the lowermost layer (C_{lw}) were measured and recorded. C_{lw} exhibited an inverse relationship with specific yield strength (i.e., higher specific yield strength resulted in lower C_{lw}) as the lowermost layer had sufficient strength to support the weight of the uppermost printed layers. The linear interpolation method was performed for all mixes to determine the maximum achievable height (M_{ah}). When C_{lw} remains lower than 1.3 for the maximum printed height, and in such cases, the maximum achievable height is linearly extrapolated, and the results are calculated. The results showed that AAMs successfully printed for 40 mm, while for PC, only a few mixes achieved this height. The data measurements and M_{ah} are presented in Table **4-7**. Regardless of the material, mixes with a specific yield strength exceeding 830 Pa.cc/g were able to achieve 40 mm. The materials had an adequate specific yield strength and a balanced density, ensuring successful printing. This confirms that higher specific yield strength correlates with a higher buildability factor. It is worth noting that the entire printing duration remains in its fresh state.

Table 4-7: Data measurements and determination of M_{ah}

Mix Proportions	Specific yield strength (Pa.cc/g)	M_{ph} (mm)	C_{lw} for a single layer	C_{lw} at M_{ph}	M_{ah} (at C_{lw} = 1.3) (mm)
30SP30	1063.12	40.5	1.06	1.13	119.43
40CS32	1124.43	140.7	1.07	1.20	242.78
60CS35	1079.95	139.9	1.08	1.12	733.45
80CS38	950.77	140.4	1.05	1.10	670.00
32SP10	1040.77	87.2	1.11	1.34	73.43
33SP00	910.50	83.0	1.16	1.46	43.00
30SP40	766.16	62.5	1.27	1.54	14.06
34SP00	653.90	62.4	1.29	1.55	10.09

The buildability factor was calculated, revealing that materials exhibiting a specific yield strength exceeding 830 Pa.cc/g could achieve a Bf of more than 0.99 for a design height of 40 mm. The minimum buildable specific yield strength was determined as the median point between the yield stress values of mix 33SP00 and mix 30SP40, resulting in a calculated and rounded-off value of 830 Pa.cc/g. It is important to emphasize that extrudability is the inherent characteristic of the extrusion system and is independent of both the design height and the material's density. However, to maintain consistency in the analysis, the maximum extrudable yield stress is expressed in terms of maximum extrudable specific yield strength. In

our previous study, mix 32SP00 was classified as a non-extrudable mix proportion, and the maximum extrudable specific yield strength was determined as the median value between mix 32SP00 and 40CS32, calculated and rounded off to 1140 Pa.cc/g. The buildable zone plot for a 40 mm design height is illustrated in Figure 4-5, while the correlation between minimum buildable specific yield strength values and buildability factor is summarized in Table 4-8.

Table 4-8: Correlation of minimum yield stress for 40 mm D_h

Mix Proportions	Specific yield strength (Pa.cc/g)	Tolerance Criteria (B_f > 0.99)	Buildability (40 mm)
30SP30	1063.12	2.99 > 0.99	Acceptable
40CS32	1124.43	6.07 > 0.99	Acceptable
60CS35	1079.95	18.34 > 0.99	Acceptable
80CS38	950.77	16.75 > 0.99	Acceptable
32SP10	1040.77	1.84 > 0.99	Acceptable
33SP00	910.50	1.08 > 0.99	Acceptable
30SP40	766.16	0.35 < 0.99	Unacceptable
34SP00	653.90	0.25 < 0.99	Unacceptable

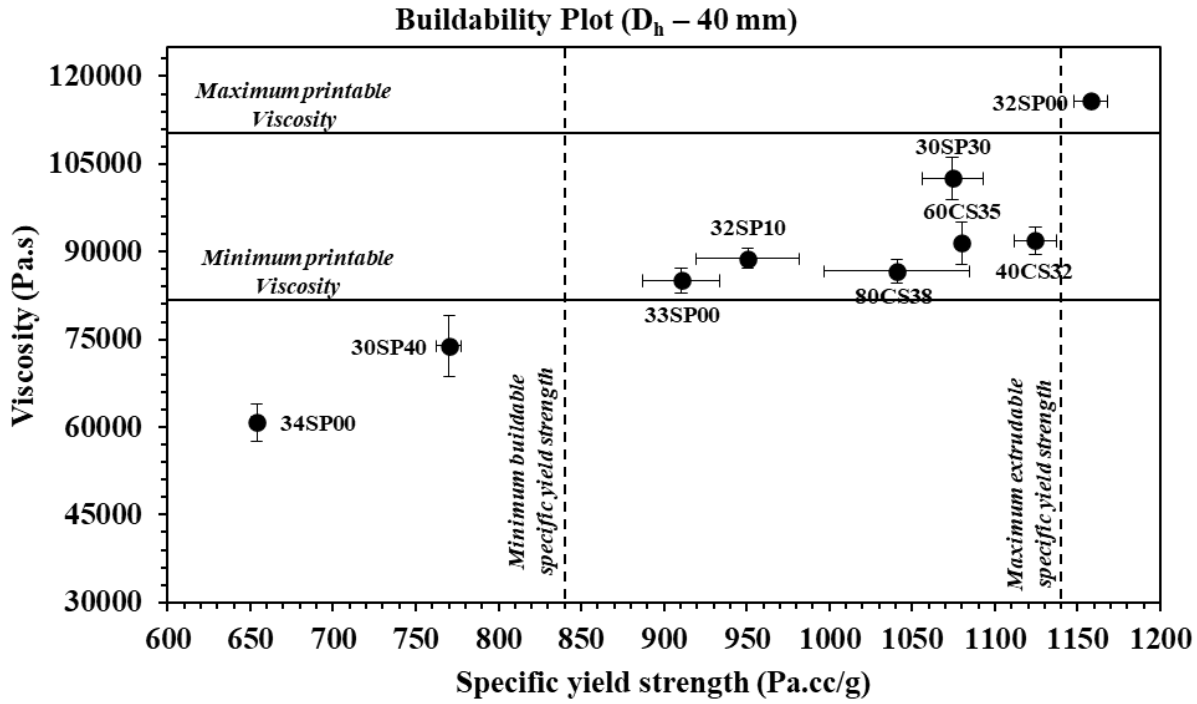

Figure 4-5: Buildability plot zone for design height of 40 mm

4.6.3.2 120 mm design height

The 120 mm design height is suitable for 3D printing applications such as aesthetic models or panels. Similar to the 40 mm design height, the data were measured, and the maximum achievable height was calculated. Among the printed materials, all AAM-based mixes, namely 40CS32, 60CS35, and 80CS38, successfully achieved 120 mm, whereas only the 30SP30 mix among PC-based formulations exceeded this height. An interesting inverse relationship was observed between the CaO/SiO_2 molar ratio and the change in the lowermost layer width. AAM mixes were chosen to exceed the minimum printable viscosity, and each exhibited a C_{lw} less than 1.3. This behaviour is attributed to the formation of C-A-S-H gels at higher molar ratios, such as 0.8 CaO/SiO_2 combined with low density among all materials, which resulted in an exceptional property for successful 3D printing labelled as "D" as shown in Figure 4-6.

The minimum specific yield strength required to print a 120 mm design height must be above 990 Pa.cc/g, whereas for 40 mm, it must be above 830 Pa.cc/g. This demonstrates that higher design heights require higher specific yield strength, but this does not necessarily apply to static yield stress. For instance, mix 32SP10 had a higher yield stress than 80CS38, yet it failed to achieve 120 mm due to the high density. This confirms that the buildability criteria are not solely based on minimum buildable yield stress but also on minimum specific yield strength. It is important to ensure that the specific yield strength remains within the maximum specific extrudable yield strength throughout the entire printing duration, as exceeding this limit can lead to extrusion failure. This can be addressed by introducing a pressurized extruder to extrude the mixes, and the buildability factor shall be calculated. The minimum buildable specific yield strength was determined as the median point between the yield stress values of mix 32SP10 and mix 80CS32, resulting in a calculated and rounded-off value of 990 Pa.cc/g. As previously noted, extrudability is governed solely by the 3D printer and is not influenced by the design geometry or the density of printing materials. The maximum specific yield strength for a 120 mm design height is the same as a 40 mm design height. The buildability plot for the 120 mm design height is shown in Figure **4-7** and the correlation between the buildability factor and the material properties is tabulated in Table **4-9**.

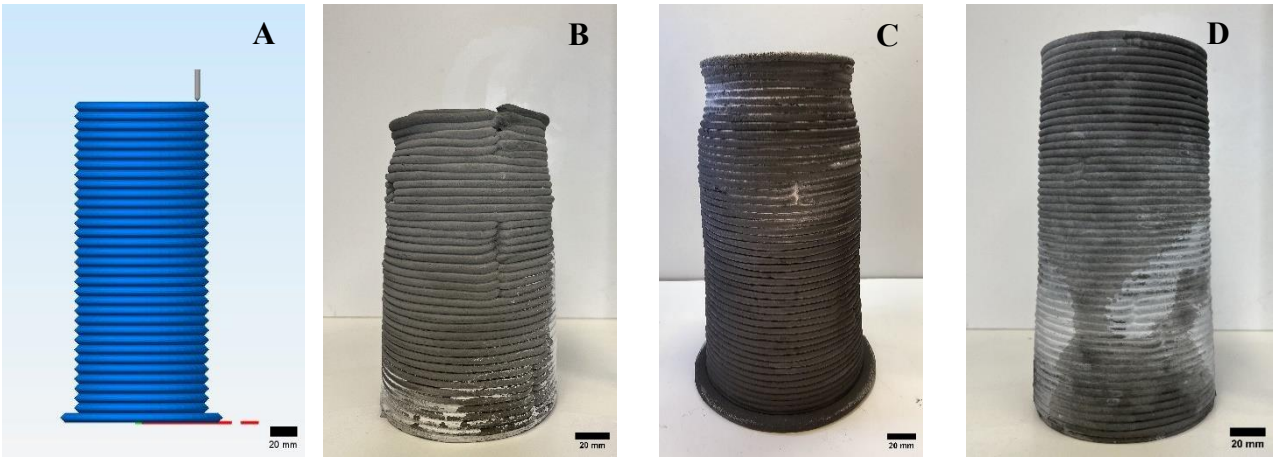

Figure 4-6: Buildability behaviour – AAM (A – Designed model, B – 40CS32, C – 60CS35, D – 80CS38)

Table 4-9: Correlation of minimum yield stress for 120 mm D_h

Mix Proportions	Specific yield strength (Pa.cc/g)	Tolerance Criteria (B_f > 0.99)	Buildability (120 mm)
30SP30	1063.12	1.00 > 0.99	Acceptable
40CS32	1124.43	2.02 > 0.99	Acceptable
60CS35	1079.95	6.11 > 0.99	Acceptable
80CS38	950.77	5.58 > 0.99	Acceptable
32SP10	1040.77	0.61 < 0.99	Unacceptable
33SP00	910.50	0.36 < 0.99	Unacceptable
30SP40	766.16	0.12 < 0.99	Unacceptable
34SP00	653.90	0.08 < 0.99	Unacceptable

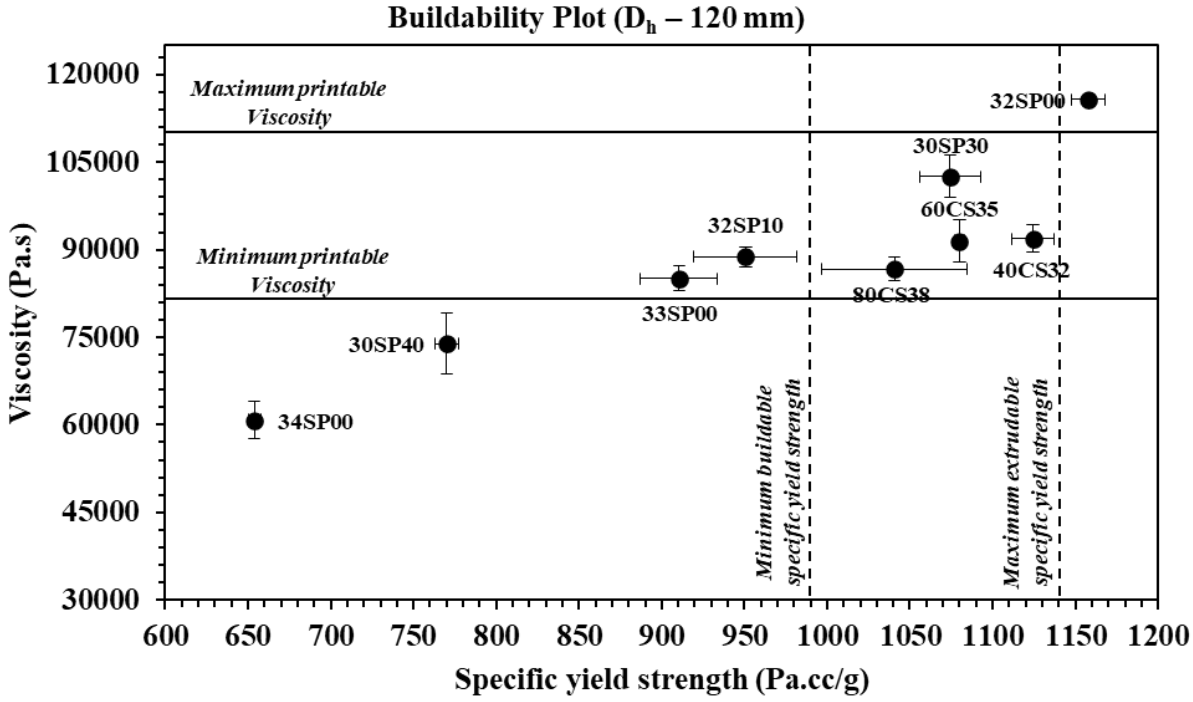

Figure 4-7: Buildability plot zone for design height of 120 mm

4.7 Conclusion and future works

This study demonstrates the influence of specific yield strength and design height on buildability. For each design height, the minimum buildable yield stress shifted accordingly, highlighting the critical relationship between material properties and printability limits. Optimizing material properties is essential for achieving high-quality 3D printing at a given design height. The findings indicate that a minimum specific yield strength of 830 Pa.cc/g is required for a 40 mm design height, which increases to 990 Pa.cc/g for successfully printing a 120 mm design height. For both the design heights, the maximum extrudable specific yield strength was determined as 1140 Pa.cc/g. The same methodology can be developed for different Supplementary Cementitious Materials (SCMs) to expand the data set and improve the understanding of material performance. Additionally, the incorporation of chemical admixtures, such as retarders or superplasticizers, can be explored in future studies to extend the printing duration for higher design heights of more than 120 mm.

The influence of the CaO/SiO_2 molar ratio on rheological properties aligns with research exploring the percentage replacement of calcium hydroxide with fly ash, indicating that molar ratio-based mix proportioning is an effective method for Alkali-Activated Materials (AAMs) and geopolymers. Future studies can apply this methodology to a variety of cementitious materials to evaluate their printability.

However, it is essential to emphasize that the first step in identifying the printability zone involves establishing the correlation between viscosity and yield stress for a specific printer. This may demand developing a tailored range of cementitious mixtures suited to the rheological requirements of the printer. Once the printability zone is defined for the extrusion system, the minimum specific buildable yield stress can then be fine-tuned based on the design height.

4.8 References

Chaiyotha, D., Kantawong, W., Payakaniti, P., Pinitsoontorn, S., & Chindaprasirt, P. (2023). Finding optimized conditions for 3D printed high calcium fly ash based alkali-activated mortar. *Case Studies in Construction Materials*, *18*, e01976–e01976. https://doi.org/10.1016/j.cscm.2023.e01976

Chen, Y., Rahmani, H., Schlangen, E., & Çopuroğlu, O. (2024). An approach to develop set-on-demand 3D printable limestone-calcined clay-based cementitious materials using calcium nitrate. *Cement & Concrete Composites*, *145*, 105373–105373. https://doi.org/10.1016/j.cemconcomp.2023.105373

David, M., Freund, N., Dröder, K., & Lowke, D. (2023). The effects of nozzle diameter and length on the resulting strand properties for shotcrete 3D printing. *Materials and Structures*, *56*(8). https://doi.org/10.1617/s11527-023-02246-1

Jayathilakage, R., Rajeev, P., & Sanjayan, J. G. (2020). Yield stress criteria to assess the buildability of 3D concrete printing. *Construction & Building Materials*, *240*, 117989–117989. https://doi.org/10.1016/j.conbuildmat.2019.117989

Kondepudi, K., & Subramaniam, K. V. L. (2021). Formulation of alkali-activated fly ash-slag binders for 3D concrete printing. *Cement and Concrete Composites*, *119*. https://doi.org/10.1016/j.cemconcomp.2021.103983

Llatas, C. (2011). A model for quantifying construction waste in projects according to the European waste list. *Waste Management*, *31*(6), 1261–1276. https://doi.org/10.1016/j.wasman.2011.01.023

Mehta, P. K. (Povindar K.). (2014). *Concrete microstructure, properties, and materials* (P. J. M. Monteiro, Ed.; 4th ed.). McGraw-Hill.

Mischke, J., Stokvis, K., Vermeltfoort, K., & Biemans, B. (2024). *Delivering on construction productivity is no longer optional Why the construction industry must climb out of its productivity rut-and why it hasn't yet*. https://www.mckinsey.com/capabilities/operations/our-insights/delivering-on-construction-productivity-is-no-longer-optional

Neupane, K. (2016). Fly ash and GGBFS based powder-activated geopolymer binders: A viable sustainable alternative of portland cement in concrete industry. *Mechanics of Materials*, *103*, 110–122. https://doi.org/10.1016/j.mechmat.2016.09.012

Nodehi, M., & Taghvaee, V. M. (2022). Alkali-Activated Materials and Geopolymer: A Review of Common Precursors and Activators Addressing Circular Economy. *Circular Economy and Sustainability (Online)*, *2*(1), 165–196. https://doi.org/10.1007/s43615-021-00029-w

Rehman, A. U., & Kim, J. H. (2021). 3D concrete printing: A systematic review of rheology, mix designs, mechanical, microstructural, and durability characteristics. *Materials*, *14*(14). https://doi.org/10.3390/ma14143800

Relis, M., & Soroka, I. (1977). Variation in density of portland cement hydration products. *Cement and Concrete Research*, *7*(6), 673–680. https://doi.org/10.1016/0008-8846(77)90050-3

Roussel, N. (2018). Rheological requirements for printable concretes. *Cement and Concrete Research*, *112*, 76–85. https://doi.org/10.1016/j.cemconres.2018.04.005

Sanjayan, J. G., Nazari, A., & Nematollahi, B. (2019). *3D concrete printing technology: Construction and building applications* (J. G. Sanjayan, A. Nazari, & B. Nematollahi, Eds.). Butterworth-Heinemann, an imptint of Elsevier.

Solaiappan, K., & Foruzanmehr, R. (2025). *A Rheological test method for determining the printability zone of cementitious 3D printers* [Manuscript Under Review].

Wangler, T., Roussel, N., Bos, F. P., Salet, T. A. M., & Flatt, R. J. (2019). Digital Concrete: A Review. *Cement and Concrete Research*, *123*. https://doi.org/10.1016/j.cemconres.2019.105780

Wei, Y., Han, S., Chen, Z., Lu, J., Li, Z., Yu, S., Cheng, W., An, M., & Yan, P. (2024). Numerical simulation of 3D concrete printing derived from printer head and printing process. *Journal of Building Engineering*, *88*. https://doi.org/10.1016/j.jobe.2024.109241

Weng, Y., Li, M., Tan, M. J., & Qian, S. (2018). Design 3D printing cementitious materials via Fuller Thompson theory and Marson-Percy model. *Construction & Building Materials*, *163*, 600–610. https://doi.org/10.1016/j.conbuildmat.2017.12.112

Wu, P., Wang, J., & Wang, X. (2016). A critical review of the use of 3-D printing in the construction industry. *Automation in Construction*, *68*, 21–31. https://doi.org/10.1016/j.autcon.2016.04.005

Zhang, C., Nerella, V. N., Krishna, A., Wang, S., Zhang, Y., Mechtcherine, V., & Banthia, N. (2021). Mix design concepts for 3D printable concrete: A review. *Cement and Concrete Composites*, *122*. https://doi.org/10.1016/j.cemconcomp.2021.104155

Zhong, H., & Zhang, M. (2022). 3D printing geopolymers: A review. *Cement and Concrete Composites*, *128*. https://doi.org/10.1016/j.cemconcomp.2022.104455

Chapter 5

5.1 Conclusions and Future Works

5.2 Conclusions

This study established a standardized methodology for determining the printability zone of a 3D printer and for constructing objects at specified design heights. The printability zone was defined as the optimal range of rheological properties within which a printing material was extruded and deposited as a single layer and retained structural integrity within acceptable tolerances. Foundational printability limits were determined, including the maximum and minimum printable yield stresses. The maximum printable viscosity is the viscosity that the printer can extrude without facing any interruptions or significant variations in S_{lf}. The minimum printable viscosity is the viscosity which the printing material can maintain its acceptable shape retention factor ($S_f < 1.2$). The minimum printable yield stress is the stress that the printer can print at least one layer with minimal dimensional variations in height ($S_{lf} > 0.99$). The maximum printable yield stress is the stress that the printer can extrude without facing any clogging throughout the printing process.

For an 8 mm layer height using the delta WASP 40100 printer, the yield stress limits ranged from 1040 Pa to 2185 Pa, and the viscosity ranged from 80000 Pa.s to 96000 Pa.s. For a 4 mm layer height, the yield stress limits range from 740 Pa to 2185 Pa, with the viscosity values ranging from 80000 Pa.s to 110000 Pa.s. The printability zone of an object can be characterized by two key parameters: specific yield strength and viscosity. The results indicated that a minimum specific yield strength of 830 Pa.cc/g was required to achieve a 40 mm design height, which increased to 990 Pa.cc/g for a design height of 120 mm. These findings demonstrated that higher design heights required proportionally higher specific yield strengths, underscoring the importance of incorporating density into buildability assessments.

The printability zone of a printer was evaluated in terms of specific yield strength, rather than relying solely on static yield stress. However, for single-layer deposition, the material's density played a negligible role, as there was no additional weight on the layer. In such cases, printability was assessed using either static yield stress or specific yield strength, given their direct proportionality. This methodology was based on quantitative assessments of rheological properties and printability factors.

The single-layer buildability factor, shape retention factor, and buildability factor were defined as the ratios of printed measurements to corresponding design parameters. Consequently, this methodology was adaptable to various design specifications, allowing for adjustments based on specific requirements and

printer capabilities. The rheological measurements observed in this study followed a linear correlation between static yield stress and viscosity.

This study opened doors for the development of 3D printers for various types of cementitious materials as well as ceramic slurries. It also paved the way for researchers and industries focused on developing printing materials, such as concrete, for 3D printing applications. Additionally, this methodology now forms the basis for an ASTM test method for 3D printers equipped with non-pressurized extruders. Reference mix proportions using Portland cement (PC), with known yield stress and viscosities, were developed to establish baseline parameters. Researchers could use these mixes to print a single layer, thereby determining the printability limits and zones for a given printer. By printing to specific design heights, the corresponding buildability factors could be identified for the printing material. The findings demonstrated the reliability of using quantitative rheological measurements to determine the printability zone for both the 3D printer and the intended design object

5.3 Future Works

This methodology enables the characterization of large-scale printers, including pressurized extruders, which require a continuous paste with much higher viscosity and yield stress. One challenge we will address is segregation, which arises when working with very low water-to-cement (w/c) ratios. To mitigate this, we plan to incorporate water reducers and sustainable superabsorbents developed by our group members.

In the case of pressurized extruders, additional factors such as extrusion pressure and segregation must be considered. Excessive pressure can cause the separation of liquids and solids within the hopper, which can be managed through the use of chemical admixtures like superplasticizers and retarders. Furthermore, printability limits and zones vary with different extrusion pressures. Higher extrusion pressure can facilitate the extrusion of materials with higher viscosities, while lower pressure may struggle to extrude materials with the same viscosity.

As part of future work, this research will employ fly ash-based AAMs to explore the impact of key factors such as the CaO/SiO_2 ratio on printability. The data set will be expanded by incorporating SCMs such as metakaolin. This material will introduce a broader range of chemical compositions and specific yield strengths, enhancing the accuracy and applicability of the printability zone for various object designs. Based on the rheological findings obtained for the specific printer used in this study, this methodology will provide a framework to explore diverse mix proportions using alternative materials.

Appendices

Appendix A: Mix proportioning based on Molar Ratios

The fresh and hardened state properties of Alkali-Activated Materials (AAM) are primarily influenced by the type, chemical composition of the aluminosilicates, and reagents that are used in the formulation (Singh et al., 2015). In this study, fly ash is utilized as the primary pozzolanic material due to its higher specific surface area, which enhances the kinetics of reactions. Its use also opens the possibility of incorporating alternative ash-based wastes, such as wood ash or ash obtained from municipal incineration plants.

The chemical composition of fly ash can vary significantly. According to ASTM C618, fly ash is categorized into Class F, C, and N, based on the combined content of silicon dioxide, aluminum dioxide, and iron oxide (F, N ≥ 70 %, 70 % > C ≥ 50 %). These compositions depend largely on geographical location and the type of coal used in thermal power plants (Low et al., 2021).

Sodium hydroxide (NaOH) is employed as the primary activating reagent in this study. However, its use is associated with high costs and sustainability concerns (Garcia-Lodeiro et al., 2015). To address this, the dosage of Sodium Hydroxide is kept minimal. While reducing NaOH content may lower the overall alkalinity, potentially compromise the fresh and mechanical properties. A viable strategy is to supplement the mix with more sustainable alternatives, such as Calcium Hydroxide. It is locally available and contributes hydroxide ions (OH^-) in $Ca(OH)_2$, thereby increasing alkalinity and calcium content, which in turn enhances mechanical properties (Hoyos-Montilla et al., 2023).

According to the literature, mix proportioning of geopolymer and alkali-activated materials is typically guided by factorial design and target strength method (Li et al., 2019; Ohno & Li, 2018). For instance, Barbosa *et al.* formulated the geopolymer mixes based on molar oxide ratios and achieved compressive strength of up to 49 MPa in 3 days. The most studied molar ratios in the literature include SiO_2/Al_2O_3, Na_2O/SiO_2, and H_2O/Na_2O. Among these, the SiO_2/Al_2O_3 significantly affects both the setting time and compressive strength; lower values are generally associated with higher compressive strength and faster setting time (De Silva et al., 2013).

In this study, fly ash is used as the sole source of aluminosilicates, limiting direct control over the SiO_2/Al_2O_3 ratio in the mix design. Therefore, the Na_2O/SiO_2 molar ratio becomes a more critical parameter, as it determines the level of alkalinity necessary for effective geopolymerization or alkalinization. Prior studies suggest that optimal Na_2O/SiO_2 is approximately 0.5 (Bocullo et al., 2021), which is consistent with the range of 0.2 to 0.48 reported by Barbosa *et al.* (Barbosa et al., 2000). In this research study, Calcium

Hydroxide is introduced alongside a reduced amount of Sodium Hydroxide to enhance sustainability through the use of locally available materials, resulting in a Na_2O/SiO_2 ratio of 0.15.

Determining the appropriate proportion of Calcium Hydroxide is essential to ensure the mixture satisfies both fresh and hardened state properties, and as a result, the CaO/SiO_2 molar ratio is introduced. Hoyos-Montilla *et al.,* demonstrated that substituting 20 percent of low calcium fly ash with calcium hydroxide increased compressive strength from 4.5 MPa to 25.65 MPa. The literature suggests that the CaO/SiO_2 ratio is most effective in the range of 0.2 to 1.2 (Hoyos-Montilla et al., 2023). T. Mabah *et al.* found that a CaO/SiO_2 of 0.4 yielded the highest compressive strength in their study, where calcium oxide was derived from chicken eggshells (T.Mabah et al., 2019).

However, previous research primarily focused on the CaO/SiO_2 in isolation, without considering its interaction with the H_2O/Na_2O. This is a critical gap, as increasing the CaO/SiO_2 ratio typically requires a higher water-to-binder ratio to maintain desirable fresh state properties (Cheah et al., 2017). Based on insights from the literature, the mix proportions in this study are governed by three key molar ratios: Na_2O/SiO_2, CaO/SiO_2, and H_2O/Na_2O. This research specifically investigates the influence of the CaO/SiO_2 in the range of 0.2 to 0.8, along with the corresponding H_2O/Na_2O ratio, in the context of rheological properties and 3D printing applications. Additionally, the chemical compositions of the fly ash and hydrated lime are characterized by X-Ray Fluorescence (XRF), are tabulated in Table 0-1 and the mix proportions are tabulated in Table 0-2.

Table 0-1: Chemical composition

	SiO_2	Al_2O_3	Fe_2O_3	CaO	Na_2O	K_2O	MgO	P_2O_5	TiO_2	MnO	LOI
Fly ash	50.063	21.693	15.076	2.887	0.825	1.997	1.45	0.363	0.737	0.083	4.413
Lime	1.456	0.249	0.155	72.8	0.024	0.09	0.714	0.008	0.037	0.007	24.359

Table 0-2: Mix Proportions

Molar Ratio	Mix 1	Mix 2	Mix 3	Mix 4
Na_2O/SiO_2	0.15	0.15	0.15	0.15
CaO/SiO_2	0.20	0.40	0.60	0.80
H_2O/Na_2O	15.00	18.50	22.00	26.00

Based on the literature review, the molar ratios were pre-determined, and the following calculations were carried out for Mix 2. To perform these calculations, the molar masses of the relevant oxides were required and are tabulated in Table 0-3.

Table 0-3: Molar Mass of oxides

Molar Mass (g/mol)	SiO_2	Al_2O_3	CaO	Na_2O	H_2O	NaOH
	60.0843	101.9612	56.0774	61.9789	18.0200	39.9971

Step 1: Calculation of Lime Content

For calculation purposes, the quantity of fly ash is fixed at 100 grams, although this value can be adjusted based on specific mix design requirements. The number of moles of CaO and SiO_2 present in fly ash and lime is calculated using the following formulas:

$$Number\ of\ CaO\ moles\ in\ fly\ ash = \frac{\%\ composition\ of\ CaO\ in\ FA\ x\ Weight\ of\ FA}{Molar\ Mass\ of\ CaO} \quad \text{Equation 5}$$

$$Number\ of\ CaO\ moles\ in\ Lime = \frac{\%\ composition\ of\ CaO\ in\ Lime\ x\ Weight\ of\ Lime}{Molar\ Mass\ of\ CaO} \quad \text{Equation 6}$$

$$Number\ of\ SiO_2\ moles\ in\ fly\ ash = \frac{\%\ composition\ of\ SiO_2\ in\ FA\ x\ Weight\ of\ FA}{Molar\ Mass\ of\ SiO_2} \quad \text{Equation 7}$$

$$Number\ of\ SiO_2\ moles\ in\ Lime = \frac{\%\ composition\ of\ SiO_2\ in\ Lime\ x\ Weight\ of\ Lime}{Molar\ Mass\ of\ SiO_2} \quad \text{Equation 8}$$

In the following formulas, the known parameters include the weight of fly ash (FA), the percentage composition of CaO and SiO_2 in both fly ash and lime. The unknown variable is the weight of lime required in the mix. Given that the CaO/SiO_2 molar ratio is fixed at 0.4, the final equation can be derived as follows,

$$\text{Equation 5} + \text{Equation 6} - 0.2\ (\text{Equation 7} + |\text{Equation 8}) = 0$$

Which can be written as,

$$\left[\frac{\%\ Cao\ in\ FA\ x\ W_{FA}}{Mm_{CaO}} + \frac{\%\ Cao\ in\ HL\ x\ W_{HL}}{Mm_{CaO}}\right] - 0.2\left[\frac{\%\ SiO_2\ in\ FA\ x\ W_{FA}}{Mm_{SiO_2}} + \frac{\%\ SiO_2\ \ HL\ x\ W_{HL}}{Mm_{SiO_2}}\right] = 0 \quad \text{Equation 9}$$

For Mix 2, the following input parameters are required for the mix design calculations,

Percentage of CaO in Fly ash (% of CaO in FA)	=	2.887	%
Percentage of CaO in Hydrated Lime (% of CaO in HL)	=	72.800	%
Percentage of SiO_2 in Fly ash (% of SiO_2 in FA)	=	50.063	%

Percentage of SiO_2 in Hydrated Lime (% of SiO_2 in HL)	=	1.456	%
Molar Mass of CaO (Mm_{CaO})	=	56.077	g/mol
Molar Mass of SiO_2 (Mm_{SiO2})	=	60.084	g/mol

The required weight of hydrated lime corresponding to 100 grams of fly ash is calculated using Equation 9,

Weight of Fly ash (W_{FA})	=	100.000	Grams
Weight of Hydrated Lime (W_{HL})	=	21.870	Grams

Step 2: Calculation of Oxides in Fly-ash and Lime

The weights of fly ash and hydrated lime are first determined, after which the total oxide content contributed by each material can be calculated using the following expression,

$$Weight\ of\ SiO_2\ moles\ in\ fly\ ash = \%\ composition\ of\ SiO_2\ in\ fly\ ash\ \times Weight\ of\ Fly\ ash$$

$$Weight\ of\ SiO_2\ moles\ in\ lime = \%\ composition\ of\ SiO_2\ in\ lime \times Weight\ of\ hydrated\ lime$$

Similarly, the weights of Na_2O and CaO contributed by both fly ash and hydrated lime are calculated. The resulting values are as follows:

Oxides for 100 grams of fly ash,			
Weight of SiO_2 oxide	=	50.063	Grams
Weight of Na_2O oxide	=	0.825	Grams
Weight of CaO oxide		2.887	Grams
Oxides for 21.870 grams of hydrated lime,			
Weight of SiO_2 oxide	=	0.318	Grams
Weight of Na_2O oxide	=	0.005	Grams
Weight of CaO oxide		15.922	Grams

Step 3: Calculation of total moles based on molar ratio

The total oxide content from SiO_2 is derived solely from fly ash and lime. Therefore, the total weight of SiO_2 is the sum of SiO_2 content from both sources, i.e., 50.063 g (from fly ash) + 0.318 g (from lime) = 50.381 grams. The total number of moles of SiO_2 can then be calculated based on the following equation:

$$Total\ SiO_2\ moles\ in\ fly\ ash\ and\ lime = \frac{Oxide\ weight\ SiO_2\ in\ fly\ ash\ and\ lime}{Molar\ Mass\ of\ SiO_2}$$

Once the total number of moles of SiO_2 is known, the remaining oxide quantities can be determined based on fixed molar ratios. The corresponding expressions are given as follows:

$$Total\ Na_2O\ moles\ required = \frac{Na_2O}{SiO_2} Molar\ ratio\ \times Total\ SiO_2\ moles\ in\ fly\ ash\ and\ lime$$

$$Total\ CaO\ moles\ required = \frac{CaO}{SiO_2} Molar\ ratio\ \times Total\ SiO_2\ moles\ in\ fly\ ash\ and\ lime$$

$$Total\ H_2O\ moles\ required = \frac{H_2O}{Na_2O} Molar\ ratio\ \times Total\ Na_2O\ moles\ required$$

Total SiO_2 moles required	=	0.839	Moles
Total Na_2O moles required	=	0.126	Moles
Total CaO moles required	=	0.335	Moles
Total H_2O moles required	=	2.327	Moles

Step 4: Calculation of the total weight of all oxides

The required number of moles of each oxide in the mix proportion has been calculated. Based on these values, the corresponding total weight of the oxides required for the complete mix are determined as follows,

$$Total\ SiO_2\ weight\ required = Total\ SiO_2\ moles\ required\ \times Molar\ Mass\ of\ SiO_2$$

$$Total\ Na_2O\ weight\ required = Total\ Na_2O\ \ moles\ required\ \times Molar\ Mass\ of\ Na_2O$$

$$Total\ CaO\ weight\ required = Total\ CAO\ \ moles\ required\ \times Molar\ Mass\ of\ CaO$$

$$Total\ H_2O\ weight\ required = Total\ H_2O\ \ moles\ required\ \times Molar\ Mass\ of\ H_2O$$

Based on the expressions, the calculated values are

Total weight of SiO_2 required	=	50.381	Grams
Total weight of Na_2O required	=	7.796	Grams
Total weight of CaO required	=	18.81	Grams
Total weight of H_2O required	=	41.930	Grams

Although the individual oxide quantities have been calculated, the actual ingredient used is sodium hydroxide in pellet form. Therefore, the total required quantity of sodium hydroxide pellets must be determined based on the calculated Na_2O content.

Step 5: Calculation of Sodium Hydroxide (NaOH) solids

The equation of NaOH is,

$$2NaOH \rightarrow Na_2O + H_2O$$

The Na_2O content contributed by fly ash and lime has been calculated, and the total required Na_2O weight is known. Therefore, the difference between the total required Na_2O and the amount already provided by the raw materials gives the remaining Na_2O that must be supplied through sodium hydroxide pellets. Similarly, the number of moles shall be calculated by dividing the weight of Na_2O by its molar mass.

Weight of Na_2O in NaOH Solids (7.796-0.825-0.005)	=	6.965	Grams
Number of Na_2O moles in NaOH Solids (6.965/61.9789)	=	0.112	Moles

Since the number of moles of Na_2O and H_2O in the sodium hydroxide conversion equation are equal, the number of moles of H_2O is also 0.112. Therefore, the weight of H_2O present in the NaOH solids can be calculated by multiplying the number of moles by the molar mass of H_2O.

Weight of H_2O in NaOH Solids (0.112 x 18.02)	=	2.025	Grams
Hence, the total weight of NaOH solids (6.965 + 0.112)	=	8.990	Grams

Step 6: Calculation of NaOH Solution

To determine the quantity of water required to prepare the NaOH solution using 8.99 grams of solids, the number of moles of NaOH must first be calculated. This is done by dividing the mass of NaOH by its molar mass (39.9971 g/mol)

Number of NaOH moles in NaOH Solids (8.99/39.9971)	=	0.2248	Moles

In this research, a 10 M (molar) sodium hydroxide (NaOH) solution is used. Given that the molar mass of NaOH is 39.9971 g/mol, a 10 M solution corresponds to 399.971 grams of NaOH dissolved in 1 litre of water (approximately 1000 grams of water). The molarity expression shall be written as,

$$Molarity = \frac{Moles}{Volume\ in\ litres}$$

The Volume of water shall be calculated as,

Volume of water (0.2248/10)	=	0.022476 (22.476)	Litres (grams)

Hence, 8.99 grams of pure NaOH solution is mixed with 22.48 grams of water to prepare the NaOH solution. Hence, the total weight of NaOH solution is,

Total weight of NaOH solution (22.476 + 8.990)	=	31.466	Grams

Step 7: Calculation of free water

The amount of free water required for the mix is calculated as the difference between the total water required and the amount of water already used to prepare the NaOH solution.

Amount of free water (41.930 – 22.476)	=	19.454	Grams

Step 8: Final Mix Design

Materials	Quantity (grams)	Weight Percentage (%)
Fly ash	100.000	61.05
Hydrated Lime	21.870	13.35
NaOH Solution	31.466	13.72
Water	19.454	11.88

Step 8: Calculation of Liquids to Solids Ratio

In this mix proportion, the solid components include fly ash, hydrated lime, and sodium hydroxide (NaOH) pellets, while the liquid components consist of the water present in the NaOH solution and the additional free water. Therefore, the liquid-to-solid (L/S) ratio can be calculated as follows,

Liquids to Solids ratio	=	0.32	-

References

Barbosa, V. F. F., Mackenzie, K. J. D., & Thaumaturgo, C. (2000). *Synthesis and characterisation of materials based on inorganic polymers of alumina and silica: Sodium polysialate polymers* (No. 1441865273700; International Journal of Inorganic Materials, Vol. 2).

Bocullo, V., Vitola, L., Vaiciukyniene, D., Kantautas, A., & Bajare, D. (2021). The influence of the SiO2/Na2O ratio on the low calcium alkali activated binder based on fly ash. *Materials Chemistry and Physics*, *258*. https://doi.org/10.1016/j.matchemphys.2020.123846

Cheah, C. B., Samsudin, M. H., Ramli, M., Part, W. K., & Tan, L. E. (2017). The use of high calcium wood ash in the preparation of Ground Granulated Blast Furnace Slag and Pulverized Fly Ash geopolymers: A complete microstructural and mechanical characterization. *Journal of Cleaner Production*, *156*, 114–123. https://doi.org/10.1016/j.jclepro.2017.04.026

De Silva, P., Hanjitsuwan, S., & Chindaprasirt, P. (2013). *The Role of SiO 2 and Al 2 O 3 on the Properties of Geopolymers with and without Calcium* (pp. 25–35). https://doi.org/10.1002/9781118807743.ch3

Garcia-Lodeiro, I., Palomo, A., & Fernández-Jiménez, A. (2015). Crucial insights on the mix design of alkali-activated cement-based binders. In *Handbook of Alkali-Activated Cements, Mortars and Concretes* (pp. 49–73). https://doi.org/10.1533/9781782422884.1.49

Hoyos-Montilla, A. A., Tobón, J. I., & Puertas, F. (2023). Role of calcium hydroxide in the alkaline activation of coal fly ash. *Cement and Concrete Composites*, *137*. https://doi.org/10.1016/j.cemconcomp.2022.104925

Li, N., Shi, C., Zhang, Z., Wang, H., & Liu, Y. (2019). A review on mixture design methods for geopolymer concrete. *Composites Part B: Engineering*, *178*. https://doi.org/10.1016/j.compositesb.2019.107490

Low, I.-M., Alomayri, T., & Assaedi, H. (2021). *Cotton and Flax Fibre-Reinforced Geopolymer Composites: Synthesis, Properties and Applications* (1st Edition 2021). Springer Singapore Pte. Limited. https://doi.org/10.1007/978-981-16-2281-6

Ohno, M., & Li, V. C. (2018). An integrated design method of Engineered Geopolymer Composite. *Cement and Concrete Composites*, *88*, 73–85. https://doi.org/10.1016/j.cemconcomp.2018.02.001

Singh, B., Ishwarya, G., Gupta, M., & Bhattacharyya, S. K. (2015). Geopolymer concrete: A review of some recent developments. *Construction and Building Materials*, *85*, 78–90. https://doi.org/10.1016/j.conbuildmat.2015.03.036

T.Mabah, D. E., K.Tchakouté, H., Fotio, D., Rüscher, C. H., Kamseu, E., Bignozzi, M. C., & Leonelli, C. (2019). Influence of the molar ratios CaO/SiO2 contained in the sustainable microcomposites on the

mechanical and microstructural properties of (Ca, Na)-poly(sialate-siloxo) networks. *Materials Chemistry and Physics*, *238*. https://doi.org/10.1016/j.matchemphys.2019.121928